H.E.S.S. Observations of Two Recently Identified Gamma-Ray-Loud Binaries

Master Thesis

Tobias Vičánek Martínez

Institute for Astronomy and Astrophysics
Eberhard Karls Universität Tübingen

January 2023

Eigenständigkeitserklärung

Ich erkläre mit meiner Unterschrift, dass ich diese Arbeit selbstständig verfasst habe und keine anderen als die angegebenen Quellen benutzt habe. Alle Stellen dieser Arbeit, die dem Wortlaut, dem Sinn oder der Argumentation nach anderen Werken entnommen sind (einschließlich des *World Wide Web* und anderer elektronischer Text- und Datensammlungen), habe ich unter Angabe der Quellen vollständig kenntlich gemacht.

Ort, Datum

Unterschrift

Abstract

Gamma-ray binaries or gamma-ray-loud binaries (GRLBs) are binary systems that are composed of a massive star and a compact object and whose energy spectrum peaks beyond 1 MeV. The two gamma-ray sources HESS J1832-093 and 4FGL J1405.1-6119 have recently been identified as members of this class, following the identification of orbital periods derived from multi-wavelength studies. The aim of this work is to analyze TeV data of both sources, in order to search for signs of orbital variability through the search for light curve periodicity. In addition, a dedicated method that we call "phase map subtraction" is developed, for eliminating contamination in the 4FGL J1405.1-6119 TeV signal whose origin is unrelated to the source, with the purpose of estimating a detection significance of the source in the very high energy (VHE) domain.

Data gathered with the High Energy Stereoscopic System (H.E.S.S.) is analyzed to obtain orbital light curves based on the identified periods, and variability is tested with a χ^2-test against the hypothesis of constant flux. Light curves are also generated over the whole time period of data taking and tested for variability with the epoch folding method, as well as a generalized Lomb-Scargle period search. For the phase map subtraction, two orbital phase ranges of expected high and low TeV flux, respectively, are defined based on the typical multi-wavelength behavior of GRLBs. A source signal is extracted from the difference in the recorded signals between the two defined phase ranges.

For both analyzed sources, no statistically significant signs of orbital variability or periodicity can be inferred from the currently available data sets. A firm VHE-detection of 4FGL J1405.1-6119 cannot be claimed with the data at hand, however the developed phase map subtraction method proves to be a promising approach for a potential VHE-detection in the future.

Contents

1 Introduction **4**

2 Theory **6**
- 2.1 Gamma-Ray Binaries . . . 6
  - 2.1.1 4FGL J1405.1-6119 . . . 10
  - 2.1.2 HESS J1832-093 . . . 14
- 2.2 The High Energy Stereoscopic System . . . 19
  - 2.2.1 Cherenkov Astronomy with Imaging Atmospheric Cherenkov Telescopes . . . 19
  - 2.2.2 The H.E.S.S. Telescopes . . . 25

3 Methods **29**
- 3.1 Data Acquisition and Selection . . . 30
- 3.2 Event Reconstruction and Background Rejection . . . 33
  - 3.2.1 Hillas Parameters and *(3D) Model* Analysis . . . 34
  - 3.2.2 Gamma-Hadron Separation . . . 35
  - 3.2.3 Cut Configurations . . . 36
  - 3.2.4 Gamma Photon Reconstruction . . . 38
  - 3.2.5 Background Subtraction . . . 42
- 3.3 Phase Folding and Binning . . . 47
- 3.4 Flux Calculation . . . 48
  - 3.4.1 Spectrum Determination . . . 48
  - 3.4.2 Aperture Photometry . . . 49
- 3.5 Variability Search . . . 50
  - 3.5.1 χ^2-Test . . . 50
  - 3.5.2 Light Curve Periodicity . . . 51
- 3.6 Phase Map Subtraction for 4FGL J1405.1-6119 . . . 52

4 Analysis Procedure and Results **54**
- 4.1 HESS J1832-093 . . . 54
  - 4.1.1 Data Selection . . . 54
  - 4.1.2 Analysis Procedure . . . 54
  - 4.1.3 Orbital Variability and Periodicity . . . 56
- 4.2 4FGL J1405.1-6119 . . . 61
  - 4.2.1 Data Selection . . . 61
  - 4.2.2 Analysis Procedure . . . 61
  - 4.2.3 Orbital Variability and Periodicity . . . 63
  - 4.2.4 Phase Map Subtraction . . . 63

5 Discussion **70**
5.1 HESS J1832-093 70
5.2 4FGL J1405.1-6119 70

6 Acknowledgements **73**

Introduction

The night sky, along with all its riddles and mysteries, has been subject of interest to humankind for a mighty long time. It was over 2000 years ago when the ancient Greeks started laying the foundation for its scientific investigations as they are carried out in the modern day. One of the famous astronomers of that epoch, Hipparchus, created the first catalog of stars as early as ~150 B.C.E. [1].
What he probably did not know at that time, is that many of those stars are actually not alone - for instance, it is estimated that about one third of all nearby Sun-like stars are escorted by a companion [2], as part of a so-called stellar binary system. In general, a binary system is composed of two astronomical bodies, bound by gravitation and thereby kept in orbit around a common center of mass. Those bodies might be stars of any type, size and mass, or even stellar remnants like white dwarfs, neutron stars or black holes.
Thanks to the progress made in the development of modern observation techniques, which have been applied since the mid-2000s, one particular class of binary systems has surfaced in recent years, called *gamma-ray binaries*. Those systems consist of a compact object, which can be a neutron star or a stellar-mass black hole, that is accompanied by a massive star. They are characterized by their peculiar energy spectrum, which peaks beyond 1 MeV. One valuable key feature of binary systems is that they facilitate the observation of processes happening at variable physical conditions, which change in a periodic manner as the objects travel along their often highly eccentric orbits. Especially at high energies, those systems can be thought of as astrophysical laboratories, hosting conditions that are impossible to reproduce on earth. In consequence, the observation and study of gamma-ray binaries might offer new insights into particle acceleration physics, magnetized relativistic outflows or accretion–ejection physics [3]. They also hold out the prospect of a unique way of investigating pulsar magnetospheres. In order to avoid confusion between the abbreviations for gamma-ray *binaries* and gamma-ray *bursts* (GRB's), the former are also referred to as gamma-ray-loud binaries (GRLBs).
Fortunately enough, the tools for astronomical observations have greatly evolved since the days of Hipparchus, making a wide range of energies nowadays accessible for inspection. This was not least thanks to the technological developments of the 20$^{\text{th}}$ century, some of which gave birth to the field of very-high energy (VHE) gamma-ray astronomy [4], and ultimately facilitated the detection and investigation of GRLBs. Rather than by measuring incoming VHE gamma-rays at first hand, observations in this regime are made by taking advantage of certain secondary effects. One way of doing this is by using what is known as imaging atmospheric Cherenkov telescopes (IACT's).
When a high-energy photon enters the Earth's atmosphere, its interaction with the

atmosphere triggers the ignition of electromagnetic showers. Ultra-relativistic particles generated within these showers exceed the speed of light in air, which in turn leads to an emission of light known as Cherenkov radiation. This emission, which can be regarded as an electromagnetic analogy to the supersonic boom caused by an aircraft exceeding the speed of sound, is then eventually recorded by the IACT's. With the subsequent application of sophisticated analysis techniques to those measurements, it is possible to reconstruct the direction and energy of the photon that initiated the electromagnetic shower in the first place [4].
One of the leading observatories applying this technology is the High Energy Stereoscopic System (H.E.S.S.), located in the Khomas Highland in Namibia. This system comprises five IACT's that simultaneously observe gamma-ray sources in a range from 10s of GeV to 10s of TeV. Its name pays tribute to Victor Hess, who first discovered the cosmic radiation and was rewarded for his findings with the Nobel prize in 1963 [5].
The aim of this thesis is to analyze H.E.S.S. observational data of two GRLBs, namely HESS J1832-093 and 4FGL J1405.1-6119. Their orbital variability is investigated, and the observations are put into context with the multi-wavelength picture. In chapter 2, a review of the current general knowledge of GRLBs is given, followed by a more detailed discussion of the two studied sources. Afterwards, the physics and working principles behind H.E.S.S. are set forth. Chapter 3 gives a detailed description of the applied methods for data analysis. The analysis procedure and results are offered in chapter 4, the latter are discussed in chapter 5.

Theory

2.1 Gamma-Ray Binaries

Gamma-ray binaries, also referred to as gamma-ray-loud binaries (GRLBs), constitute a subclass of high-mass binary systems which is defined by three criteria. First, they host a compact object that is often expected, although in most cases not confirmed, to be a neutron star (NS), the other alternative being a stellar-mass black hole. Second, the other member of the binary system is a young, massive star of O or Be spectral class. Third, their energy spectrum peaks beyond a certain energy threshold. While the exact value varies slightly across literature, most frequently the line is drawn at 1 MeV. At the time of writing, there are 10 systems known to match those properties [6][7]. The presence of a NS is firmly established in three of those, indications are found in a fourth one. Hence, GRLBs represent a fairly novel class that is yet to be explored in more detail. A recent population synthesis study estimates an upper limit of about 230 such systems existing in our galaxy [8].
The known GRLB systems share a set of typical observational features that are detected in most cases. They show non-thermal emission in a broad energy range that spans from radio, over X-rays, to the high energy (HE, $\gtrsim 100\,\mathrm{MeV}$), and even to the very high energy (VHE, $\gtrsim 100\,\mathrm{GeV}$) regimes. In fact, most of their radiative output is found in the MeV-TeV range. As a common feature, the emission in all energy bands is typically modulated with the orbital period [3]. However, the intensity maxima across different energies do not necessarily happen at the same orbital phases. A link is only found between X-rays and VHE gamma-rays, where the orbital light curves (OLC's) are usually positively correlated.
Some other features, whilst not in all cases, are frequently encountered. Part of the systems show differences between the HE and the VHE radiation, both in spectral and timing characteristics. In those cases, the energy spectra of the two domains cannot be connected by a consistent model, but clearly indicate two separate components. Also, the OLC's in the two regimes often peak at different phases, in one case they are even anti-correlated. In addition, for several of the known systems, the unpulsed radio emission is known to be extended [9] [3].
Radio pulsations have been measured from three sources, namely PSR B1259-63, PSR J2032+4127 and LS +61° 363, thereby confirming that the hosted compact object is in fact a pulsar. In the case of LS 5039, pulsed X-ray emission has been detected, which again is considered a hint towards the presence of a NS [10]. For the rest of the known GRLBs, it remains unconfirmed whether the compact object is also a pulsar, or rather an accreting NS or a stellar-mass black hole [6].
A summary of the currently known GRLB systems, together with some of their

Source	Detections	Orb. Mod.	Relation X-rays & VHE	Relation HE & VHE
PSR B1259-63	Radio Optical X-rays GeV TeV	✓ ✓ ✓ ✓ ✓	Similar double-peak lightcurves.	Lightcurves behaving differently.
LS I +61° 303	Radio Optical/IR X-rays GeV TeV	✓ ✓ ✓ ✓ ✓	Correlation indicated.	No correlation, spectral cut-off at GeV energies.
LS 5039	Radio X-rays GeV TeV	✓ ✓ ✓ ✓	Peak at same orbital phase.	Anti-correlated light curves.
1FGL J108.6-5856	Radio Optical X-rays GeV TeV	✓ ✓ ✓ ✓ ✓	Peak at same orbital phase.	Peak *at same* orbital phase, spectral cut-off at GeV energies.
HESS J0632+057	Radio X-rays GeV* TeV **indicated*	✓ ✓ ✓* ✓	Similar structure.	Spectral cut-off at GeV energies.
HESS J1832-093	IR X-rays GeV TeV	✗ ✓ ✓ -	-	Different spectral components.
LMC P3	Radio Optical X-rays GeV TeV	✓ ✓ ✓ ✓ ✓	-	Peak at different orbital phases.
4FGL J1405.1-6119	Radio X-rays GeV	✓ ✓ ✓	-	-
PSR J2032+4127	Radio Optical X-rays GeV TeV *$P_{\text{Orb}} \sim 45\,\text{a}$	✓[11] ✓[12] ✓ ✗ ✓	Both variable around periastron*.	No variability in HE around periastron*.
HESS J1828-099 [7]	Radio X-rays TeV	- - -	-	Different spectral components.

Table 2.1: Summary of some basic observational features of the currently known GRLBs. All wave lengths in which the respective source is detected are listed under "Detections", whereas "Orb. Mod." indicates whether orbital modulation is seen (✓) or not (✗). Entries with a hyphen indicate that there is no available light curve data in at least one of the respective energy bands. The sources written in bold letters are the objects studied in this thesis. Unless indicated otherwise, the content of this table is based on [6].

observational features, is found in tab. 2.1. The astrophysical processes that lead to the observed emission from those systems, with its characteristics in time and energy, are understood only to a certain extent. In fact, there is no applicable standard model that can explain all the features observed from the different systems [3]. There are however some basic notions able to represent a foundation for further explanatory approaches. With the purpose of conceptualizing the physics behind GRLBs, two different main ideas have been proposed.

In the late 1990s, X-ray binaries had been recognized as sources of non-thermal radio emission and relativistic jets [3]. This led to the interpretation of elongated radio emission from GRLBs as the latter. In this scenario, the emission is powered by the accretion of matter onto the compact object, which in that case would be a stellar-mass black hole. Considering the analogy between such systems and active galactic nuclei (AGNs), this type of system was named "microquasars" [13]. Two examples of some well-studied microquasars are Cyg X-1 and Cyg X-3 [6]. It was speculated that particles accelerated in the jet could be the source of non-thermal gamma-ray emission, as it is observed from AGNs [3]. This could explain the emission observed from GRLBs.

However, this scenario cannot hold for the systems in which a radio pulsar has been detected. This is because radio pulsars generally do not accrete, since the pressure of the pulsar wind is strong enough to hold off in-falling matter [3]. Instead, the gamma radiation of those systems is understood to originate from interactions between the pulsar wind and the stellar wind of the massive companion. A fraction of the energy released through the spindown of rotation-powered pulsars drives a highly relativistic wind of $e^{\pm}$ pairs. Those particles initially co-rotate with the pulsar, tied to its magnetic field lines. However, this is only possible until the distance from the pulsar exceeds the light cylinder radius R_{L}, defined by

$$R_{\mathrm{L}} = \frac{c \cdot P_{\mathrm{Rot}}}{2\pi}, \tag{2.1}$$

where c is the speed of light and P is the rotational period of the pulsar. Beyond this point, further co-rotation would require superluminal speed, hence magnetic field lines and the tied particles decouple from the rotational motion and form the mentioned relativistic pulsar wind. This wind then propagates freely, until it collides with the radiatively driven wind from the massive companion star [14]. Particles accelerated at the resulting shock front are believed to be the emitters of the measured gamma radiation.

In the case of PSR B1259-63, this interpretation has been proposed on numerous occasions (see [6] and references therein) and is widely accepted. For systems where neither the presence of a black hole, nor the detection of radio pulsations can be firmly established, the reasoning becomes less straightforward. Nevertheless, there is a notable amount of indirect evidence that points towards this "pulsar scenario" as the favorable explanation.

For instance, the obvious similarities in spectral and timing characteristics, as explained above, do not only motivate to categorize those systems into the same, distinguished class - they also invite to think that those similar features are caused by the same type of mechanism. Further, the changing morphology of the radio emission resolved for some systems is more compatible with a comet-tail like behavior exhibited through the interaction between pulsar and stellar winds, rather than with a relativistic jet. The latter explanation would require jet precession on

orbital time scales, which is unprecedented [3]. In addition, constraints on the mass of the compact object obtained from radial velocity measurements, which have been carried out for some of the systems, allow for the presence of a stellar-mass black hole only at very high inclinations [6].
Those and other additional arguments (see [3] for more examples) suggest that the pulsar scenario is better suited to model GRLB systems. In comparison with PSR B1259-63 and PSR J2032+4127, where radio pulsations have been detected, the orbital periods of the other known GRLBs are much shorter [9][15][16]. Following Kepler's third law, the orbital separations are therefore much smaller in those other systems. This means that the tentative pulsar is embedded in denser regions of the stellar wind, where the optical depth with respect to free-free absorption is large enough to inhibit the propagation of any pulsed radio emission from the NS [17], which in consequence becomes impossible to detect. This picture, also referred to as the "hidden" pulsar scenario, is supported by the fact that for PSR B1259-63, the radio pulsations disappear around the periastron passage of the pulsar [3].
The specific details of the particle acceleration processes that happen at the shock front between the colliding winds, and of how the radiation in the different energy bands is generated, are not fully understood, and the modeling is a current topic of research. It is usually assumed that the X-ray signal is produced by synchrotron emission, while the gamma rays are generated through inverse Compton (IC) scattering of the particles of the relativistic pulsar wind, with the stellar radiation field acting as the source of seed photons [3]. Also, the often observed distinct spectral components in the HE and VHE domains are seen as evidence for two different particle populations, each emitting in one of the two different regimes [3]. Likewise, the typical correlation between the OLC's in X-rays and VHE gamma-rays can be interpreted as an origin from the same population of particles. Non-pulsed radio emission has been related to synchrotron emission for several of the systems [3][18][19][20].
Moreover, it is of interest to understand not only the origin of the radiation, but also the effects that lead to the orbital modulation that is typically observed in all energy bands. This has been related to two fundamental parameters that change during the orbital motion of the binary system. On one hand, the orbits can be highly eccentric, and the consequent change in distance between the two objects causes variations in the basic physical conditions at the surroundings of the pulsar. Once again, PSR B1259-63 provides a good example for this point, since the variability of the X-ray light curve, as well as the above mentioned disappearing of radio pulsations around periastron passage, are associated with the pulsar penetrating through the circumstellar disc of the massive companion [3]. On the other hand, the relative orientation of both objects with respect to the line of sight also differs along the orbit. This is relevant for emission, but also absorption mechanisms. For instance, the Compton cross-section depends on the angle between incoming and outgoing photons, so the anisotropic distribution of seed photons leads to an anisotropic emission of gamma-rays [3], which causes the observed flux to vary between different orientations with respect to the observer. It is a similar situation with the absorption of VHE gamma photons through pair production by interaction with the stellar UV photons, where the threshold energy for producing an $e^{\pm}$ pair depends again on the incident angle between the photons. Consequently, the absorption efficiency becomes phase-dependent as well. On top of that, other processes like relativistic

Doppler boosting or cascade emission might also play a role in shaping the orbital light curves [3].
Developing a model that accurately represents all details of the different systems is challenging, since at this point in time, it requires a trade-off between over-simplification of the emission region and assumptions based on estimates of limited accuracy [3]. Despite the difficulties, GRLBs bear the potential for new insights in different fields of astro- and particle physics. As reflected in the periodically changing behavior across various wavelengths, they offer multiple perspectives - literally - for the investigation of physical processes that take place under different physical conditions, changing in a recurrent way. This makes them unique astrophysical laboratories to study the physics of particle acceleration processes and magnetized relativistic outflows [3]. Moreover, they provide a special way of probing pulsar winds, whose constituents take part in interactions that happen much closer to the pulsar as compared to other related systems, like pulsar wind nebulae [3], making GRLBs adequate candidates to improve the current knowledge on pulsar physics.
As a resource for detailed investigation, multiwavelength analysis has been fundamental for exploring all known GRLBs. In this work, we aim to extend the upper edge of the analyzed energy ranges for two of the known GRLB sources, 4FGL J1405.1-6119 and HESS J1832-093, which have both only recently been identified as such. As can be seen from the entries indicated with bold letters in tab. 2.1, one of them has not yet been detected in TeV, while the other one has, yet does not feature any TeV light curve data either. However, before we proceed into the realms of the unexplored, it is first necessary to obtain an overview of the available data on those sources in other wavelengths, along with the resulting conclusions.

2.1.1 4FGL J1405.1-6119

Identified as a GRLB in 2019 [16], 4FGL J1405.1-6119 is one of the most recent members of this class of binary systems. It is listed in the fourth catalog of the *Fermi* Large Area Telescope (LAT) at a position of

$$\begin{aligned} &\mathrm{RA} = 14^{\mathrm{h}}05^{\mathrm{m}}11.6^{\mathrm{s}}, \\ \text{and}\quad &\mathrm{DEC} = -61^{\circ}19'56''\ (J2000)\ [21]. \end{aligned} \tag{2.2}$$

In a previous analysis, the counterpart from the third LAT catalog 3FGL J1405.1-6118 had been ranked as a probable pulsar candidate, and possible X-ray counterparts had been found in data from both the *Swift* X-ray Telescope (XRT), as well as the *Chandra* X-ray Observatory (CXO) [22]. Further, observations with IBIS on the *International Gamma-Ray Astrophysics Laboratory* (INTEGRAL) showed another X-ray signal associated with 3FGL J1405.1-6118, and spatial coincidence with the near-infrared (near-IR) source 2MASS J14051441-6118282/allWISE J140514.40-611827.7 was noticed [23].
The detailed analysis and subsequent classification as a GRLB of 4FGL J1405.1-6119 by [16] was fruit of a systematic search for signs of periodicity in LAT light curves, where the data for 3FGL J1405.1-6118 yielded a positive result. Thereupon, in a more thorough approach, GeV light curves of 4FGL J1405.1-6119 were generated by two slightly different methods, using probability-weighted, as well as conventional aperture photometry. While the former method improves the signal-to-noise ratio of the light curves, it can result in a distortion of photometric properties of the

source through different effects, which is why the latter method was applied as well. Afterwards, the power spectra of both light curves were analyzed.
For the probability-weighted light curve, the resulting power spectrum shown in fig. 2.1 (bottom panel) shows two significant peaks, at 6.8586 ± 0.0013 days and 13.7235 ± 0.0046 days. While the first one of the two is also featured in the power

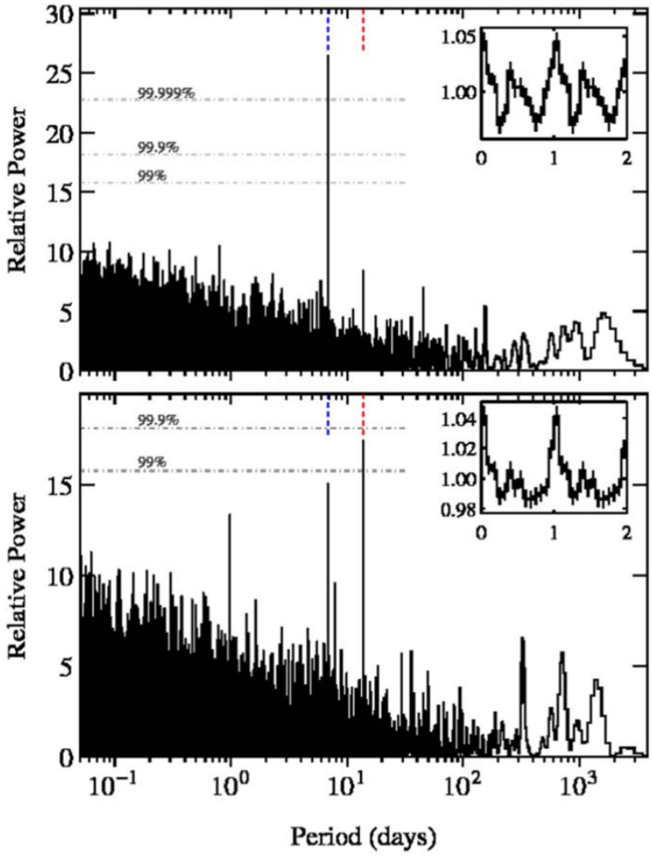

Figure 2.1: Power spectra of the LAT light curves of 4FGL J1405.1-6119. *Top:* Spectrum of the light curve obtained through conventional aperture photometry. *Bottom:* Spectrum of the light curve obtained through probability-weighted aperture photometry. The horizontal dashed-dotted lines indicate the False Alarm Probability levels, as introduced in [24], under the assumption of white noise. The vertical dashed lines indicate the positions of the two peaks at $6.856\,75 \pm 0.000\,96$ days (blue) and 13.7135 ± 0.0019 days (red). The insets show the respective light curves folded with a period of 13.7135 days, plotted over two periods for visualization purposes and normalized to 1. Adopted from [16].

spectrum of the light curve obtained by conventional aperture photometry (fig. 2.1, bottom panel), at a slightly different period of $6.856\,75 \pm 0.000\,96$ days, only a small-sized peak is observed close to 13.7 days. Nonetheless, since signals at multiples of the intrinsic modulation period of a light curve are not expected from Fourier-based analysis techniques, the longer of the two periods was interpreted as the modulation period, and the shorter period as its first harmonic. Therefore, derived from the single peak in the power spectrum of the un-weighted light curve, a value of 13.7135 ± 0.0019 days was adopted as the intrinsic modulation period of the system.

The finding was solidified by slicing the light curve into three equal-length sections, as the power spectra of individual parts showed consistent results. The differences between the power spectra obtained through the two different photometry methods were attributed to biases in the probability weighting, an effect resulting from the energy dependence of the instrument's point-spread function.
The insets in both panels of fig. 2.1 show the respective light curves folded on the adopted modulation period. A clear orbital variability can be observed in both cases, as the light curves exhibit a double-peak structure with maxima around phases 0.5 and 1.
The identified period of 13.7 days was then used to also create orbital light curves in X-rays. For this, both archival data, as well as data from dedicated observations with the XRT was employed. The result is shown in fig. 2.2. While a clear orbital

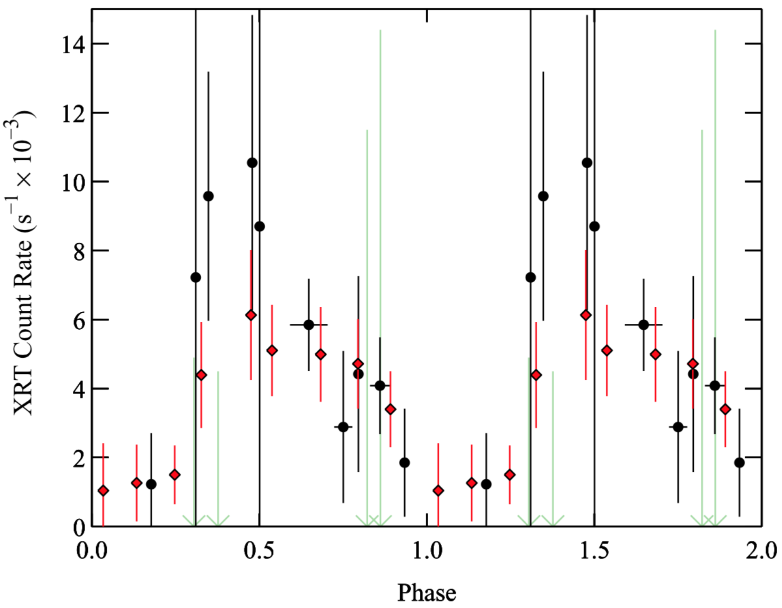

Figure 2.2: X-ray light curve of the counterpart of 4FGL J1405.1-6119 with data from the *Swift*-XRT, folded with a period of 13.7135 days. Data from dedicated observations is shown in red, archival data is shown in black. The green arrows indicate upper limits of 3σ confidence level, obtained from the archival data. Plotted over two periods for visualization purposes. Adopted from [16].

variability with approximately sinusoidal shape is manifested, the X-ray minimum occurs at orbital phases close to the primary GeV maximum seen in the LAT light curves. A cross-correlation analysis between the X-ray light curve and the non-weighted LAT light curve yielded a phase-shift of 0.568, which was also confirmed through consistent results from a sine-wave fit on the X-ray light curve. However, the certainty of this result is limited by the short coverage and large error bars of the X-ray observations.
Further, with the *Australia Telescope Compact Array* (ATCA), a radio point source was detected within the LAT error region, coincident with the positions of both the X-ray and near-IR counterparts. Again, the radio flux densities were folded on the 13.7 day period, the result of which is shown in fig. 2.3. As in the other, previously analyzed wave lengths, orbital variability is also observable in radio. While the

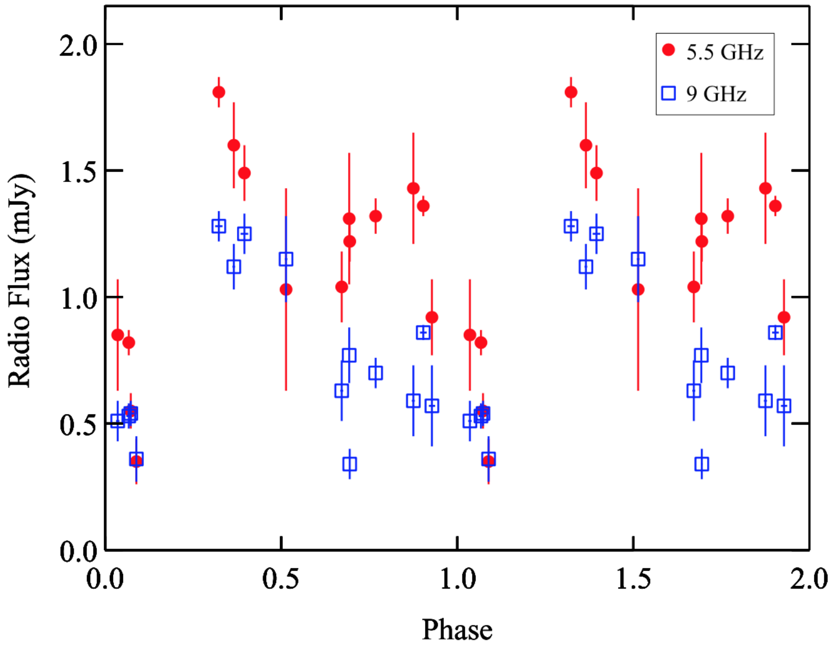

Figure 2.3: Radio light curve of the counterpart of 4FGL J1405.1-6119 with data from the ATCA, folded with a period of 13.7135 days. Plotted over two periods for visualization purposes. Adopted from [16].

phase coverage is not sufficient to precisely determine the radio flux maximum, the minimum seems to coincide with the primary GeV maximum, once again indicating an offset between the two orbital light curves.

Finally, data from FLAMINGOS-2 was used to obtain a near-IR spectrum. From this analysis, the counterpart was classified as an O6.5 III star, however emphasizing that the result should be re-evaluated in the future with a spectrum of higher signal-to-noise ratio.

The identification of the periodic modulation of 13.7 days, found in the LAT light curves and confirmed by the orbital variability seen in X-rays and Radio, together with the identification of the O-type stellar counterpart, ultimately lead to the classification of 4FGL J1405.1-6119 as a GRLB. The orbital light curves in X-rays and GeV peak at different orbital phases, as it is frequently observed in those systems. Due to various potential artifacts in the LAT light curves and/or power spectra, it would be beneficial to confirm the modulation period through independent analysis at other wave lengths [16]. Moreover, it is generally desirable to further investigate the behaviour of the system in other energy domains, especially towards the upper end where GRLBs exhibit most of their radiative output, in order to add more knowledge to a class that counts few members and is not completely understood at this point in time. This constitutes enough of an incentive to observe the source in VHE, with the aim of claiming a detection with H.E.S.S. which at the time of writing this thesis is pending, and analyzing the behavior of the orbital light curve. The process required for detection is not straightforward. Sky maps of the region in TeV, which result from a preliminary analysis of H.E.S.S. data, show the presence of a second TeV source close to 4FGL J1405.1-6119 in the field of view, as is shown in 2.4. Also, a diffuse LAT source is located nearby, partly overlapping with the 4FGL J1405.1-6119 position. Consequently, any signal measured from the source position is exposed to contamination through gamma-rays from the adjacent sources. Through a dedicated approach, which is also pursued in this work, this constant component can be removed from the signal by taking advantage of the expected source variability.

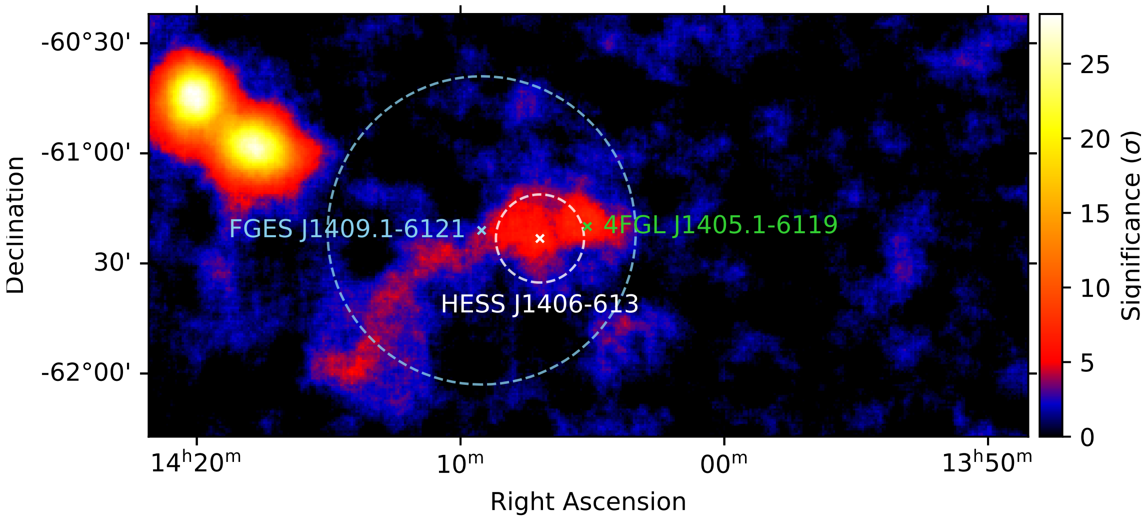

Figure 2.4: Significance map of the region around 4FGL J1405.1-6119 obtained from a preliminary H.E.S.S. analysis. The significance is a statistical measure for the probability of the presence of a TeV signal, see sec. 3.2.5. Crosses mark the source positions, dashed lines indicate the source extensions. 4FGL J1405.1-6119 is shown in green, the nearby TeV source [25] in white, the nearby LAT source [26] in light blue.

2.1.2 HESS J1832-093

Even more recently, in 2020, it was HESS J1832-093 that was granted membership in the club of GRLBs. The object had been detected five years earlier by the H.E.S.S. Collaboration [27] as a TeV point source, with a post-trial detection significance of 5.6σ, where a best-fitting position of

$$\begin{aligned} \mathrm{RA} &= 18^{\mathrm{h}}32^{\mathrm{m}}50^{\mathrm{s}} \pm 3^{\mathrm{s}}_{\mathrm{stat}} \pm 2^{\mathrm{s}}_{\mathrm{syst}}, \\ \text{and} \quad \mathrm{DEC} &= -9°22'36'' \pm 32''_{\mathrm{stat}} \pm 20''_{\mathrm{syst}}\ (J2000) \end{aligned} \tag{2.3}$$

was found. A subsequent search for counterparts in different wave lengths was performed in the same work. As shown in the H.E.S.S. excess map in fig. 2.5, the source lies close to the radio rim of the supernova remnant (SNR) G22.7-0.2, however no evident increase in radio flux was found around the source position. Likewise, a search for a GeV counterpart with LAT data did not yield any significant result. A search in X-rays however turned out more rewarding, as dedicated observations of the region with the *XMM-Newton* satellite revealed the new source XMMU J183245-0921539 as a potential counterpart to the TeV source. In addition, the infrared (IR) source MASS J18324516-0921545 was found to be spatially coincident with the X-ray source.
Several scenarios were proposed to explain the origin of the detected TeV signal.

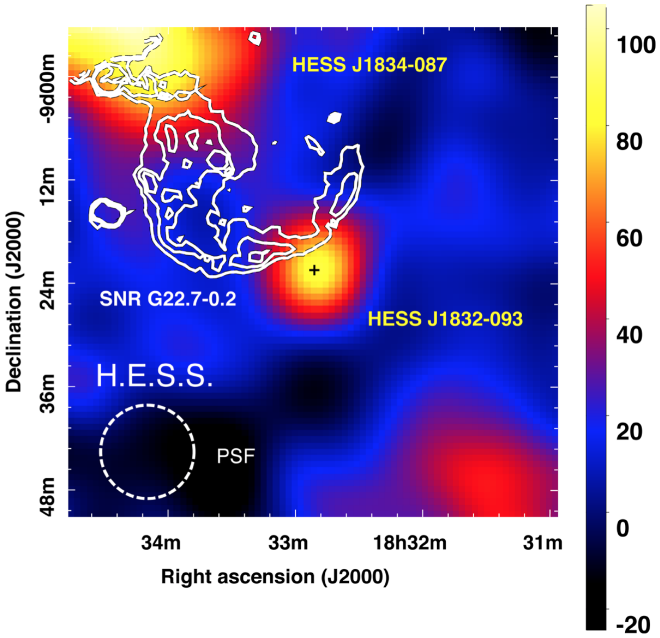

Figure 2.5: Excess map of the region around HESS J1832-093 obtained with H.E.S.S., smoothed with a 2D-Gaussian of 0.081° width. The black cross indicates the best-fitting position of the source with statistical errors, the white contours represent observations of the SNR G22.7-0.2 at 1.4 GHz [28]. Reproduced from [27].

For instance, it was suggested that protons might interact in dense molecular clouds (MC's) that had been detected nearby in the field of view (FoV), producing neutral pions that would then decay and emit gamma rays. Another scenario was that of a pulsar wind nebula (PWN), radiating through IC emission powered by an undetected pulsar. Finally, in view of the spatial coincidence with the IR source, the possibility of a binary system was also considered.
It was not until 2020 that the latter of the three scenarios was eventually confirmed in [15]. This time, the search for a GeV signal was successful, as the LAT source 4FGL J1832.9-0913 was found to be a potential HE-counterpart. Periodicity searches were then carried out both in X-rays and in GeV.
X-ray data obtained from archival observations with the *Swift*-XRT was analysed for that purpose. Together with additional X-ray data from the *Nuclear Spectroscopic Telescope Array* (NuSTAR) and from the CXO reported in [29], a light curve was obtained, from which a Lomb-Scargle [30][24] periodogram was subsequently generated. As can be seen in fig. 2.6, a significant peak is found at 86.28 ± 3.77 days. A compatible result was obtained by applying the epoch folding method proposed by Leahy [32], however providing no improvement with respect to the first result. The orbital light curve phase-folded with the 86 day period, which is shown in fig. 2.7, clearly indicates orbital variability, hence the finding was interpreted as the modulation period of the system. The two other non-negligible peaks at $\sim$99 days and at $\sim$65 days were explained as an artifact of the window function, and as a result of the deviation from a sinusoidal shape of the light curve, respectively.

As for the LAT data, searches for periodicity based on Fourier series showed no sign of orbital modulation. Nonetheless, a result was obtained with the epoch fold-

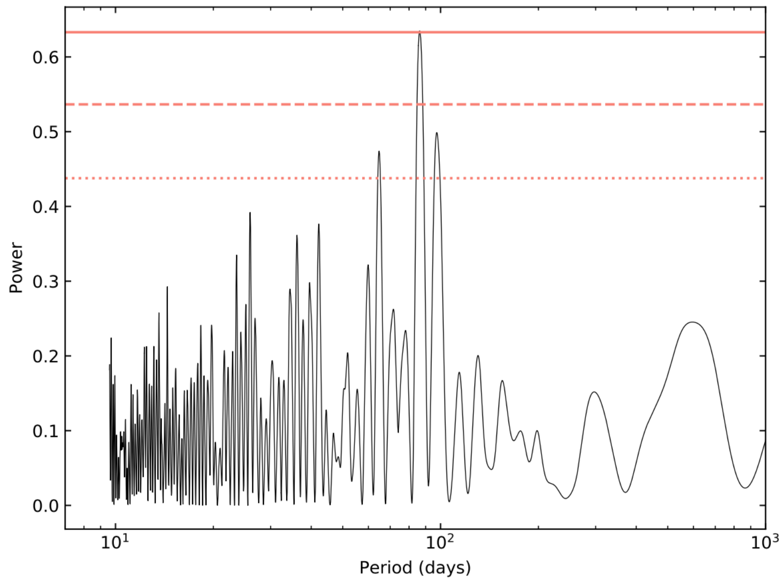

Figure 2.6: Lomb-Scargle periodogram obtained from the unbinned X-ray light curve of multiple data sets. The dotted, dashed and solid red lines represent False Alarm Probability levels of 3σ, 4σ and 5σ, respectively, calculated using the analytical approximation introduced in [31]. Reproduced from [15].

ing method. As shown in fig. 2.8, a signal is found at a period of 87.106 days. However, the S statistic [32] that assesses the statistical significance of the peak did not converge. Also, the result was not robust against variations in the number of phase bins, whereby neighboring peaks happened to reach levels similar to the primary one. Therefore, this result was interpreted as an indication of variability, rather than a confirmation of the true period.
Still, it allowed to compare between the orbital light curves in X-rays and GeV, folded on the 87.106 day period, which are shown in fig. 2.9. Once again, the maxima in those two different energy bands do not occur at the same orbital phase, a recurrent characteristic of GRLB systems. In addition, spectral analysis of the LAT data showed that the spectral energy distribution (SED) between GeV and TeV cannot be described by a single power law, but rather shows two separate components. Those findings did not only strengthen the association between the sources at different wave lengths, but also led to the classification of HESS J1832-093 as a new GRLB. Extrapolating the habitual behavior of other members of this category, we expect the orbital light curve in TeV to be correlated to the one in X-rays. In order to investigate this relation, once again with the purpose of refining the comprehension of GRLBs in general and of this source in particular, this work aims at generating an orbital light curve of HESS J1832-093 in TeV and analyzing its behavior, using H.E.S.S. observational data.

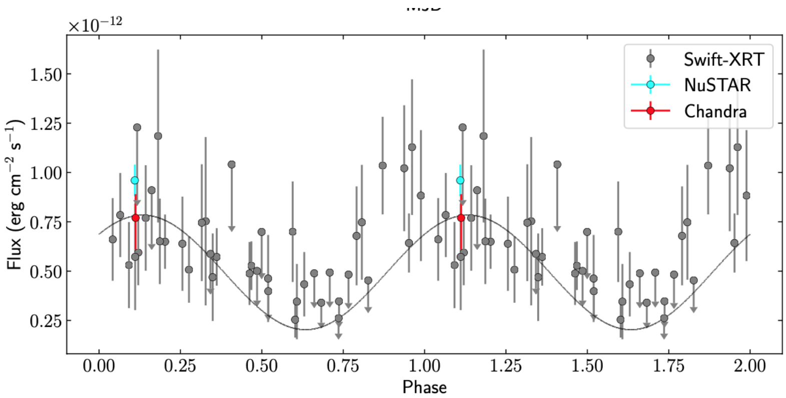

Figure 2.7: Phase folded X-ray light curve including data from multiple observations of XMMU J183245-0921539, folded with a period of 86.28 days as found in the Lomb-Scargle periodogram. Plotted over two periods for visualization purposes. Reproduced from [15].

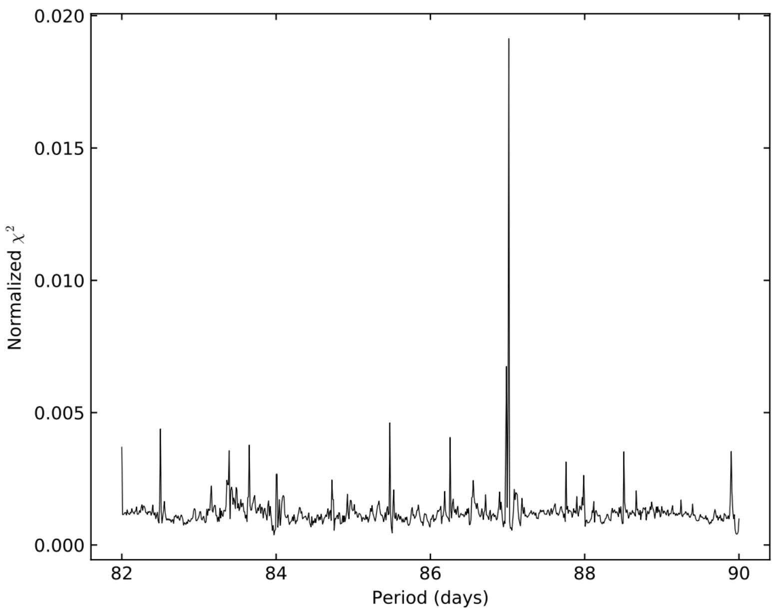

Figure 2.8: χ^2-values of the different periods tested with the epoch folding method for the LAT data of 4FGL J1832.9-0913, using ten phase bins. A larger value of χ^2 indicates a larger variability of the orbital light curve folded with the respective period. Reproduced from [15].

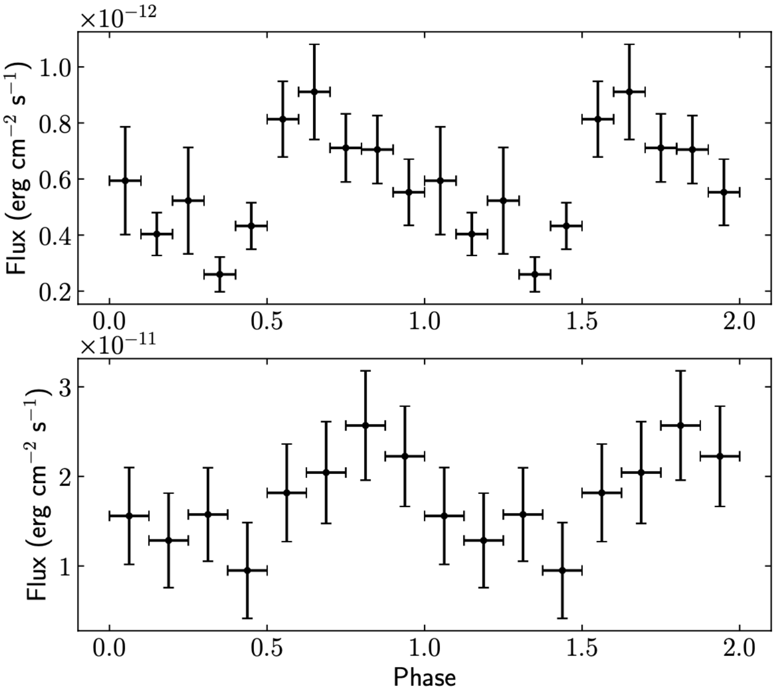

Figure 2.9: Orbital light curves of the counterparts of HESS J1832-093 folded with the period of 87.106 days obtained from the epoch folding method on the LAT data. Plotted over two periods for visualization purposes. *Top:* X-ray data from the XRT observations of XMMU J183245-0921539. *Bottom:* GeV-Data from LAt observations of 4FGL J1832.9-0913. Reproduced from [15].

2.2 The High Energy Stereoscopic System

Figure 2.10: Image of the H.E.S.S. array in Namibia. Picture by Christian Föhr, MPIK [33].

The High Energy Stereoscopic System (H.E.S.S.) is an array of five imaging atmospheric Cherenkov telescopes (IACTs), located in the Khomas highland in Namibia. Its name pays tribute to Victor Hess, who first detected cosmic radiation in 1912 [34]. It was inaugurated in September 2004, with four telescopes operating during H.E.S.S. I, the first phase of the project. A fifth, much larger telescope was added later and went operational in July 2012, initiating the H.E.S.S. II era.
IACTs detect gamma-rays by means of an indirect measurement. Rather than interacting with the incident gamma photons at first hand, the detectors pick up on secondary effects caused by interactions of the VHE radiation with the atmosphere. To facilitate proper comprehension of the workings of our measurement device, the development and basic principles of this observation technique are explained, followed by a more detailed description of the H.E.S.S. telescopes.

2.2.1 Cherenkov Astronomy with Imaging Atmospheric Cherenkov Telescopes

The phenomenon of Cherenkov radiation was first observed by its namesake P.A. Cherenkov in 1934 [35], who detected light emission from beta particles propagating through water. The theoretical explanation for this effect was delivered three years later by I. Frank and I. Tamm [36]. The association with cosmic rays came in 1947, when P.M.S. Blackett [37] proposed that, since the same effect should also occur in gases, Cherenkov radiation might be emitted by cosmic ray particles traveling through the atmosphere. This was first measured in 1952 and linked to cosmic ray air showers. For this, W. Galbraith and J.V. Jelley [38] used a simple setup, consisting of a search-light mirror and a photomultipliter tube (PMT) placed in a garbage can to shield the detector from stray light signals. Ever since then, both detection and analysis methods have continuously been developed, even though the technique faced major challenges in its early beginnings. From the first measurement of atmospheric Cherenkov light, it took 37 years until both aspects of the technology were advanced enough to facilitate the first firm detection of gamma-ray emission: In 1989, the Whipple collaboration eventually succeeded to measure a signal above 0.7 TeV from the Crab nebula [39], which turned out to be the strongest steady-state gamma-ray emitter in the sky.

In general, gamma-ray astronomy faces two essential challenges in comparison to observations at lower energies. First, there is no known way to focus gamma-rays above a limit on the order of MeV. Because of their ways of interacting with matter, powered by the high amount of energy they carry, gamma-rays become increasingly difficult to reflect or redirect from their path. Second, fluxes rapidly decrease towards higher energies. This fact is illustrated in fig. 2.11, showing an energy spectrum of the cosmic ray flux over a wide energy range, which serves as a proxy for the typically observed galactic source emission. In order to be able to still detect signals

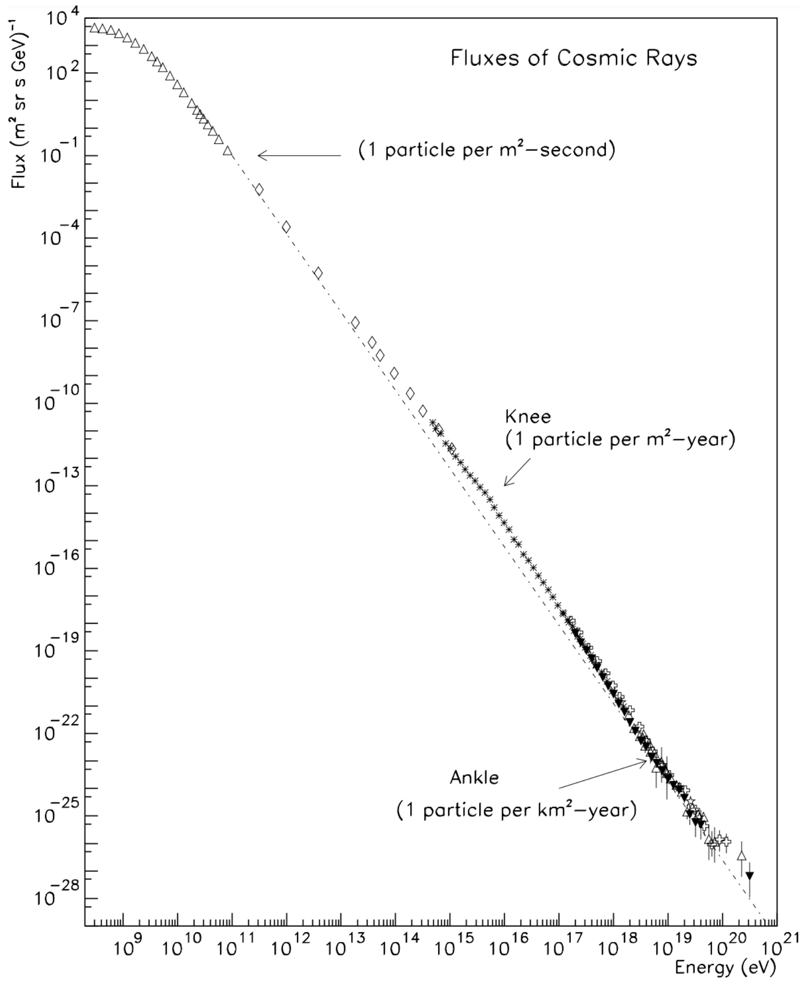

Figure 2.11: Spectrum of cosmic ray flux spanning multiple energy bands. Intensities decrease steeply towards high energies. Taken from [40].

at such low intensities, a high effective area of the instrument is required, defined as the product of geometrical area and detector efficiency. The two challenging factors provide an upper energetic boundary to the capability of space-based detectors: Through the impossibility of focusing, the geometrical area is essentially restricted to the detector area, which in turn is limited to $\sim 1\,\mathrm{m}^2$ by the high costs of space technology. Luckily, as we will see, Cherenkov astronomy provides a solution to both of these issues. It does so by making use of two fundamental effects, which make gamma-rays observable when they propagate through Earth's atmosphere.

The first one is the development of electromagnetic showers. When a high energy photon enters the atmosphere, by interacting with the Coulomb field of atmospheric nuclei it can create an $e^{\pm}$ pair. The energy threshold for pair production is twice the electron mass $2m_{\mathrm{e}}$, which corresponds to a photon energy of $E_{\gamma} = 1.022\,\mathrm{MeV}$ and is therefore easily surpassed by gamma-rays in the HE and VHE ranges. Again in the Coulomb field of atmospheric nuclei, those particles are then deviated from their trajectory and consequently emit Bremsstrahlung, which leads to the creation of more gamma photons, which again produce $e^{\pm}$ pairs, and so on. The process is illustrated on the left hand side in fig. 2.12. In this avalanche-like effect, more and more particles are created, amongst which the energy of the initial gamma photon is redistributed. The number of particles initially grows exponentially, reaching its maximum when the charged particles in the shower fall below the critical energy E_{C}, which in air has a value of 83 MeV. At this threshold, losses of $e^{\pm}$ through ionization and atomic extinction become dominant, leading to a rapid termination of the shower [4].

The second important effect is the aforementioned Cherenkov radiation. In a medium with refractive index $n > 1$, light travels at a velocity v_{Ph} given by $v_{\mathrm{Ph}} = c/n$, where c is the speed of light in vacuum, i.e. light is slowed down in the medium. Thereby, it becomes possible for ultra-relativistic particles to actually propagate through a medium faster than light. As illustrated in fig. 2.13, a charged particle generally has a polarizing effect on its encompassing medium. The medium's subsequent relaxation creates electromagnetic waves, which propagate through the medium at v_{Ph}.

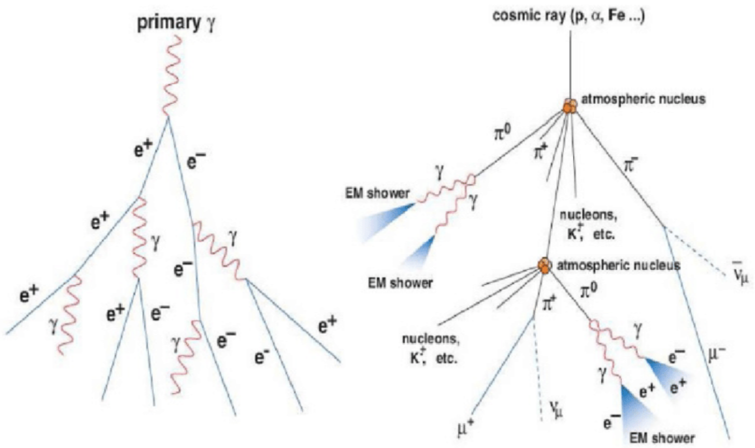

Figure 2.12: Schematic illustration of the development of atmospheric air showers. *Left:* Development of an electromagnetic air shower, caused by a primary gamma photon. *Right:* Development of a hadronic shower and its sub-components, caused by a primary nucleus. Taken from [41].

If the particle responsible for the initial polarization travels *slower* than v_{Ph}, according to Huygen's principle the waves interfere destructively and hence no radiation is emitted. However, if the particle travels through the medium at *superluminal speed*, those wave fronts add up coherently in one specific direction. As is schematically illustrated in fig. 2.14, the angle θ_{C} between the direction of motion of the particle and the wave vector $\vec{k}$ of the resulting emission is given by

$$\cos\theta_{\text{C}} = \frac{c}{n \cdot v_{\text{P}}}, \tag{2.4}$$

where v_{P} is the velocity of the particle. This leads to a cone-shaped electromagnetic "shockwave" with opening angle θ_{C} that is generated behind it. The effect can be thought of as an electromagnetic analogy to the sonic boom of an aircraft moving at supersonic speed. A detailed theoretical description is given in [42].
The $e^{\pm}$ pairs generated in the electromagnetic showers carry enough energy to emit

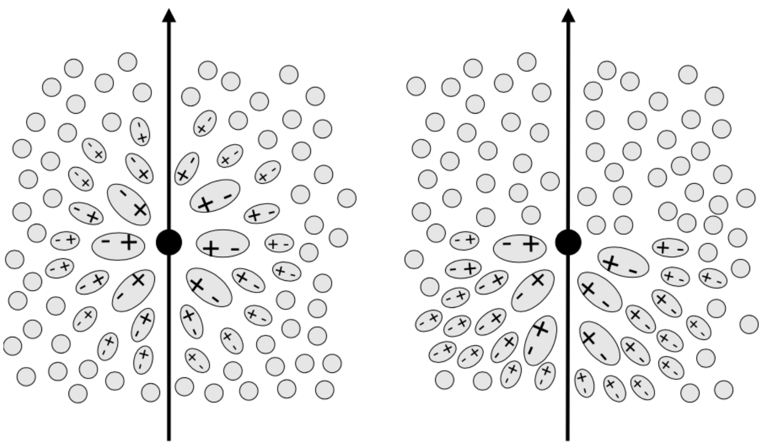

Figure 2.13: Illustration of the polarizing effect of a charged particle on its encompassing medium. *Left:* A particle moving at sub-luminal speed ($v < v_{\text{Ph}}$). *Right:* A particle moving at super-luminal speed ($v > v_{\text{Ph}}$). Adapted from [4].

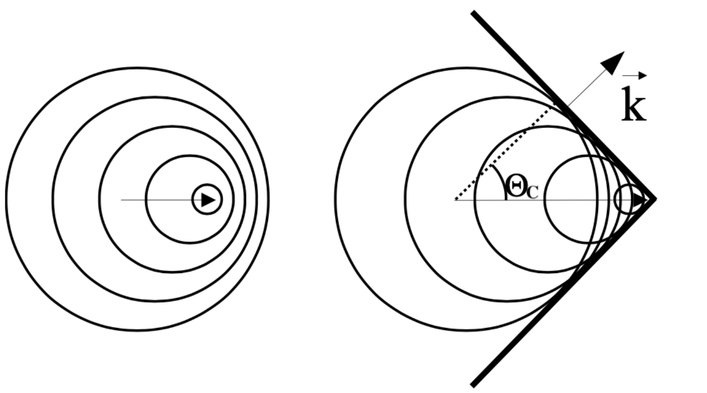

Figure 2.14: Illustration of the propagation of wave fronts emitted by a charged particle. *Left:* A particle moving at sub-luminal speed ($v < v_{\text{Ph}}$). *Right:* A particle moving at super-luminal speed ($v > v_{\text{Ph}}$). $\vec{k}$ is the wave vector of the resulting Cherenkov radiation, Θ_{C} is the opening angle of the Cherenkov light cone. Adapted from [4].

radiation through this process, and the emitted Cherenkov light is what IACTs eventually measure. Those light flashes are of the duration of a few nanoseconds[1], and their spectra, influenced by the emission profile and atmospheric absorption, peak in UV and extend into the optical range. As is shown in [4], despite the inhomogenities of the atmosphere, the amount of Cherenkov light emitted from the shower is about proportional to the energy of the primary gamma photon that ignited the shower in the first place. Fig. 2.15 offers an illustration of the whole process on a macroscopic scale. The maximum shower development happens at an altitude of $\sim 10\,\mathrm{km}$, with an opening angle of the Cherenkov light cone $\theta_\mathrm{C} \sim 1°$, which leads to Cherenkov light pool of $\sim 120\,\mathrm{m}$ radius illuminating the ground [4]. The technique provides a relatively large effective area, which corresponds to the size of the light pool and is on the order of $10^5\,\mathrm{m}^2$ [4]. From the measured Cherenkov light, it is possible to reconstruct the direction and energy of the incoming primary gamma particle. The currently used generation of IACTs makes use of stereoscopic measurements, simultaneously recording events with multiple telescopes. This facilitates an improved background rejection, as well as higher angular and energy resolution compared to single telescope measurements. However, IACTs offer only a small FoV of a few degrees, and the duty cycle is limited to $\sim 10\%$ [4], since the observations are restricted to clear and moonless nights. The main experimental challenges derive from the Cherenkov light flashes being short in duration ($\sim$ ns), as well as low in intensity, hence detectors need to be both fast and sensitive.

Other challenges that manifest at the level of data analysis are the accurate treatment of variations in atmospheric conditions and the rejection of background sig-

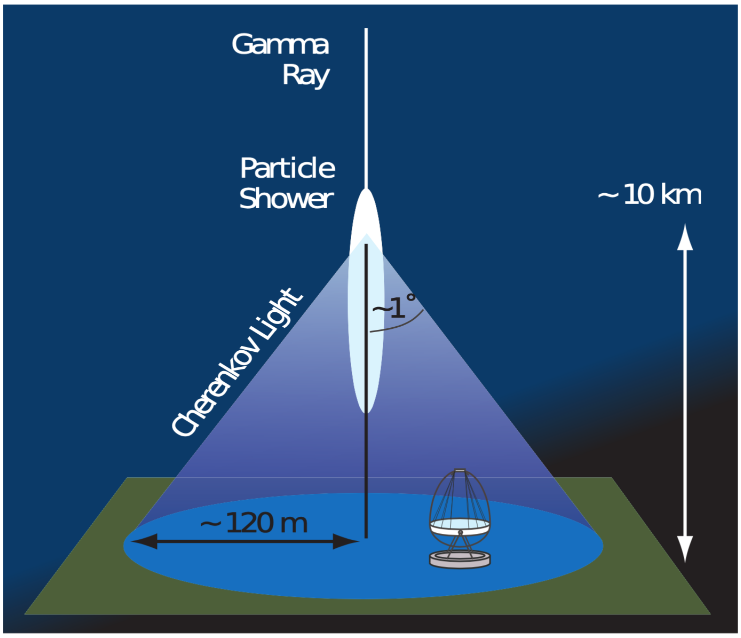

Figure 2.15: Macroscopic representation of an electromagnetic air shower emitting Cherenkov radiation, which is picked up by an IACT on the ground. Taken from [4].

[1]The short duration of the Cherenkov flashes of a few ns is the reason why they are not picked up by the human eye, which has a time resolution on the order of $\sim 100\,\mathrm{ms}$ as derived from the usual maximum of 60 fps used for videos.

nals. The former aspect is important for the correct energy reconstruction of gamma events, and therefore particularly affects spectral analysis. Clouds and aerosols act as absorbers for atmospheric light, weakening the Cherenkov radiation by reducing the number of photons that reach the detector. As a consequence, a reduced atmospheric transparency leads to an underestimation of gamma photon energies. The quality criteria applied for data selection have to account for short-term variations, like local clouds passing through the FoV during measurement, as well as long-term variations, like seasonal changes in aerosol concentrations. The applied methods are described in section 3.1.
Cherenkov astronomy is characterized by a strong background component. Besides gamma-photons, atmospheric showers are also triggered by cosmic electrons and positrons, as well as hadrons like protons or heavier nuclei. This leads to a distinction between electromagnetic and hadronic showers, which additionally comprise processes of the strong and weak interactions throughout their development. At the beginning of a hadronic shower, the primary cosmic ray particle decays mainly into pions and kaons. The neutral pions quickly decay into two gamma photons, generating an electromagnetic sub-shower. The charged pions and kaons however can interact with other atmospheric nuclei to further develop the hadronic component of the shower. However, another possibility is for them to decay into muons and anti-neutrinos, which constitute the third, muonic component of a hadronic shower. The process is illustrated on the right hand side of fig. 2.12. Due to the different interactions and components, the two types of atmospheric showers differ in their developmental properties. Hadronic showers are ignited at lower heights in the atmosphere, exhibit a stronger lateral broadening throughout their development, and die out more slowly. This is exemplarily depicted in 2.16. Those differences translate into distinguishable characteristics of the Cherenkov radiation that reaches the ground and is recorded with IACTs. Fig. 2.16 displays the results of simulations of different air showers, which show the trajectories of emitting particles during shower development, as well as the Cherenkov light that arrives on the ground. Through parametrization of the recorded shower images, metrics can be introduced for statistical discrimination between electromagnetic and hadronic showers, based on the individual image parameter values. A more detailed description of these methods is given in sec. 3.2.
The rejection of background signals happens at two different stages. First, as just described, various parameters of the single events recorded with the cameras are used to distinguish between gamma-like events, which are likely to originate from a gamma-ray, and background-like events, which have a higher probability of stemming from a charged cosmic ray. The latter are excluded from further analysis. Later in the analysis, the amount of remaining background signal at a position of interest can be estimated in different ways, and is then subtracted from the recorded signal. The details of these methods are discussed in 3.2.5.
Regarding the locations of IACT observatories, two aspects need to be considered. Detecting the Cherenkov light requires a site with little light pollution, since the Cherenkov flashes and consequently the detector sensitivity extend far into the optical spectrum. Also, the optimal altitude constitutes a trade-off between high transparency of the atmosphere to the Cherenkov light, which is achieved at higher altitudes, and a proper, ideally complete development of the electromagnetic showers, which requires lower altitudes. The sweet-spot is usually reached at $\sim 1500\,\mathrm{m}$

[4]. One location suitable for IACT observations is found in the southwest of Africa.

2.2.2 The H.E.S.S. Telescopes

H.E.S.S. is situated in the Khomas highland of Namibia, close to the Gamsberg mountain, at 23°16′18″ South, 16°30′0″ East, and at an altitude of 1800 m above sea level. The country has an especially low population density, which keeps light pollution at reduced levels. The location in the southern hemisphere provides good visibility of the galactic plane. The four smaller telescopes CT1-4 are arranged in a square with a side length of 120 m, which is optimized for sensitivity at an energy threshold of 100 GeV [44]. The fifth, larger telescope CT5 is located in the center of the square. It provides an improved, i.e. lowered energy threshold and allows for observations with less dead-time thanks to faster readout electronics [45]. However, since only data recorded with CT1-4 was analyzed for this work, the following descriptions are focused on the smaller telescopes.

The telescopes are constructed of steel and installed with an altitude/azimuth mounting. The dishes are arranged in Davies-Cotton style [46], with the outer borders forming a hexagon of 13 m separation between parallel sides, and with a spherical profile. They are equipped with 382 individual, round mirror facets of spherical profile with a 60 cm diameter each, resulting in a total effective mirror surface area of 107 m^2. The camera in the focal plane has a distance of 15 m to the dish. Each one of the mirrors has been remotely adjusted by electrical support units for perfect alignment onto the focal plane of the camera. The azimuth and elevation angle of the telescopes are controlled by friction drives, which provide slew rates up to 100 °/min in both axes. The physical pointing position is monitored by two shaft encoders, one at the central bearing for azimuth, and one at the end of the elevation axis for elevation angle. The digital precision is of 10″ [47].
Each camera consists of 960 photo-multiplier tubes (PMTs), corresponding to one pixel each, arranged in a hexagonal array. The PMTs are assembled into 60 drawers, each containing 16 PMTs, along with their respective electronics and high voltage (HV) supplies. Each tube is provided with a Winston cone to bundle up the light that would otherwise fall between the PMTs, and also to shield the detectors from stray light signals. The FoV of a single pixel is of 0.16° diameter, while the FoV of the total detector extends to a diameter of 5°. The width of the on-axis optical point-spread function (PSF), given as the rms width of the projected 1-dimensional intensity distributions σ_{proj}, has a value of 0.23 mrad [48]. The width varies across the field of view, and with different elevation angles, as is shown in fig. 2.18. However, this value stays well below the single pixel FoV radius of $\sim$ 1.4 mrad. Fig. 2.19 shows different views of the camera and its components.

The storage of observational data is managed through a three-level trigger system [49]. The first, single-pixel level is reached when at least one pixel reaches a threshold of four photo-electrons (p.e.) within a time frame of 1.5 ns. The second level, which addresses the whole camera of one telescope, requires a coincidence of at least three triggered pixels within one sector, defined as overlapping square-shaped groups of 64 pixels. The third level to finally prompt data storage is reached when at least two telescopes trigger within an interval of 80 ns. If all three trigger level requirements are satisfied, the images of cameras that triggered individually on the second level are read out and stored for later data processing - which leads us to the next chapter.

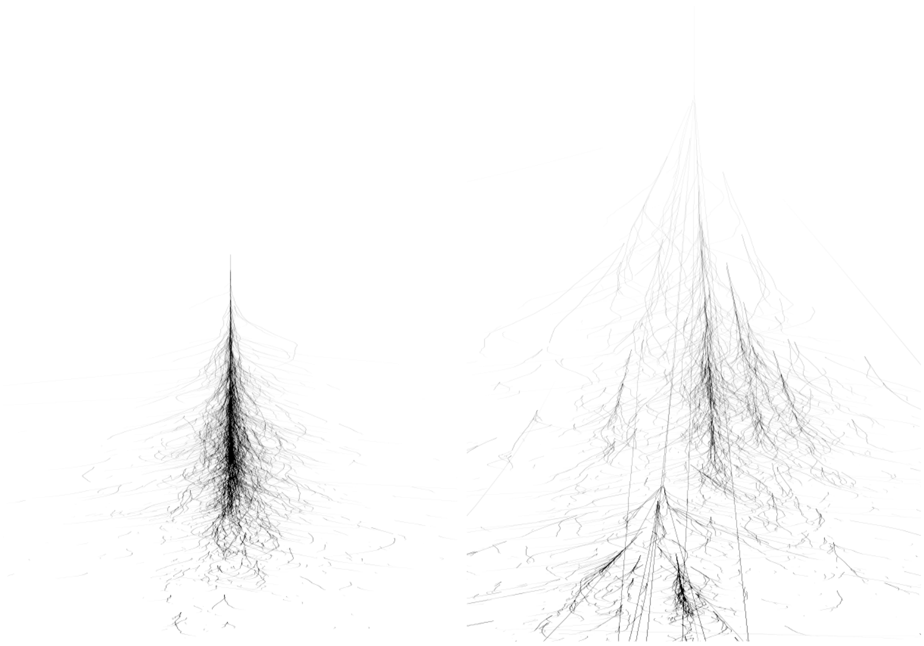

(a) Development of gamma-induced shower.

(b) Development of Proton-induced shower.

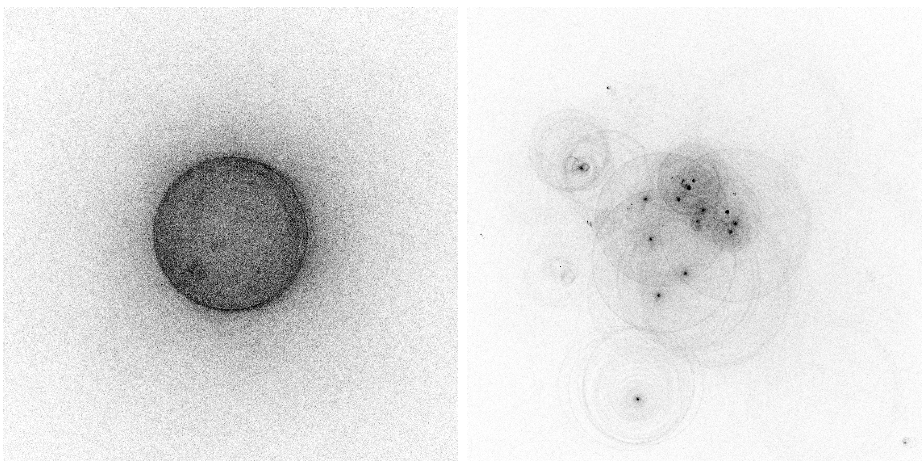

(c) Cherenkov light of gamma-induced shower.

(d) Cherenkov light of Proton-induced shower.

Figure 2.16: Simulations of an electromagnetic shower induced by a 300 GeV gamma-photon and a hadronic shower induced by a 1 TeV proton. A longitudinal view of the trajectories of emitting particles during shower development is shown in 2.16a and 2.16b, showing heights up to 27 km and with an image width of 600 m. A lateral view of the same showers is shown in 2.16c and 2.16d, where the images correspond to a square of 400 m side length. Taken from [43].

Figure 2.17: View of CT1, one of the smaller telescopes. Taken from [33].

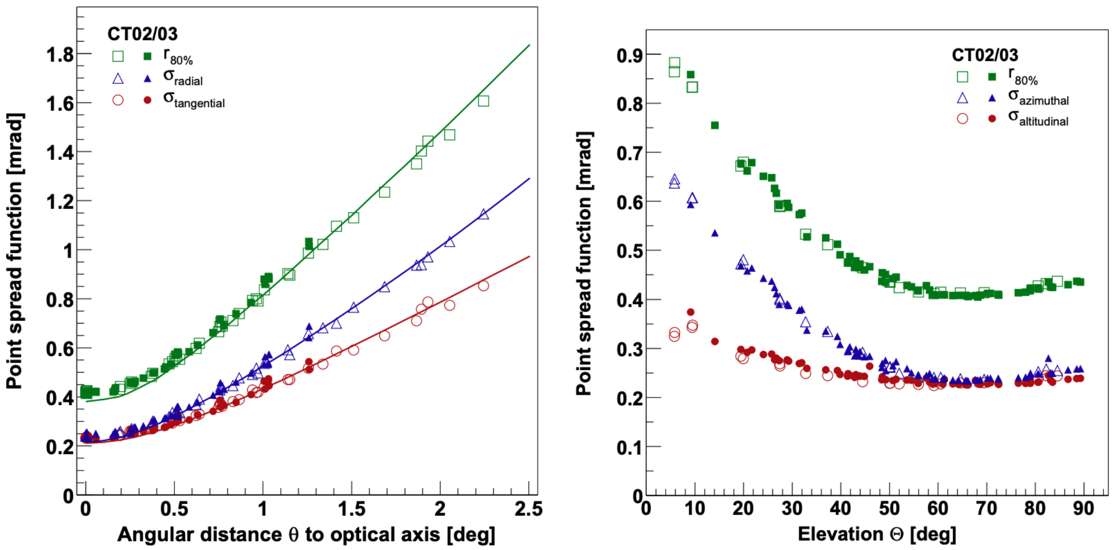

(a) PSF across the FoV at a fixed elevation of $\sim 65°$.

(b) PSF at different elevation angles.

Figure 2.18: Width of the PSF of the cameras of CT2 and CT3 at different angular distances θ to the optical axis, expressed as the rms width of the projected distributions in both radial (squares) and tangential (triangles) directions, as well as the radius $r_{80\%}$ encompassing 80% of the light. (squares). Taken from [16].

(a) Camera mounted in one of the telescopes, with an open lid.

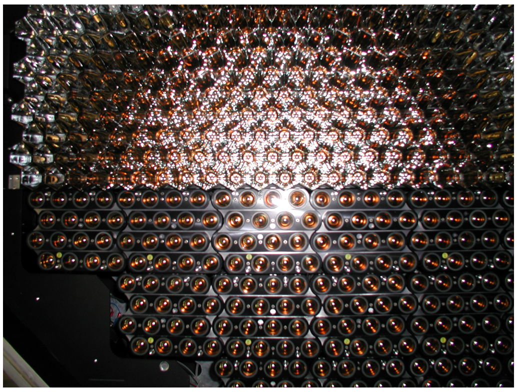

(b) Front view of the camera array in final stages of development. The upper half of the array is equipped with Winston cones in front of the PMTs. The lower half shows the sub-division into drawers of 16 PMTs each.

Figure 2.19: Different views on the camera of the smaller telescopes CT1-4. Taken from [33].

Methods

The procedure of data analysis employed for this thesis is essentially divided into five steps:

1. **Data selection:** Potentially useful sets of observational data, referred to as runs, are identified and included in the analysis based on specific quality criteria.

2. **Event Reconstruction and Background Rejection:** Recorded camera images are used to reconstruct the energy and direction of the incident gamma photon. Background events are rejected through various methods.

3. **Binning and Phase Folding:** Reconstructed gamma counts are assigned to their corresponding orbital phase based on timing information. Runs are merged into combined data sets, statistics are calculated for individual phase bins.

4. **Flux calculation:** The source spectrum is determined through a power-law fit to the measured energy spectrum. Flux values are calculated for each phase bin, as well as for each night of observation, based on the source spectrum, recorded counts and exposure in the specific bin or night.

5. **Variability search:** The calculated light curves are tested for variability and/or periodicity through various different methods.

In addition, for the case of 4FGL J1405.1-6119 we apply a dedicated method referred to as **Phase Map Subtraction**, where we use the expected correlation between the X-ray and TeV light curves to define "bright" and "dark" phases, and subsequently subtract the dark phase counts from the bright phase counts, in order to eliminate the signal contamination from neighboring sources.
At the time of writing, analysis methods that are able to produce a combined result which incorporates data from CT1-4 and data from CT5 recorded with the latest camera system are still under development. Therefore, this work contemplates only data from CT1-4, and the following descriptions apply to the corresponding analysis procedure. The processes of gamma-hadron separation and event reconstruction, as well as the process of spectrum determination, are applied by using the Heidelberg HESS Analysis Program (HAP-Hd), a software package for H.E.S.S. data analysis. The respective procedures are described according to the implementation within the software.

3.1 Data Acquisition and Selection

For H.E.S.S. observations, data is generally recorded and stored in units of 28 min duration, referred to as runs. The duration is chosen as a trade-off between enough time for sufficient statistics on one hand, and a duration short enough to avoid strong variations in observational conditions on the other. Nonetheless, the duration of single runs might also be shorter due to different limitations during observations, like poor observation conditions or hardware malfunctions. The total run duration includes times at which the telescopes are busy tracking the source position, therefore not taking any data. The time spent on actual data taking is referred to as live time.
The first step of data selection consists of searching the H.E.S.S. data base for suitable runs. For this, all runs are chosen for which the pointing position of the telescopes was within 2° separation to the position of the source of interest (SOI). Hence, both dedicated observations of the SOI as well as observations of nearby sources are included into this pre-selection. Observations with H.E.S.S. are usually taken in *Wobble* pointing mode, where the telescope pointing position is slightly shifted with respect to the position of the SOI, with alternating directions of the shift between different runs, see fig. 3.1. This is necessary for proper background subtraction methods described in sec. 3.2.5.

As the observations were made over a long period of time, the state of the instrument can vary between runs in different aspects of hardware conditions. Also, as described in sec. 2.2.1, unfavourable atmospheric conditions during observations might impair the quality of the data, leading to wrong results of reconstructed gamma energies and the loss of faint events. Therefore, it is necessary to evaluate the quality of all available data, in order to assess which of the runs are to be included in the analysis. For this purpose, two standard sets of quality criteria are examined for each individual run. Those sets have been established as a measure for run quality in H.E.S.S. analysis. Failed criteria might lead to the exclusion of single telescopes from the run, or to the exclusion of the entire run from the analysis. The following descriptions are based on [51].
The detection criteria are usually applied for the purpose of detecting sources, which requires information on measured counts. For this, it is desired to include runs that

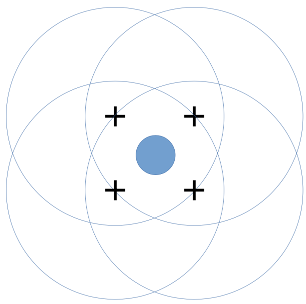

Figure 3.1: Illustration of the Wobble observation mode. The blue circular area represents the SOI region, black markers indicate the telescope pointing position for different runs, and blue circles the corresponding telescope FoV. Taken from [50].

improve the signal-to-noise ratio, which can be reduced through noise induced by hardware malfunctions. A correct flux reconstruction, which has an important dependence on the atmospheric conditions, is less relevant for this step. Therefore, with the exception of run duration, only instrumental aspects are considered. A minimum run duration of 10 min is required to guarantee significant count statistics. Afterwards, it is ensured that each telescope is participating in a minimum part of the events registered at the third level of triggering (see sec. 2.2.2). If one of the telescopes registers much less events as compared to the others, it is an indication of problems with the camera, and therefore that single telescope is excluded from the run. The threshold for participation fraction, that is the relative participation of single telescopes in central trigger events, is set to 0.4 for runs without CT5. Since the energy threshold is lower and the readout electronics are faster for CT5, the threshold is reduced to 0.04 if CT5 was participating in the observation.
Similarly, a certain amount of PMTs in single cameras might not be participating for different reasons. One possible reason is any kind of physical damage that causes the high voltage of the PMT to be missing. Those pixels are usually excluded for the entire, or even several entire observation periods, as the associated problems usually require a hardware expert on-site to be solved. Other reasons are temporary deactivation of single PMTs caused by over-current protection, which can be triggered by bright events like meteorites, airplanes, etc. If too many pixels are not participating in the measurement, a correct reconstruction of gamma photons becomes difficult. Hence, a limit is imposed on the number of missing pixels. The number of long-term, "HV-off" missing pixels is required to be smaller than 50, whereas the number of short-term "hardware" missing pixels must be smaller than 120.
Another criterion considered is the accuracy of telescope tracking, i.e. how precisely the telescopes were pointing at the desired position during the run. Faulty tracking might lead to an incorrect reconstruction of the source position, or to events not being associated with their actual position of physical origin. To avoid this, two different criteria are implemented. The actual position of the telescopes measured by the shaft encoders (see sec. 2.2.2) is compared to the intended nominal pointing position stored in the data base. To assure pointing accuracy, if the deviation between the two surpasses a mean value of $1'$ averaged over the whole run, the telescope is excluded. In addition, to also ensure smooth tracking during the run, the r.m.s. of the deviation must be below $10''$.
On top of those hardware cuts, additional aspects of atmospheric conditions are considered. The combination of hardware cuts and atmospheric cuts, referred to as spectral criteria, results in a more restrictive run selection at consistently comparable trigger thresholds that assures an accurate reconstruction of gamma energies and effective areas, which are both employed to ultimately determine energy fluxes. Two additional conditions are therefor included.
The first assessment is derived from the telescope trigger behaviour. Too strong variations in the trigger rates on time scales of run duration, or even shorter, are an indicator of significant changes in observational conditions, like clouds passing through or increasingly covering the FoV. Those effects are quantified by two parameters.
First, a straight line $L(t)$ is fitted to the trigger rate values as a function of time $R(t)$ during the run. The first quantity δ_1 is defined as

$$\delta_1 \coloneqq |L(t_{\max})/\langle R \rangle|, \tag{3.1}$$

where $t_{\max}$ is the last-filled time bin value and $\langle R\rangle$ is the mean system trigger rate. Therefore, δ_1 represents the absolute ratio between the mean trigger rate and the last value of the fitted trigger rate, providing a measure for the uniform change of the trigger rate throughout the run. A graphic illustration is offered in fig. 3.2. The

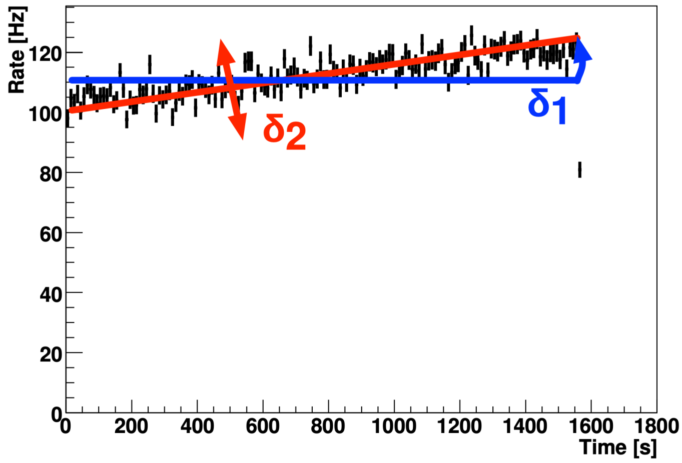

Figure 3.2: Representation of the two parameters δ_1 and δ_2 used for quantifying the trigger rate stability. The plot shows the recorded trigger rates throughout one run as black data points. The blue line represents the mean trigger rate $\langle R\rangle$, the red line represents the linear function $L(t)$ fitted to the data. Taken from [51].

maximum allowed value is set to $\delta_1 = 30\%$.
The second quantity δ_2 is the r.m.s. percentage value of the trigger rate values with respect to the linear fit, defined as

$$\delta_2 := \frac{100}{\langle R\rangle} \cdot \sqrt{\sum_{\mathrm{i}=1}^{N} \frac{\left(R(t_{\mathrm{i}}) - L\left(t_i\right)\right)^2}{N}}, \tag{3.2}$$

where N is the total number of time bins. Hence, δ_2 gives a measure for fluctuations of the trigger rate on time scales shorter than the run duration. Again, fig. 3.2 gives a graphic illustration. The cut value is set to $\delta_2 = 10\%$.
With δ_1 and δ_2 covering the changes on time scales of run duration and shorter, what is left to monitor are the long-term variations of observational conditions. Besides natural seasonal changes, a big contribution to this is made by agricultural biomass burning, typically carried out in the region during early summer months. Those increase the concentration of aerosols in the atmosphere, again decreasing the transmissivity for Cherenkov light. To take those long-term changes into account, a quantity called transparency coefficient T is defined. It is the average value[1] of four telescope-specific parameters t_{i}, which are proportional to the atmospheric transparency. The parameter is designed to be as independent as possible from any hardware effects. Since a properly conducted detailed elaboration would extend beyond the scope of this chapter, we refer to [52] for an exact definition of the transparency coefficient, with explanations of the quantities used therein. For a run to be included in the analysis, the value of T has to be between 0.8 and 1.2.

[1] A correction factor is applied to account for telescope multiplicity.

All the explained criteria are listed in 3.1, together with their respective cut values. Since the used reconstruction methods described in the next section are designed

Criterion	Requirement
Run duration	>10 min
Trigger participation fraction	>0.4 w.o. CT5, >0.04 w. CT5
Telescope Tracking	Mean dev. <1′, dev. r.m.s. <10″
Broken Pixels	"Hardware" < 120, "HV Off" < 50
Trigger rate stability	$\delta_1 < 30\%$, $\delta_2 < 10\%$
Transparency coefficient	$T \in [0.8, 1.2]$

Table 3.1: Summary of quality criteria applied for run selection. The upper block of the table constitutes the detection criteria, both blocks together form the spectral criteria.

for stereoscopic observations, only runs for which at least two telescopes pass the criteria are finally included in the selection.
Another possible reason for the exclusion of runs is the absence of data summary tables (DSTs) in the data base. DSTs are files containing intermediate results of some initial analysis steps. Those steps comprise the processing of raw pixel data, for which aspects of instrument calibration have to be considered. This part of the analysis is sophisticated and computing expensive, however independent of the individual analysis purpose. Therefore, it is more feasible to be executed once in a centralized fashion. The resulting DSTs are stored in the data base, where they can be accessed for further processing of observational data. In some cases however, due to any kind of technical malfunctions, data transfer errors etc., those files might not be available for single runs, which constitutes the last of the possible exclusion criteria. All data sets that pass the quality cuts are included in the run list, which is then ready to be analyzed.

3.2 Event Reconstruction and Background Rejection

The first essential step of the HAP analysis is the separation between gamma-like events induced by gamma-rays (and electrons, formally), and background-like events induced by hadronic cosmic rays. Afterwards, the camera images of the selected events are analyzed to reconstruct the energy and direction of the incoming gamma photon.
Throughout the history of Cherenkov astronomy with IACTs, those methods have continuously been developed, refined, renewed and replaced. Since newer meth-

ods such as the ones used in this work usually build on their predecessors, a brief description of the antecedent analysis procedures is given.

3.2.1 Hillas Parameters and *(3D) Model* Analysis

In 1985, A.M. Hillas [53] first proposed a method to separate between gamma-like and background-like events. The approach made use of the fact that the camera images of gamma-ray induced showers are in good approximation of elliptical shape, while images of hadronic showers are more spread and uneven. Hillas introduced a set of parameters based on the first and second moments of the image to describe its shape. Those correspond to the length and width of the ellipse, the total image amplitude, the distance of the image center of gravity (COG) from the optical axis, the orientation and the azimuthal[2] location of the ellipse. Fig. 3.3 shows a geometric representation of the Hillas parameters. By defining discrimination thresholds for the values of those parameters, which contain a great part of the image information, events can be separated into gamma-like and hadron-like. Also, by combining multiple images acquired through stereoscopic observations, the gamma-ray energy, arrival direction and impact distance, which is the distance between the telescope and the intersecting point of the primary particle track extended to the ground, can be reconstructed. The procedure is illustrated in 3.4.

Another reconstruction method of improved performance called *model* analysis is based on an image template fitting procedure. A semi-analytical model that describes the electromagnetic air shower development and the IACT response is used to generate expected shower images for given values of gamma energy, direction and impact distance. The recorded shower image is then compared to this library of templates, in order to determine the best-fitting shower parameters through a multi-dimensional fitting procedure. The *model* analysis was further developed for H.E.S.S. data by using a simpler analytical 3-dimensional Gaussian air shower model, and therefore re-named *3D model* analysis.

As is described in the next sections, the method for gamma-hadron separation im-

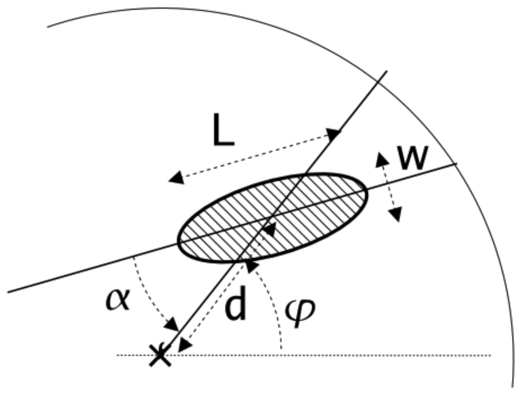

Figure 3.3: Geometric representation of the Hillas parameters: Length L and width W, distance d, orientation angle α and azimuthal angle φ. Taken from [54].

[2]Azimuthal with respect to an arbitrary axis inside the image plane.

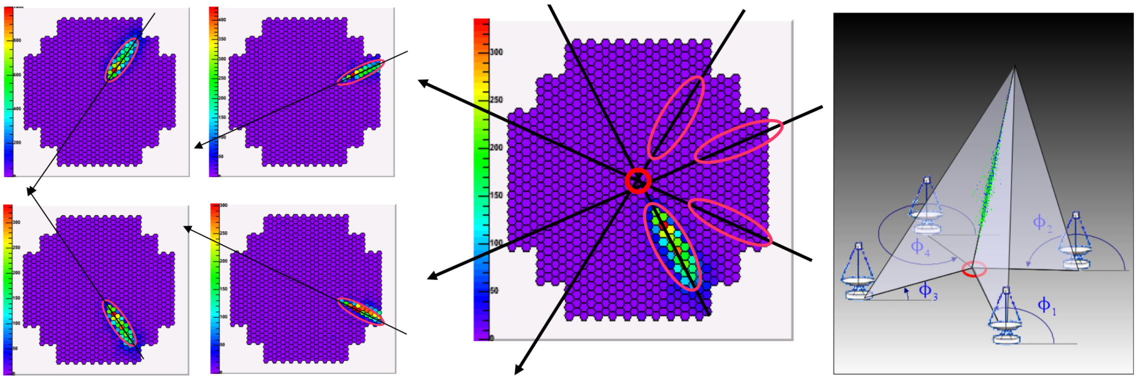

Figure 3.4: Illustration of the stereoscopic Hillas reconstruction. The plots on the left and center show the recorded camera images, where the color indicates the pixel amplitude. From a single telescope image, a plane containing the shower track and the telescope is reconstructed (left). Intersecting the planes for different telescopes (center and right) yields the shower direction and impact distance. Taken from [54].

plemented in the HAP-Hd software makes use of some of the Hillas parameters. Also, similar to the *(3D) model* analysis, the used gamma reconstruction method is based on multi-dimensional fitting of the camera images to a previously generated template library.

3.2.2 Gamma-Hadron Separation

Before the recorded camera images are classified as gamma-like or background-like, a simple image cleaning procedure is applied to eliminate night sky background (NSB) signals from the data. For this, two threshold values are defined. Pixels are required to have an intensity of 5 photo-electrons (p.e.) and a neighboring pixel with at least 10 p.e., or vice versa. All pixels that do not satisfy this condition are eliminated from the image. Fig. 3.5 shows a camera image before and after cleaning.

The identification of background-like events is done by use of a boosted decision tree (BDT) based method. The selection algorithm behind a BDT can be described by a two-dimensional structure like the one displayed in fig. 3.6. Each node represents a binary split decision based on one of the characterizing input parameters derived from the image (like some of the Hillas parameters), where a criterion is

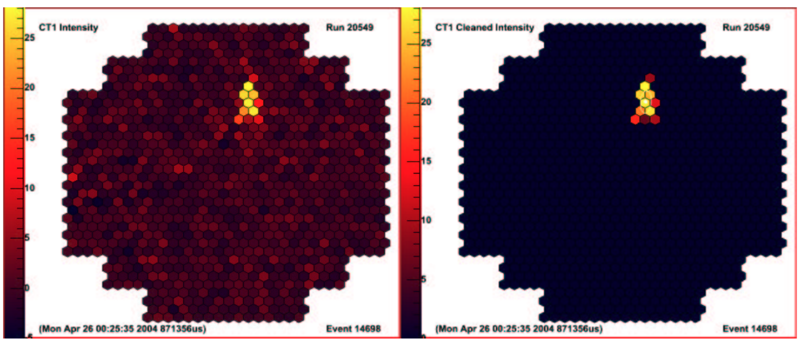

Figure 3.5: Recorded camera image before (left) and after (right) cleaning. Taken from [55].

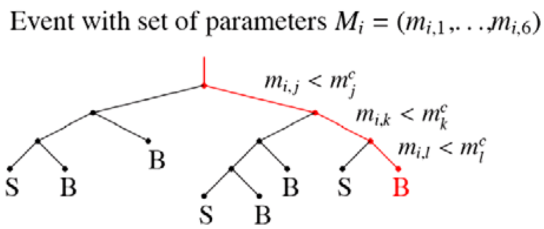

Figure 3.6: Graphical representation of a boosted decision tree. Taken from [56].

either met or not. By concatenating such decisions, at the end of the BDT an event is classified as either gamma- or background-like. The determination of the specific decision criteria is done by machine learning techniques, where the BDT is trained on a set of events of known type. This training set is composed of Monte Carlo (MC) simulations for gamma-like events, and recorded off-source signals as background-like events. To reduce the instability against statistical fluctuations of the training set, a BDT is extended to a *forest* of BDTs with varying split criteria. The output ζ is then determined as a weighted mean vote of the classification of all single trees, and describes the probability of an event being gamma- or background-like.
For every recorded image, the parameters evaluated by the BDTs are obtained by a preceding Hillas event reconstruction. They include the image width, length and total amplitude as part of the Hillas parameters, which are averaged over all participating telescopes. Further, a parameter called mean reduced scale width ($MRSW$) is considered. For an image with defined size and reconstructed impact distance, the measured width W_i is compared against the mean expected width $\langle W_\mathrm{i} \rangle$ obtained from gamma-ray simulations. On the level of a single telescope i, the scaled width SCW_i is defined as

$$SCW_\mathrm{i} := \frac{(W_\mathrm{i} - \langle W_\mathrm{i} \rangle)}{\sigma_\mathrm{i}}, \tag{3.3}$$

where σ_i is the spread of the expected width distribution. Then, the included parameter $MRSW$ is defined as the weighted average over all participating telescopes

$$MRSW := \frac{1}{\sum_\mathrm{i}^{N_\mathrm{Tel.}} \omega_\mathrm{i}} \cdot \sum_\mathrm{i}^{N_\mathrm{Tel.}} \left(\mathrm{SCW_i} \cdot \omega_\mathrm{i}\right), \tag{3.4}$$

where the weighting factors $\omega_\mathrm{i} := \langle W_\mathrm{i} \rangle^2 / \sigma_\mathrm{i}^2$ account for the accuracy of gamma-ray simulations and $N_\mathrm{Tel.}$ is the total number of telescopes participating in the event. In addition, the depth of the shower maximum X_Max is also reconstructed from the images and considered in the BDT, again as a weighted average over all telescope images. Finally, the average spread of reconstructed energies between the single telescopes $\Delta E/E$ is included. All those parameters participate in the BDT decision process, leading to the mentioned output parameter ζ, interpreted as the "gamma-likeliness" of the event.

3.2.3 Cut Configurations

Finally, based on the retrieved parameter values, each event is classified as either gamma- or background-like. The discriminating threshold parameter values are dictated by the used cut configuration.

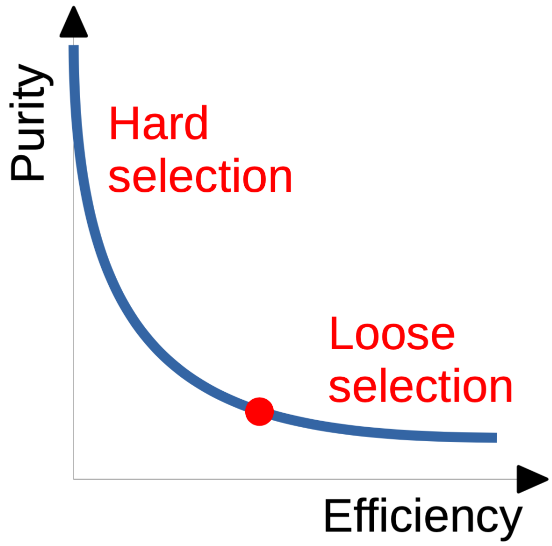

Figure 3.7: Relation between purity and efficiency for different cut configurations. Taken from [50].

Generally, the event classification is always imperfect, since the distributions of parameter values, such as the Hillas parameters, overlap for both event classes. Therefore, a number of background events is likely to pass the event selection, just as some gamma events might be rejected. It is however possible to set parameter thresholds in a way that minimizes one of the two effects at the cost of increasing the other, thereby facilitating a trade-off between efficiency and purity. Efficiency indicates the fraction of gamma events that pass the selection cuts, while purity is the relative fraction of actual gamma events included in the selection. A cut configuration that increases purity is referred to as "hard", whereas cuts that increase efficiency are called "loose". The principle is illustrated in fig. 3.7. Since low-energy showers exhibit larger statistical fluctuations, they are more likely to be rejected in hard selections. Consequently, a hard configuration leads to a higher energy threshold. While the choice of cut configuration is non-trivial and depends on the individual case, there is a point along the curve shown in fig. 3.7 that statistically optimizes the selection. This optimum however depends on the source intensity and spectral shape.

The HAP-Hd software offers three different cut configurations, named *loose*, *standard* and *hard*. The use of *loose* cuts is suitable for sources with steep spectra where the statistics benefit from higher counts through a lowered energy threshold, at the cost of increased systematics. The *hard* cut configuration is appropriate for sources with soft spectra (optimized for spectra $\propto E^{-2}$), where sufficient statistics are available to focus on higher energy ranges. Neither of the two cases apply here, hence the cut configuration used in this work is the *standard cuts* configuration, which together with the reconstruction method described in the following section is optimized for sources of 10% flux of the Crab nebula, with a spectrum $\propto E^{-2.6}$. The rejection threshold for ζ is set to 0.84, and in addition a minimum image amplitude of 60 p.e. is required for gamma-like events. Also, all events for which the image COG is separated by more than 2° from the source position are rejected.

3.2.4 Gamma Photon Reconstruction

After sorting out all events classified as background-like during the gamma-hadron separation procedure, the remaining gamma-like events are processed to reconstruct the properties of the incoming gamma photon. The method used in this work is called ImPACT [57] reconstruction. In the following, its working principles are described as they have been implemented in the HAP-Hd software. Like in the *(3D) model* analysis, the approach is based on fitting the shower image to a library of pre-generated templates. For the ImPACT reconstruction, the templates are produced using Monte Carlo (MC) air shower simulations, followed by ray-tracing of the telescope optics and subsequent simulation of the electronics to generate the images. This allows to consider fluctuations within showers at large energies above 10 TeV, since no analytical approximations are required. In addition, optical and electronic aspects are accurately taken into account.
Showers are simulated at different points of a four-dimensional parameter space, spanned by zenith and azimuth angle, energy and impact distance of the gamma photon. For each of those points, a number of simulations between 600 and 300,000, depending on the gamma energy, is carried out. In addition, each of the events is simulated for different values of X_{Max} spread around the expected value for the respective gamma energy. Finally, a multi-dimensional linear interpolation algorithm is used to fill the gaps between the sampled points in the multi-dimensional parameter space. Thereby, an image template is available for any set of parameters within the ranges chosen for the simulations. During the reconstruction procedure, the parameters which best correspond to the recorded image are found by likelihood fitting of the cleaned image pixel values to the template library. Fig. 3.8 shows some exemplary image template histograms of pixel amplitudes for simulated showers at different impact distances.

The performance of the ImPACT reconstruction is evaluated in [57], again by use of Monte Carlo simulations for the four smaller H.E.S.S. telescopes. Here, the angular resolution is defined as the radius containing 68% of the reconstructed positions for a given point source. The method provides an angular resolution between $\sim 0.1°$ in the GeV range, and down to $\sim 0.03°$ in the TeV range, as is shown in fig. 3.9, which also displays the dependence of angular resolution on the zenith angle.
The accuracy of energy reconstruction is expressed as the fractional deviation of reconstructed energy from the value used in the simulation. The mean value and r.m.s. of the resulting distribution are then referred to as the energy bias and resolution, respectively. The values are shown fig. 3.10. Above ~ 500 GeV, the analysis shows a "safe energy" range suited for spectral reconstruction, with biases smaller than 10%. A large bias is seen at low energies, where only extreme events with large upwards fluctuations in the number of Cherenkov photons pass the selection cuts, leading to an over-estimation of gamma energies. The energy resolution lies between ~ 0.19 at lower energies, and up to ~ 0.07 at higher energies, as shown in 3.10.
Finally, the effective area for the H.E.S.S. telescopes is defined as the probability for both triggering and subsequent event-selection of a gamma photon, multiplied by the collection area. The latter, as described in sec. 2.2.1, corresponds to the size of the light pool illuminated by the Cherenkov flash, which is only slowly changing with the gamma photon energy. The triggering and selection probabilities however change significantly at different energies, as the weaker Cherenkov radiation from low-energy gamma photons is less likely to trigger the telescopes, whereas events in

the upper energy range are disfavoured in the selection cuts. The latter is due to the fact that higher energy showers produce broader images, which are to some degree rejected since images near the camera edges cannot be reconstructed well. Fig. 3.11 shows the effective area as a function of energy.
All the plots mentioned in this section additionally show the corresponding performance of the Hillas reconstruction method with two different cut configurations, *standard* and *hard*, optimized for different types of sources.

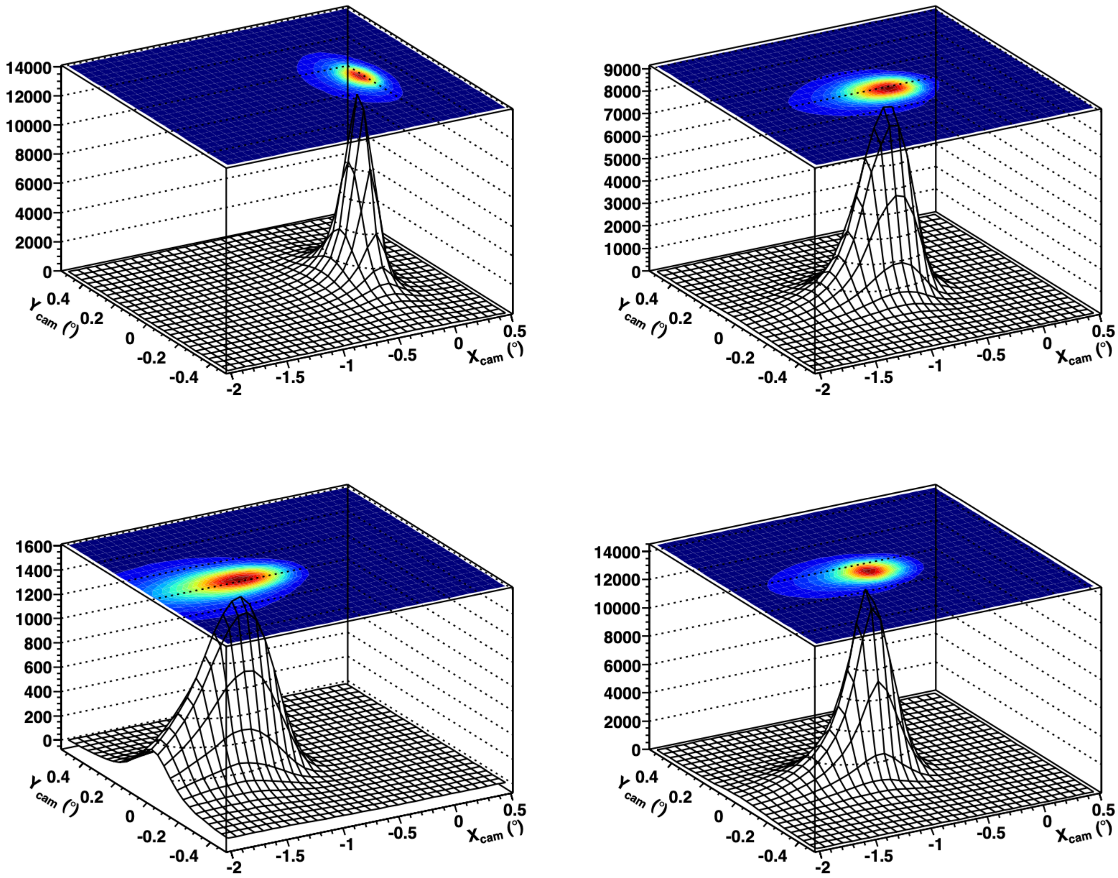

Figure 3.8: Pixel amplitude histograms for exemplary image template models used in the ImPACT reconstruction. All images result from MC simulations of a 1 TeV gamma photon, at different impact distances of 20 m (top left), 100 m (top right) and 200 m (bottom left), using the expected shower maximum of 200 g/cm^2. The bottom right histogram shows the template for an impact distance of 100 m and a shower maximum depth of 400 g/cm^2. Pixel amplitudes are given in p.e. per square degree. Taken from [57].

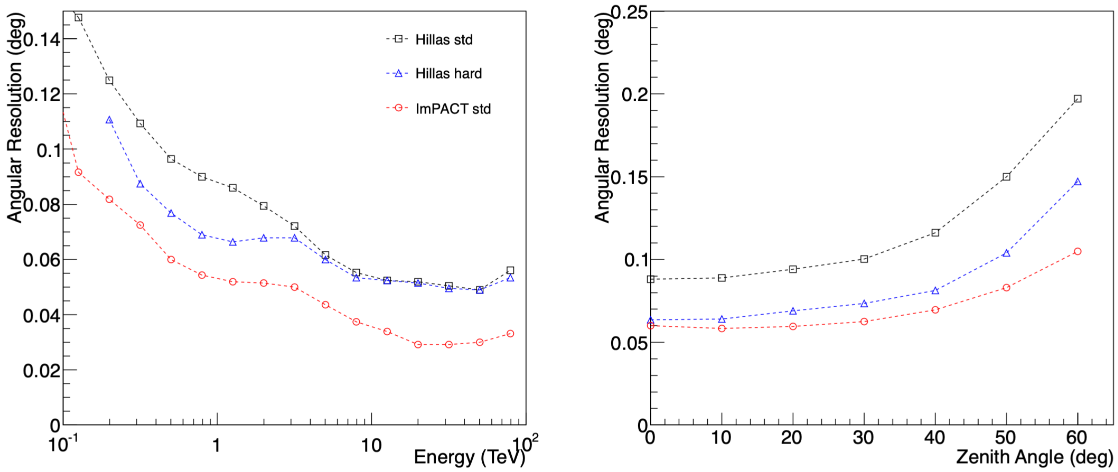

Figure 3.9: Angular resolution of the different reconstruction methods, defined as the 68% containment radius. The dependence on gamma-ray energy (left, fixed zenith angle of 20°), and on zenith angle (right, averaged over spectrum $\propto E^{-2}$) is plotted. Taken from [57].

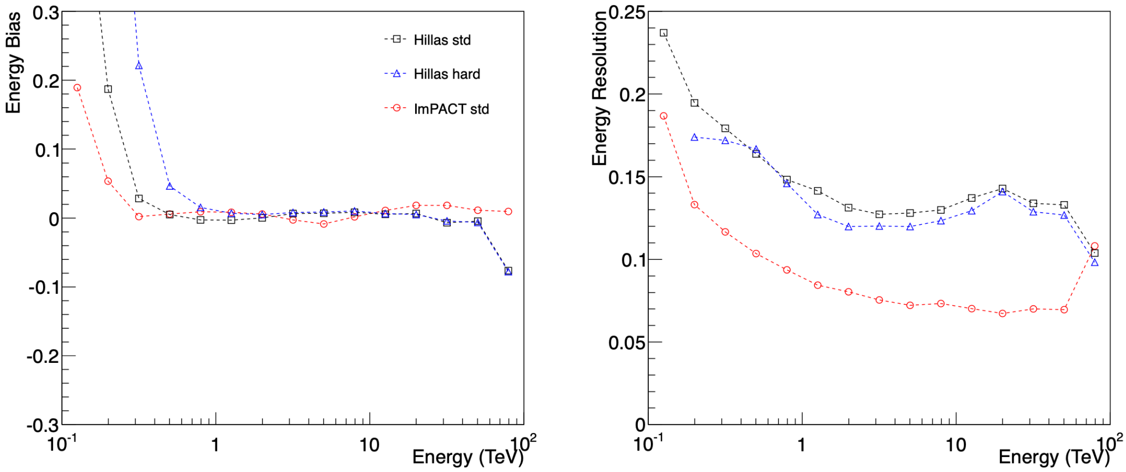

Figure 3.10: Energy bias (left) and resolution (right) of the different reconstruction methods, depending on the gamma-ray energy. Taken from [57].

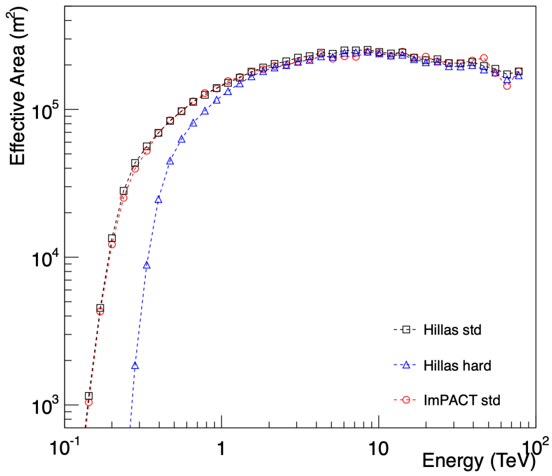

Figure 3.11: Effective area of the different reconstruction methods, depending on the gamma-ray energy. Taken from [57].

3.2.5 Background Subtraction

As a result of the reconstruction procedure, a list of gamma-like events is obtained, each containing all the reconstructed parameter values. In order to determine the possible presence of a gamma-ray source at the region of interest (ROI) in a sky map, it is necessary to estimate the expected number of background gamma-like events in the ROI tht are unrelated to the putative source. Those can be induced by hadronic events that passed the selection cuts, by electrons, or by actual gamma events unrelated to the source. The estimation is done by two similar, but different techniques, each of which is well suited for a specific purpose. Both of them are based on counting the number of gamma-like events at nearby sky regions that do not contain a known gamma-ray source, called off-regions. This provides an estimate of the number of background counts contained in the signal measured from the ROI, obtained from a defined on-region. The estimated number of background counts is then subtracted from the total number of on-counts. The remaining excess counts are evaluated by statistical methods to obtain a detection significance, which is interpreted as the probability of a gamma-ray source being present in the ROI. The underlying assumption in both methods is an isotropic background, and the differences lie in the ways of defining the off-regions. The applied statistical methods are the same in both cases.

Statistics of Background Subtraction

Observations of a particular ROI yield a number of on-counts N_{On} from a predefined on-region, as well as a number of off-counts N_{Off} from nearby regions which do not contain any known gamma-ray sources, hence the off-counts are assumed to be pure background events. Under the assumption of an isotropic background, the excess counts N_{Exc} from the ROI are then calculated as

$$N_{\mathrm{Exc}} = N_{\mathrm{On}} - \alpha \cdot N_{\mathrm{Off}}, \tag{3.5}$$

where α is a normalization factor accounting for the different sizes between the on- and off-regions, and also for instrumental acceptance-related differences discussed in the next paragraph. In a simplistic approach, the excess could be interpreted as the number of counts that originate from a source in the ROI. However, since an excess can always be induced by statistical fluctuations of the background signal, this could lead to the false detection of a non-existent source. Hence, a method is required which assesses the statistical significance of the measured excess, giving a probability that a source is actually present in the ROI. For that purpose, the measured on- and off-counts are evaluated by means of the likelihood ratio method proposed by Li and Ma [58]. This yields maximum likelihood estimates for the expected number of source counts $\langle N_{\mathrm{S}} \rangle$ and background counts $\langle N_{\mathrm{B}} \rangle$ measured within the ROI, as well as a significance S, which describes how strongly the measured counts indicate the presence of a source in the ROI.
The likelihood ratio method is a test to assess the probability of a hypothesis, referred to as the null hypothesis H_0, which assumes that the signal N_{On} consists of pure background events, hence $\langle N_{\mathrm{S}} \rangle_0 = 0$ and $\langle N_{\mathrm{B}} \rangle_0 = N_{\mathrm{On}}$. Following Poisson

statistics, the likelihood P_0 for measuring $N_{\text{On}}, N_{\text{Off}}$ under the null hypothesis is

$$\begin{aligned} & P_0\Big(N_{\text{On}}, N_{\text{Off}} \mid \langle N_{\text{S}}\rangle_0, \langle N_{\text{B}}\rangle_0\Big) \\ = \;& P\Big(N_{\text{On}} \mid \langle N_{\text{On}}\rangle = \langle N_{\text{B}}\rangle\Big) \cdot P\Big(N_{\text{Off}} \mid \langle N_{\text{Off}}\rangle = \langle N_{\text{B}}\rangle/\alpha\Big) \\ = \;& \frac{\langle N_{\text{B}}\rangle^{N_{\text{On}}} e^{-\langle N_{\text{B}}\rangle}}{N_{\text{On}}!} \cdot \frac{(\langle N_{\text{B}}\rangle/\alpha)^{N_{\text{Off}}} e^{-\langle N_{\text{B}}\rangle/\alpha}}{N_{\text{Off}}!}. \end{aligned} \tag{3.6}$$

Otherwise, under the alternative hypothesis H where no assumption is made, $\langle N_{\text{S}}\rangle = N_{\text{On}} - \alpha N_{\text{Off}}$ and $\langle N_{\text{B}}\rangle = \alpha N_{\text{Off}}$, and the likelihood P for measuring $N_{\text{On}}, N_{\text{Off}}$ is given by

$$\begin{aligned} & P\Big(N_{\text{On}}, N_{\text{Off}} \mid \langle N_{\text{S}}\rangle, \langle N_{\text{B}}\rangle\Big) \\ = \;& P\Big(N_{\text{On}} \mid \langle N_{\text{On}}\rangle = \langle N_{\text{S}}\rangle + \alpha\langle N_{\text{B}}\rangle\Big) \cdot P\Big(N_{\text{Off}} \mid \langle N_{\text{Off}}\rangle = \langle N_{\text{B}}\rangle/\alpha\Big) \\ = \;& \frac{\langle N_{\text{S}}\rangle + \alpha\langle N_{\text{B}}\rangle^{N_{\text{On}}} e^{-(\langle N_{\text{S}}\rangle+\alpha\langle N_{\text{B}}\rangle)}}{N_{\text{On}}!} \cdot \frac{(\langle N_{\text{B}}\rangle/\alpha)^{N_{\text{Off}}} e^{-\langle N_{\text{B}}\rangle/\alpha}}{N_{\text{Off}}!}. \end{aligned} \tag{3.7}$$

The best likelihood estimates $\langle \widehat{N}_{\text{B}}\rangle_0$ for H_0, as well as $\langle \widehat{N}_{\text{B}}\rangle, \langle \widehat{N}_{\text{B}}\rangle$ for H, are found by maximizing the likelihood functions P_0 and P with respect to the individual parameters, which yields

$$\langle \widehat{N}_{\text{B}}\rangle_0 = \frac{\alpha}{1+\alpha}(N_{\text{On}} + N_{\text{Off}}), \tag{3.8}$$

$$\langle \widehat{N}_{\text{B}}\rangle = \alpha N_{\text{Off}}, \tag{3.9}$$

$$\langle \widehat{N}_{\text{S}}\rangle = N_{\text{On}} - \alpha N_{\text{Off}}. \tag{3.10}$$

With this, the likelihood ratio λ is defined as

$$\begin{aligned} \lambda &= \frac{P_0\left(N_{\text{On}}, N_{\text{Off}} \mid \langle \widehat{N}_{\text{B}}\rangle_0\right)}{P\left(N_{\text{On}}, N_{\text{Off}} \mid \langle \widehat{N}_{\text{S}}\rangle, \langle \widehat{N}_{\text{B}}\rangle\right)} \\ &= \left[\frac{\alpha}{1+\alpha}\left(\frac{\mathrm{N_{On}} + \mathrm{N_{Off}}}{\mathrm{N_{On}}}\right)\right]^{\mathrm{N_{On}}} \cdot \left[\frac{1}{1+\alpha}\left(\frac{\mathrm{N_{On}} + \mathrm{N_{Off}}}{\mathrm{N_{Off}}}\right)\right]^{\mathrm{N_{Off}}}. \end{aligned} \tag{3.11}$$

Applying Wilks' theorem [59], under assumption of the null hypothesis and in the limit of large counts, the profile likelihood $-2\ln\lambda$ follows a χ^2-distribution of one degree of freedom, hence the quantity

$$S = \sqrt{-2\ln\lambda}, \tag{3.12}$$

follows a standard normal distribution of zero mean and unit variance. S is referred to as the significance, and it gives a measure for the probability of recording the obtained excess signal by chance if no source is present, where a higher significance indicates a lower chance probability. In gamma-ray astronomy, the detection threshold is conventionally set to $S = 5\sigma$. Using the right reparametrization, it can be shown that S is proportional to the square root of the total number of background counts expected in the on-region [60]. For a constant background, the number of counts grows linearly with exposure. Hence, the significance of a source signal is

expected to scale with the square root of the total exposure of the observations, which implies a scaling with the square root of the observation time.
The likelihood ratio method is also used to calculate confidence intervals for the obtained maximum likelihood value of the source counts $\langle \widehat{N}_\mathrm{S} \rangle$. For this, the profile likelihood $-2\ln\lambda$ is evaluated as a function of $\langle N_\mathrm{S} \rangle$, where a minimum is located precisely at the obtained value $\langle \widehat{N}_\mathrm{S} \rangle$. Parameter limits of confidence $1-c$ are then found at points along both directions of the $\langle N_\mathrm{S} \rangle$-axis for which the value of $-2\ln\lambda$ has increased with respect to the minimum value by the c percentile of a χ^2-distribution of one degree of freedom. This way, 1σ confidence limits are calculated for the determined excess rate. The procedure is illustrated in fig. 3.12, a more detailed description of the confidence limit calculation is given in [61]. The above calculations are again implemented in the HAP-Hd software, which yields the respective count numbers and significance values as part of the analysis results.

Acceptance

The acceptance model refers to the expected distribution of background events across the FoV in the absence of any gamma-ray sources. It can be determined through MC simulations for gamma-ray events, and is determined through background measurements for hadronic events, excluding regions with known gamma-ray sources. The simplest approach is the radial acceptance model, where the instrument response is assumed to be azimuthally symmetric around the pointing position of the telescope. In this description, the acceptance therefore depends only on radial distance from the pointing position, particle energy, zenith angle, and the applied cut configurazion. Fig 3.13 shows the radial acceptance for different zenith angle bands, as well as for different energy bands. Values obtained from MC simulations and measurements are stored within lookup tables available in the data base, providing the possibility to use the radial acceptance model for parts of the background subtraction that require its application.

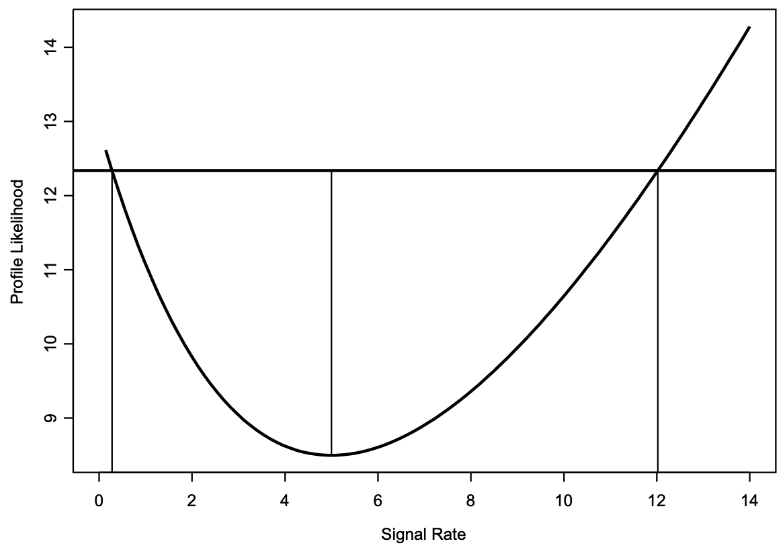

Figure 3.12: Graphical illustration of how confidence limits are obtained with the likelihood ratio method. Taken from [61].

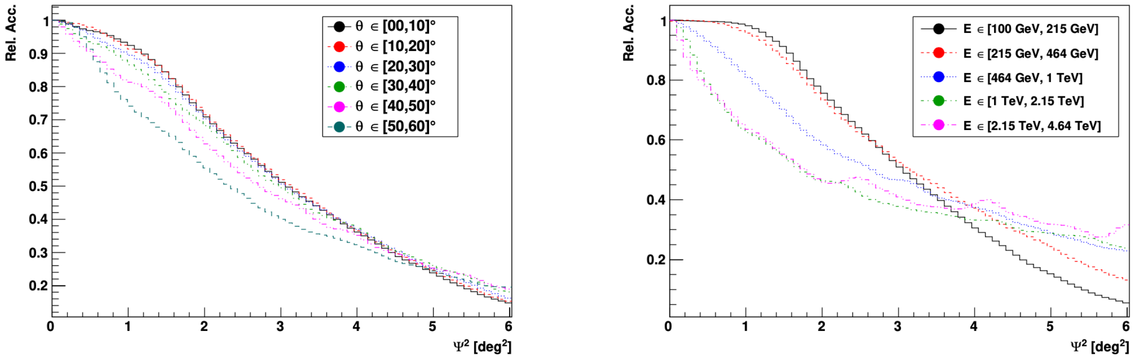

Figure 3.13: Radial acceptance of the H.E.S.S. I array of four telescopes, for different zenith angle bands (left) and different energy bands (right). The curves correspond to a version of the *model* reconstruction method, however for the ImPACT reconstruction they show a similar trend. Taken from [50].

Reflected Background Method

The reflected background is the first of two methods for background estimation used in this thesis, both of which are implemented in the HAP-Hd software. Here, the background is determined on a run-by-run basis. The off-regions are chosen at the same angular distance from the pointing position as the on-region, as is illustrated in fig. 3.14. They are spaced evenly across the field of view, however off-regions that intersect with predefined exclusion regions containing known gamma-ray sources are not considered. This method is only applicable if the separation between ROI and pointing position is large enough, which is the motivation for using the wobble observation mode described in sec. 3.1. The main advantage of the reflected background method is that the radial dependence of the acceptance does not need to be considered, since all regions are set at the same radial distance from

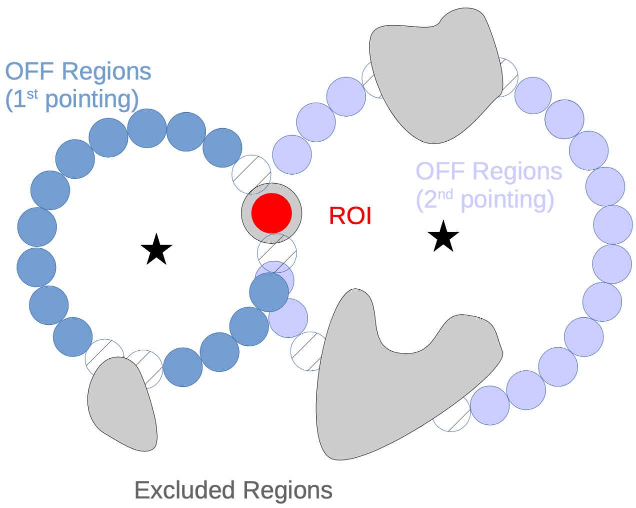

Figure 3.14: Illustration of the reflected background method for two runs with different pointing positions, indicated by the black stars. Excluded off-regions are shown as dashed circles. Taken from [50].

the pointing position. Under the assumption of a rotationally symmetric acceptance around the pointing positions, α is therefore calculated as the size ratio between the on-region and the off-regions. In particular, the assumption implies that the energy dependence of the acceptance is the same in the on- and in all off-regions, which makes this method well suited for spectral analysis of a source. On the other hand, the background regions differ for every pointing position of the telescope, which of course in general changes from run to run. Also, the method is not applicable for every region in the FOV. Hence, for the purpose of generating sky maps, a different approach is more advantageous.

Ring Background Method

The ring background method defines the off-region as an annulus around the ROI, as is illustrated in 3.15. Again, parts of the ring that overlap with exclusion regions are removed from the calculation. The choice of the annulus radius and area constitutes a trade-off between two effects: It should be large compared to the size of the ROI to reduce the effect of statistical fluctuations, however not too large as compared to the FoV to avoid the inclusion of additional systematics. In this method, the off-regions correspond to the same sky regions for every run. Therefore, rather than doing the calculation for every single run, the data of all runs can be merged (see sec. 3.3) so that background, excess, etc. are determined on the stacked data set to produce sky maps. In turn, since the off-regions of different runs are located at different distances from the pointing position, the radial acceptance model is used to include an additional weight factor in the calculation of α, for which values are retrieved from lookup tables. Since the energy dependence of the acceptance is not equal across the off region, spectral analysis would require a more complex acceptance determination with this method, which is why the previously described reflected background method is usually employed to derive energy spectra.

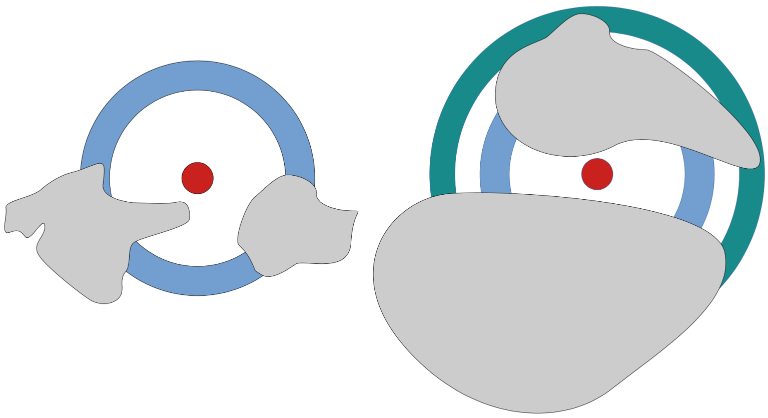

Figure 3.15: Illustration of the ring background method for a single run. The ROI is indicated as a red circle, the off-region as a blue or green annulus. Exclusion regions are shown as grey patches. *Left:* Normal ring background. *Right:* Adaptive ring background: The normal annulus (blue) has a large overlap with exclusion regions, hence the radius is expanded (green) for sufficient acceptance. Taken from [50].

A slight variation of the procedure is the adaptive ring method, which is useful in crowded regions like the galactic plane, where large parts of the ring would be excluded due to the large amount of neighboring sources. To avoid this, the radius of the annulus is adapted to the data set. More precisely, the radius is expanded until the area of the annuls, with exclusion regions removed, contains at least four times the acceptance of the on-region.

3.3 Phase Folding and Binning

Once the number of measured excess counts is determined, the next step is to derive light curves. The generation of orbital light curves requires a transformation of data points, which in general can be runs, events, flux values etc., from the time domain into the phase domain, established by the orbital modulation of the GRLB system. This requires the knowledge of the orbital period P and the definition of a zero-phase time value T_0, which in principle can be chosen arbitrarily. Then, each data point corresponding to a time t is assigned to a phase $\phi \in [0, 1)$, which is used to parameterize the orbital motion of the system. This process is called phase-folding, and the relation between t and ϕ is given by

$$\phi = \frac{t - T_0}{P} \bmod 1. \tag{3.13}$$

Since counts are generally limited in TeV observations, runs that fall into similar ranges of orbital phase are stacked together in a process referred to as merging, where time resolution is reduced for the benefit of higher statistics. For this, the numbers for on- and off-counts, as well as exposure time, are summed over all runs to obtain a merged data set. The merged normalization ratio α_{Tot} is calculated as

$$\alpha_{\mathrm{Tot}} = \frac{\sum_{\mathrm{r}} \alpha_{\mathrm{r}} N_{\mathrm{Off,r}}}{\sum_{\mathrm{r}} N_{\mathrm{Off,r}}}, \tag{3.14}$$

where r indicates that the respective quantity corresponds to a single run. For the procedure of phase folding, the whole phase range $[0, 1)$ is divided into a number of equal-sized intervals, called phase bins. All runs whose phase, given by equation (3.13), lies within the same phase bin are then merged into one data set, and the flux is calculated for each phase bin from the merged data, according to the procedure explained in the next section. It is in principle possible that over the 28 min duration, a run is included in two different phase bins, a case which requires special treatment. However, this special case does not occur for the data analyzed in this work. In a similar fashion, for the generation of night-wise light curves, all runs that were conducted during the same night are merged, and subsequently flux values are calculated for the respective merged data sets. Time stamps for each night are calculated as the weighted average of mid-run times of the corresponding runs, using the run durations as weights.

For this work, the calculation of phase values and time stamps, as well as the subsequent grouping of different runs, is implemented in a custom Python code. The subsequent procedure of merging the resulting groups of runs is again carried out by application of the HAP-Hd software.

3.4 Flux Calculation

In general, the differential flux $\frac{\mathrm{d}\Phi}{\mathrm{d}E} = \frac{\mathrm{d}^3 N}{\mathrm{d}A\,\mathrm{d}t\,\mathrm{d}E}$ is defined as the number of measured particles per energy, time and surface area. Integrating over any energy range then yields the flux $\Phi = \frac{\mathrm{d}^2 N}{\mathrm{d}A\,\mathrm{d}t}$ over that range. In a simple approach, the flux can be calculated as the number of measured counts within the specified range, divided by the exposure $\xi = A_{\mathrm{Eff}} \cdot \Delta t$, where Δt is the observation time. However, as previously discussed, the effective area is itself dependent on energy, i.e. $\xi(E) = A_{\mathrm{Eff}}(E) \cdot \Delta t$, assuming that $A_{\mathrm{Eff}}(E)$ remains constant in time, which is justified for a short enough Δt. Also, count statistics are generally limited due to low fluxes. Consequently, a more sophisticated method is required to obtain flux values with reasonably small errors. The flux calculation procedure used in this work follows an approach based on aperture photometry, with the underlying assumption of a constant source spectrum.

3.4.1 Spectrum Determination

The spectrum is derived from a fit to the whole data set, for which all analyzed runs are merged. The model used to describe the spectral shape $\mathrm{d}\Phi/\mathrm{d}E$ of a source is a power law defined as

$$\frac{\mathrm{d}\Phi}{\mathrm{d}E} = \Phi_0(E_0) \cdot \left(\frac{E}{E_0}\right)^{-\Gamma}, \tag{3.15}$$

where $\Phi_0(E_0)$ is the differential flux normalization at the normalization energy E_0, and Γ is the spectral index.

The method applied to determine the spectral parameters is called forward-folding. It is an approach that considers the variation of acceptance, energy resolution and effective area with different zenith angles δ and angular distances ψ of the source from the pointing position. Also, changes in optical efficiency ϵ due to the wear of the instruments are taken into account. For different bands in (δ, ψ, ϵ), the expected gamma-ray count rate n_γ in a reconstructed energy bin $[E_1, E_2]$ is given by

$$n_{\gamma,(\delta,\psi,\epsilon)} = \int_{E_1}^{E_2} \mathrm{d}E_{\mathrm{R}} \int_0^{\infty} \mathrm{d}E_{\mathrm{T}}\ \mathcal{R}_{(\delta,\psi,\epsilon)}(E_{\mathrm{R}}, E_{\mathrm{T}}) \cdot \mathcal{A}_{(\delta,\psi,\epsilon)}(E_{\mathrm{T}}), \cdot \frac{\mathrm{d}\Phi}{\mathrm{d}E_{\mathrm{T}}}(E_0, \Gamma), \tag{3.16}$$

where $E_{\mathrm{T}}, E_{\mathrm{R}}$ indicate the true and reconstructed energies, $\mathcal{R}$ is the resolution function and $\mathcal{A}$ is the acceptance. The resolution function is defined as the probability density for obtaining a reconstructed E_{R} from a given E_{T}. All values for $\mathcal{R}$ and $\mathcal{A}$ are retrieved from lookup tables available in the data bank, which contain the results of MC simulations performed with different combinations of values for the relevant parameters. Energy bins are defined by a maximum splitting of the used energy range such that within each bin, a minimum significance of 2σ is guaranteed. The used energy range is adapted to the ranges in which events were registered, however constrained in a way that a reasonably small energy binning is still possible. For each energy bin, the resulting value of n_γ is then compared to the measured count rate, and the overall best-fitting spectral parameters Φ_0, Γ are found via log-likelihood maximization, where the flux normalization is calculated at a value of E_0 that minimizes the correlation between the fit parameters. The error values for each fit parameter are given as the square root of the corresponding diagonal element of the covariance matrix, corresponding to 1σ confidence intervals. The method implicitly assumes a constant source flux. While this is a viable assumption for a first approach, it needs to be kept in mind that in the case of strong source variability the approximation loses its validity. For a more detailed description of the spectrum reconstruction, see [54] and references therein. The procedure of spectrum determination is carried out using the HAP-Hd software.

3.4.2 Aperture Photometry

Once the spectral parameters are determined, the flux can be calculated. As we will see in a moment, the only actually relevant spectral parameter is the index Γ. The flux value is calculated from three quantities. First, the actual excess counts N_{Exc}, which are obtained from the analysis. Second, considering the exposure ξ of the observations, the number of expected counts N_{Exp} from the source under the assumption of a constant emission spectrum $\mathrm{d}\Phi/\mathrm{d}E$ is given by

$$N_{\mathrm{Exp}} = \int \frac{\mathrm{d}\Phi}{\mathrm{d}E} \cdot \xi(E)\,\mathrm{d}E, \tag{3.17}$$

where the effective area induces an energy dependence of the exposure, which is assumed to be constant in time for the given integration. The range of integration can in theory be infinite, since the integrand is naturally enveloped by the effective area that only spans a finite range of energies. In practice however, the expected counts are calculated as a sum over fine-sized energy bins, which lie within the energy range ΔE of all recorded events, according to

$$N_{\mathrm{Exp}} \approx \sum_{E_{\mathrm{i}} \in \Delta E} \left.\frac{\mathrm{d}\Phi}{\mathrm{d}E}\right|_{E_{\mathrm{i}}} \cdot \xi(E_{\mathrm{i}}), \tag{3.18}$$

Again, the values for the effective area in each of the energy bins are retrieved from lookup tables, which were produced through MC simulations. The calculation of expected counts is carried out using the HAP-Hd software. The expected counts are calculated for each run, and the results are summed in order to obtain a number of expected counts for a merged data set.
Finally, the third quantity is a reference flux Φ_{Ref}, which is simply the assumed source spectrum integrated over a specific energy range $[E_{\mathrm{Min}}, E_{\mathrm{Max}}]$:

$$\Phi_{\mathrm{Ref}} = \int_{E_{\mathrm{Min}}}^{E_{\mathrm{Max}}} \frac{\mathrm{d}\Phi}{\mathrm{d}E}\,\mathrm{d}E. \tag{3.19}$$

The flux Φ is then ultimately calculated as the ratio between measured and expected counts, multiplied by the reference flux:

$$\Phi = \frac{N_{\mathrm{Exc}}}{N_{\mathrm{Exp}}} \cdot \Phi_{\mathrm{Ref}}. \tag{3.20}$$

The caclulation of equations (3.19) and (3.20) is performed with a custom C++ code that supplements the existing HAP-Hd software. Equation (3.19) is calculated by evaluating the analytical expression of the integrated power-law spectrum defined in equation (3.15):

$$\Phi_{\mathrm{Ref}} = \frac{\Phi_0(E_0)}{E_0^{-\Gamma}} \left[E_{\mathrm{Max}}^{1-\Gamma} - E_{\mathrm{Min}}^{1-\Gamma}\right]. \tag{3.21}$$

As can be shown when inserting equations (3.18) and (3.19) in equation (3.20), by definition of the assumed power-law spectral shape, the differential flux normalization can be taken out of the integral as it is independent from energy, and therefore effectively cancels out between Φ_{Ref} and N_{Exp} without influencing the value of Φ. In principle, the energy ranges $E_{\mathrm{Min}}, E_{\mathrm{Max}}$ for the reference flux could again be chosen arbitrarily. However, bearing the physical meaning in mind, they should not strongly deviate from the energy range in which the data was taken, which dictates the range in which the power law spectrum was fitted and therefore the spectral assumption is justified. Nonetheless, since this work is focused on relative flux changes, the choice of reference flux can in this case be regarded as a formality, given that it only influences the absolute flux levels.

3.5 Variability Search

Once the orbital and night-wise light curves are generated, the final step of the analysis is to look for signs of orbital variability and periodicity. This requires methods that can estimate the probability that the recorded signal was obtained from a source whose signal is - or is not - intrinsically modulated, ideally also yielding the value of the modulation period if required. In this work, we apply a simple χ^2-test to investigate the phase-folded orbital light curves for variability. On the nightwise light curves, the epoch-folding method proposed by Leahy [32] and a generalized Lomb-Scargle [30][24] period search are applied.

3.5.1 χ^2-Test

The χ^2-Test is a procedure commonly used for analyzing statistical data sets. In general, the purpose of the method is to test how well a data set, in our case the orbital light curve, is represented by a given model referred to as the null hypothesis H_0, which in our case is the assumption of a non-variable, constant source. The χ^2-Test estimates the probability of obtaining the data at hand under the assumption that H_0 is true. Hence, the method can be thought of as a goodness-of-fit statistics, describing how well the orbital light curve is fitted by a constant flux. The test statistic χ^2 is defined as

$$\chi^2 = \sum_{i=1}^{n_{\mathrm{B}}} \frac{(F_{\mathrm{i}} - \langle F \rangle)^2}{\Delta F_{\mathrm{i}}^2}, \tag{3.22}$$

where n_{B} is the number of phase bins with corresponding flux data points, F_{i} and ΔF_{i} are the flux values and half-widths of the corresponding 1σ confidence interval for the respective phase bin, and $\langle F \rangle$ is the weighted average flux over all phase bins, using the 1σ errors as weights. The calculation of χ^2 is implemented into a dedicated Python script. For large enough counts, the probability distribution of χ^2 is well approximated by a chi-square distribution χ^2_ν, where the number of degrees of freedom ν is given by $\nu = n_{\mathrm{B}} - 1$. The goodness of fit can then be expressed as the reduced chi-square $\frac{\chi^2}{\nu}$, where a fit is better the closer this number is to one. Alternatively, the p-value can be calculated as

$$p = \int_{\chi^2}^{\infty} \chi^2_{n_{\mathrm{B}}-1}(x)\, \mathrm{d}x, \tag{3.23}$$

indicating the probability of measuring values that deviate *at least* as much as the data set from the null hypothesis H_0, or in our specific case, the probability of measuring an orbital light curve *at least* as variable as the one analyzed, assuming that the source is constant. The calculation of χ^2 is manually implemented as a Python code, whereas the p-value is obtained by using the *chi*2 sub-module of the *scipy* Python-package [62].
For our purposes, a reduced chi-square close to one and equivalently a high p-value denote good agreement between the data and a constant flux, therefore indicating that any orbital variability is either absent or not detectable within the error limits of the data set. Accordingly, a large reduced chi-square and low p-value can be interpreted as an indication of variability in the orbital light curve.

3.5.2 Light Curve Periodicity

Two different methods are applied on the night-wise light curves to test them for periodicity.

The Epoch-Folding Method

The epoch-folding method proposed by Leahy [32] builds on the previously described χ^2-test. The concept is to fold the light curve on a set of n_P different orbital periods $\mathbf{P} = (P_1, ..., P_{n_\mathrm{P}})$ and subsequently evaluating the χ^2-test statistic on each of the resulting orbital light curves. If the source has an intrinsic modulation period, the orbital light curve should show strong deviations from a constant flux when folded on periods close to the correct value, white noise is expected otherwise. A plot of the obtained χ^2-values against the respective periods can then be interpreted as a periodogram, yielding high values for periods close to the intrinsic modulation period. The orbital light curves and χ^2-values for the different orbital periods are calculated with the previously described procedures. In order to identify a positive result, a detection threshold T_c for a confidence level c is defined as

$$1 - c = n_\mathrm{P} \int_{T_c}^{\infty} \chi^2_{n_\mathrm{B}-1}(x)\,\mathrm{d}x, \tag{3.24}$$

where n_B is again the number of phase bins used. Hence, for a chosen probability level c, a threshold T_c is defined such that if for any period the resulting χ^2 surpasses T_c, there is a probability of c that it *did not* happen by chance. To approximate T_c for different levels of c, both sides of the equation are plotted into the same graph. A solution of equation (3.24) is then estimated graphically at the intersection between the two curves.

The Generalized Lomb-Scargle Periodogram

Additionally, we apply the generalized Lomb-Scargle [30][24] period search to the night-wise light curves. The method is equivalent to fitting a model function $y(t; f_\mathrm{i})$ for different candidate frequencies f_i to the light curve. The fit model is given by

$$y(t; f_\mathrm{i}) = y_{0,\mathrm{i}} + A_\mathrm{i} \sin\left(2\pi f_\mathrm{i}(t - \phi_\mathrm{i})\right), \tag{3.25}$$

where $y_{0,\mathrm{i}}$, A_i and ϕ_i are free parameters. For each fit result, the χ^2 goodness-of-fit is evaluated as

$$\chi^2_\mathrm{i} = \sum_{\mathrm{j}=1}^{n_\mathrm{t}} \frac{(F(t_\mathrm{j}) - y(t_\mathrm{j}; f_\mathrm{i}))^2}{\Delta F(t_\mathrm{j})^2}, \tag{3.26}$$

where n_t is the number of data points of the light curve, and F and ΔF are the flux values and corresponding 1σ-errors. The periodogram is then calculated as

$$P(f_\mathrm{i}) = \frac{1}{2}[\chi^2(H_0) - \chi^2_\mathrm{i}], \tag{3.27}$$

where $\chi^2(H_0)$ is again the test statistic for a constant flux model, calculated analogously to the definition in equation (3.22), but applied to the night-wise light curve data. Therefore, for a set of candidate frequencies f_i, the periodogram indicates how much better the data is fit by a sine function of the respective frequency as compared to a constant flux.
False alarm probability (FAP) levels, indicating the probability that a peak of a given magnitude is generated from noise, are calculated according to the bootstrap method. For this, the periodogram is calculated for many random resamplings of the data, where time values are kept but flux values are permuted randomly. Each resampling gives a maximum power of the periodogram, and for a large enough number of resamplings, the distribution of maxima approximates the distribution for the case of no signal periodicity. FAP levels are then derived from this resulting distribution. For a detailed review of the Lomb-Scargle period search and its different variations, see [63].
The generalized Lomb-Scargle search is performed by using the implementation in the *astropy*[64] Python-package. Since the method should not depend on any previous assumption of periodicity, it is applied on the night-wise light curves.

3.6 Phase Map Subtraction for 4FGL J1405.1-6119

For the case of 4FGL J1405.1-6119, the aim is not only to investigate the presence of orbital modulation, but also to develop a method that allows to separate the signals received from the GRLB and adjacent sources, as explained in sec. 2.1.1. For this, we make use of the expected correlation between the TeV and X-Ray light curves. Based on the data from [16], the orbital phase is divided into two blocks:

- A "bright" phase ϕ_B of increased X-ray flux,
- A "dark" phase ϕ_B of reduced X-Ray flux.

All runs that pass the detection criteria are merged into two data sets, corresponding to the two phase blocks. The approach for signal separation consists in generating two TeV sky maps with the H.E.S.S. data, one for each of the phase blocks, respectively. Afterwards, the "dark" map is subtracted from the "bright" map. The non-varying signal of adjacent sources should thereby cancel out, while the expected augment of the 4FGL J1405.1-6119 signal during the bright phase should lead to a residual excess registered at the source position.
On-count sky maps are generated by evaluating the merged data sets at different test positions in the FoV, corresponding to the different pixels of the map. The

resulting maps are correlated with a top-hat filter corresponding to the on-region size, in order to account for the fact that counts are determined for regions of finite extension, hence neighboring pixel values are not statistically independent. In a similar fashion, exposure maps are generated in units of expected on-counts for an assumed flat background of gamma-like events in the absence of sources, calculated pixel-wise and also correlated.
The subtracted counts map ΔN_{On} is calculated pixel-wise as

$$\Delta N_{\mathrm{On}} = N_{\mathrm{On}}(\phi_{\mathrm{B}}) - \frac{\xi_{\mathrm{On}}(\phi_{\mathrm{B}})}{\xi_{\mathrm{On}}(\phi_{\mathrm{D}})} \cdot N_{\mathrm{On}}(\phi_{\mathrm{D}}), \tag{3.28}$$

where ξ denotes the respective numbers of expected on-counts, representative of the different exposures. The approach constitutes an analogy to the background subtraction explained in sec. 3.2.5, replacing on- and off-counts in equation (3.5) with bright- and dark-phase counts, and α with the ratio α_ξ of on-exposures. Analogously, a subtracted significance map S_Δ is calculated pixel-wise according to equation (3.12), applying the same substitutions. The sign of ΔN_{On} is applied to S_Δ, allowing negative significance values in the case of a negative subtracted count value. The method implicitly assumes equal rates of background counts measured for both phase blocks. On first order, this can be verified at the positions of other, non-variable sources in the FOV, where no remaining signal should appear. To further assert the legitimacy of this assumption, the distribution of S_Δ at non-exclusion regions, meaning regions of the FoV with no present TeV source, denoted $N_{\Delta,\mathrm{B}}$, is plotted as a histogram. Following the statistical properties of the significance S as defined in eq. (3.12), if the assumption is correct, the values should follow a standard normal distribution of zero mean and unit variance. If however systematics are induced by different background levels between the dark and bright phase, the resulting distribution would deviate from the expected shape. Therefore, the possible presence of systematics is investigated by fitting a Gaussian distribution N_{G} to the histogram, defined as

$$N_{\mathrm{G}}(S) = \frac{N_0}{\sqrt{2\pi}\sigma_{\mathrm{G}}} \cdot \exp\left(-(S-\mu_{\mathrm{G}})^2/2\sigma_{\mathrm{G}}^2\right), \tag{3.29}$$

where the amplitude N_0, center μ_{G} and sigma σ_{G} are free fitting parameters. Further, in order to quantify the symmetry of $N(S_{\Delta,\mathrm{B}})$, the skewness is calculated as

$$\tilde{\mu}_3(N_{\Delta,\mathrm{B}}) = \left\langle \left(\frac{S_{\Delta,\mathrm{B}} - \langle S_{\Delta,\mathrm{B}} \rangle}{\sigma(N_{\Delta,\mathrm{B}})} \right)^3 \right\rangle, \tag{3.30}$$

where angular brackets indicate the average value and σ is the standard deviation. The skewness is a measure for asymmetry of a probability distribution. A positive or negative value indicates the presence of systematics with the inclination to over- or underestimate, respectively, the source signal. In addition to the Gaussian fit, by which a possible shift or broadening of the distribution can be derived from the best-fitting parameters, a non-zero skewness indicates an asymmetrical deformation of the distribution from a Gaussian shape.
The sky maps are obtained by using the HAP-Hd software. All subsequent steps of the calculation are executed with a custom python code.

Analysis Procedure and Results

4.1 HESS J1832-093

4.1.1 Data Selection

The data base is searched for H.E.S.S. observational runs with a pointing offset of no more than 2° from the source position, yielding a pre-selection of 233 runs corresponding to 98.1 h observation time. After applying the spectral criteria selection and eliminating runs with less than one telescope or missing DSTs, a run list of 203 runs is obtained, corresponding to 92.2 h of observation time, acquired between May 2004 and June 2020. The histogram in fig. 4.1 shows the distribution of runs over the whole period of data taking. Also, fig. 4.2 shows the distribution of runs across the orbital phase, where runs are phase-folded and binned by their start time, using the 87.106 d period reported in [15], with $T_0 = 54524.9979255$ (MJD[1]). For a data set spanning 16 years, a variation of the period by ±0.005 d leads to a maximum phase shift of the data points of $\Delta\phi \approx \pm 0.004$, which is significantly smaller than the phase bin size of 0.1, indicating that the accuracy of the period is sufficient for the time span of the H.E.S.S. data set. The plot shows that phase bin 0.0-0.1 is not covered by the current set of observations.

4.1.2 Analysis Procedure

The steps of gamma reconstruction, background rejection/subtraction and spectrum fitting are performed by use of the HAP-Hd software version 18.11. An on-region radius of 0.1° is used, which is a standard value that optimizes the signal-to-noise ratio for typical galactic point sources. This The results of this analysis are obtained with the reflected background method. Standard HAP exclusion regions are used, where the exclusion region of the source itself is corrected to match the identified position given in eq. (2.3) and to have a radius of 0.24°. This eliminates some residual signal from regions of assumed pure background, which could otherwise result in an erroneous reconstruction of the source signal. A list of the relevant used exclusion regions is given in tab. 4.1. The reconstruction and background steps are performed for each run individually, and run-wise results are then further merged according to the respective purposes. The combined data set of all merged spectral runs yields a total excess of 476.2 counts with a detection significance of 9.7σ.
A spectrum fit is performed between 0.2 and 10 TeV, the resulting best-fit parameters are given in tab. 4.2. Fig. 4.3 shows the measured spectrum, together with the

[1] Short for modified julian date.

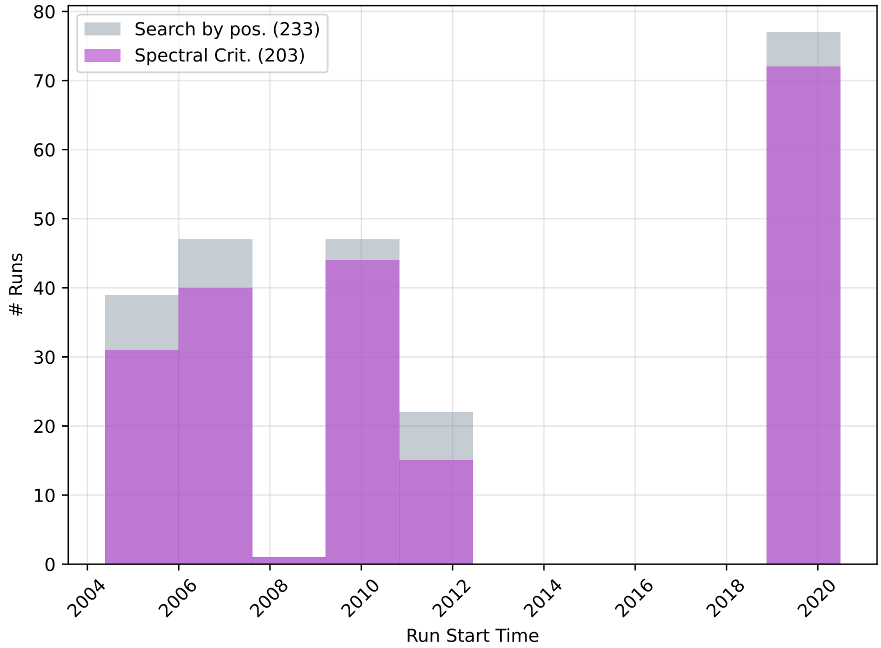

Figure 4.1: Distribution of runs over the period of data taking, showing the pre-selection found with the source position (grey) and the spectral runlist obtained after selection procedure (purple). Numbers in the legend indicate the total number of runs.

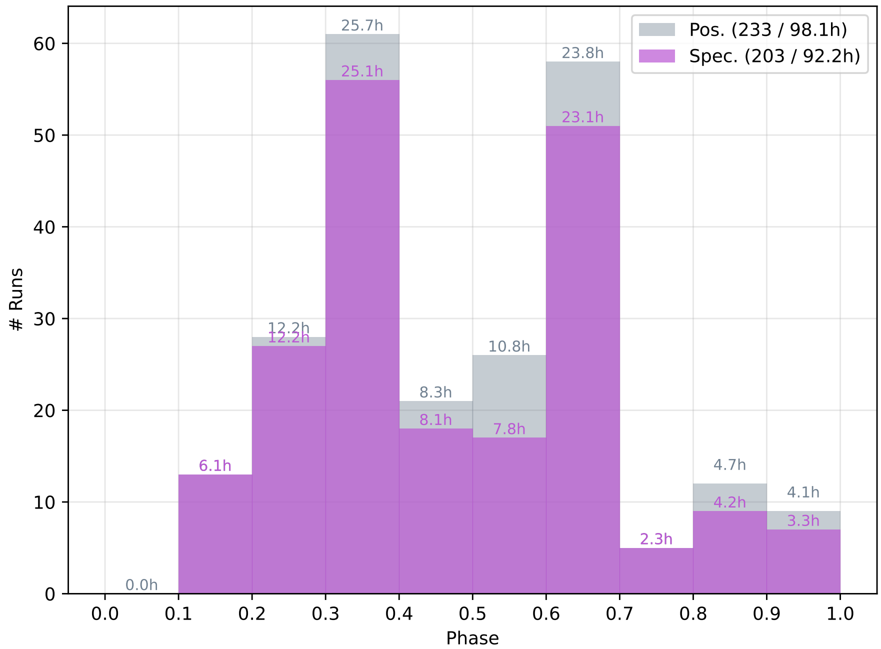

Figure 4.2: Distribution of runs over the orbital phase, folded with the 87.106 d period. The histogram shows the pre-selection found with the source position (grey) and the spectral runlist obtained after selection procedure (purple). Numbers above the bars show the observation time of the respective bin. Numbers in the legend indicate the total number of runs and the total observation time.

best-fit power law spectrum and the corresponding error margins.
Runs are assigned into ten different phase bins by folding the run start time on the 87.106 d period, and subsequently merged into one data set per phase bin. The obtained spectral index of 3.1 is then used to calculate the flux on each phase bin individually by means of the aperture photometry method described in sec. 3.4.2, where the reference flux is calculated with an integration range between 0.21 and 30 TeV. The flux calculations result in the orbital light curve shown in fig. 4.4. In a similar way, runs are merged night-wise, and the respective flux values are calculated to generate nightly-binned data points. For visualization purposes, the result is phase-folded on the 87.106 d period, which is shown in fig. 4.5.

4.1.3 Orbital Variability and Periodicity

A χ^2-test is performed on the obtained orbital light curve, resulting in a reduced chi-square of 1.17, which is equivalent to $p = 0.31$. The result is not indicative of any orbital modulation.
To search for periodicity in the night-wise light curve on a broad range, a Lomb-Scargle period search is performed for periods between 25 and 1000 d. The resulting periodogram is shown in fig. 4.6. No significant peaks that indicate a periodicity of the signal at a confidence level above 1σ are found.
In addition, motivated by a similar approach used in [15], a close range around the identified period is investigated with the epoch-folding method. A binning of $n_{\mathrm{B}} = 8$ is chosen to evaluate $n_{\mathrm{P}} = 1000$ periods between 86 and 88 d. Since the method for calculating FAP levels defined in eq. (3.24) depends on n_{B}, a total of 330 periods for which the binning results in uneven coverage of less than 8 bins are removed, leaving 670 data points for the power spectrum, which is shown in fig. 4.7. To obtain threshold values for different confidence levels, a solution of eq. (3.24) is estimated graphically from the plot shown in fig. 4.8, giving $T_{2\sigma} \approx 14$ and $T_{3\sigma} \approx 21.5$. No significant levels of periodicity are retrieved at a confidence level above 2σ within the searched range.
A more detailed discussion of the results is given in sec. 5.1.

l [°]	b [°]	radius [°]
20.31	0.19	0.2
21.51	0.37	0.3
21.51	-0.87	0.3
21.93	-0.11	0.3
22.47	-0.17	0.24
23.24	-0.32	0.63
23.27	0.3	0.2
25.14	-0.1	0.79
25.17	-0.11	0.79

Table 4.1: Standard HAP exclusion regions used for the HESS J1832-093 analysis. Positions are given in galactic coordinates, following the HAP convention within exclusion region files.

Parameter	Best-Fit Value
Γ	3.1 ± 0.2
E_0	$0.4024\,\mathrm{TeV}$
$\Phi_0(E_0)$	$3.7 \pm 0.4 \cdot 10^{-12}\,\mathrm{TeV}^{-1}\mathrm{cm}^{-2}\mathrm{s}^{-1}$
$\Phi(> 1\,\mathrm{TeV})$	$9.8 \pm 3.0 \cdot 10^{-14}\,\mathrm{cm}^{-2}\mathrm{s}^{-1}$

Table 4.2: Best-fit values of the power law parameters from eq. (3.15) as derived from the spectrum fit, including the integrated flux above 1 TeV resulting from the best-fit model. Errors correspond to 1σ confidence intervals.

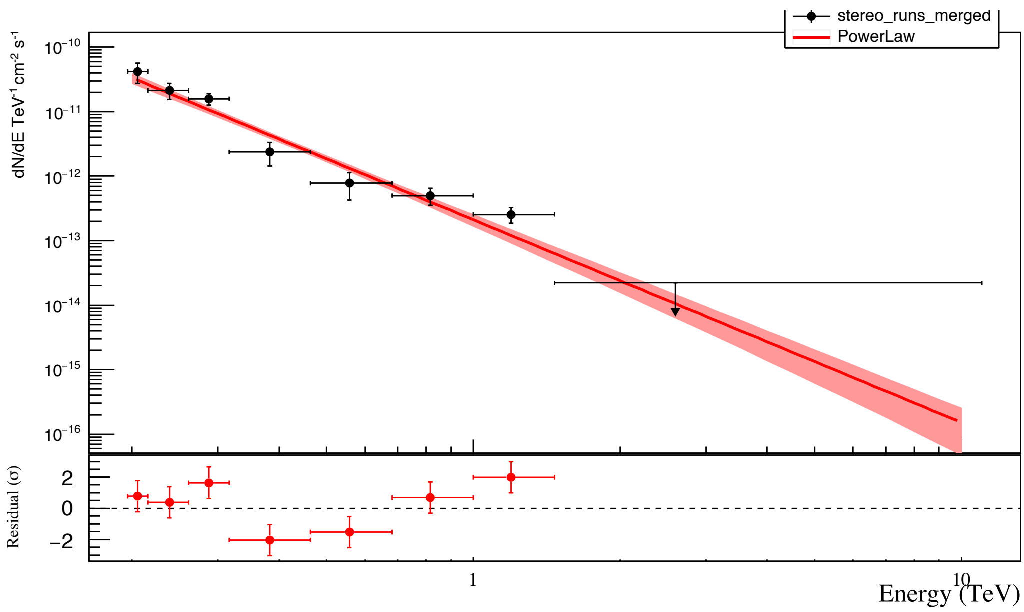

Figure 4.3: Spectrum obtained from the data (black) and best-fit power law model (red), also showing the fit residuals on the bottom.

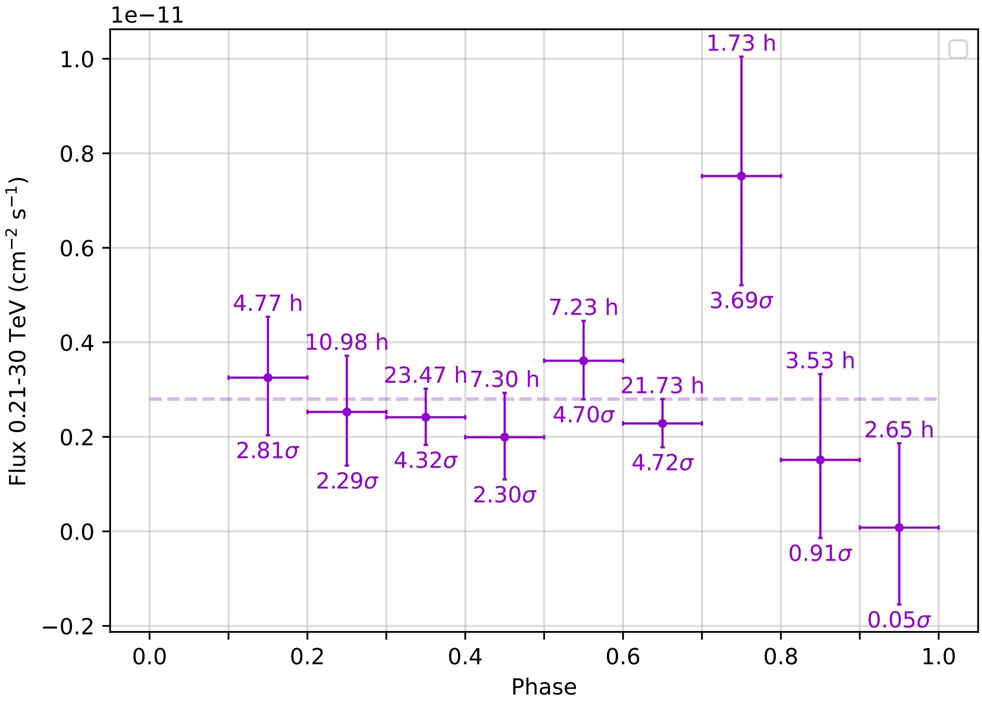

(a) Single Orbit

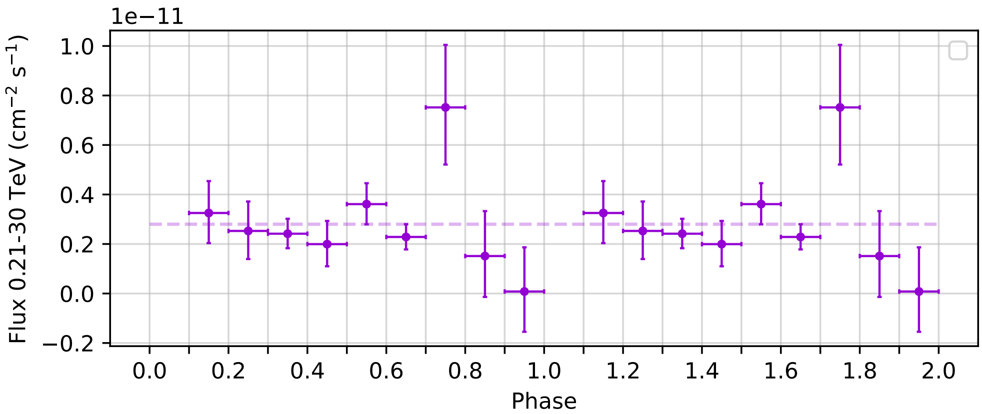

(b) Two Orbits

Figure 4.4: Phase-binned orbital light curve obtained from the HESS J1832-093 observations, folded on the 87.106 d period with T_0 = 54524.9979255 (MJD). The average flux level is indicated with dashed lines. In 4.4a, the numbers above and below the data points indicate the observation live time and detection significance for each bin, respectively. In 4.4b, the same data is plotted over two periods for visualization purposes.

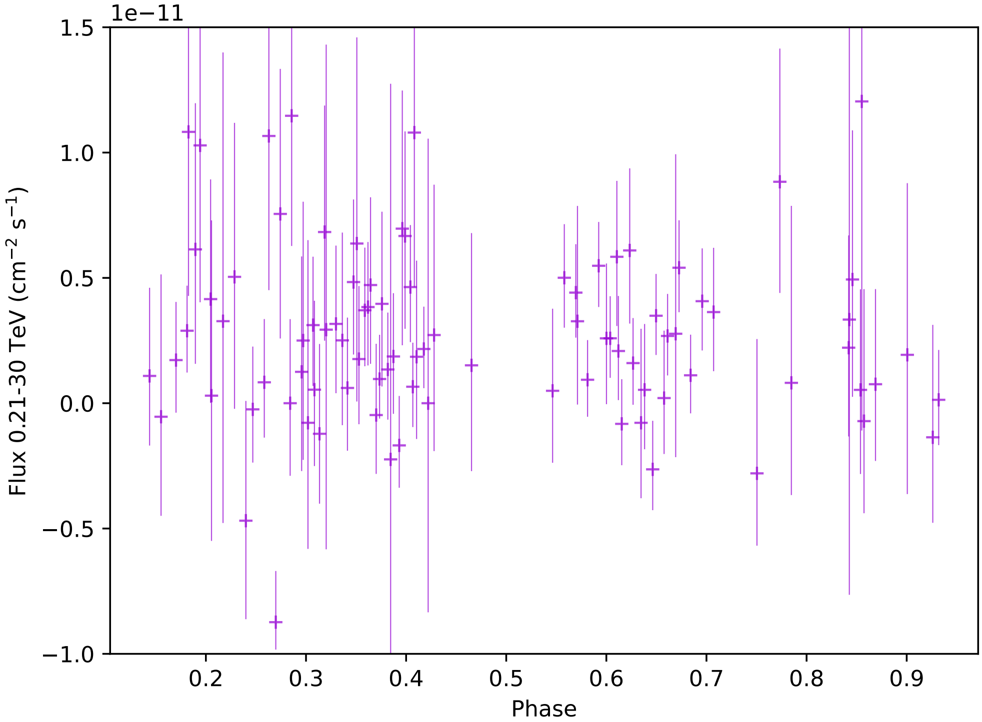

Figure 4.5: Nightly-binned orbital light curve obtained from the HESS J1832-093 observations, folded on the 87.106 d period with $T_0 = 54524.9979255$ (MJD).

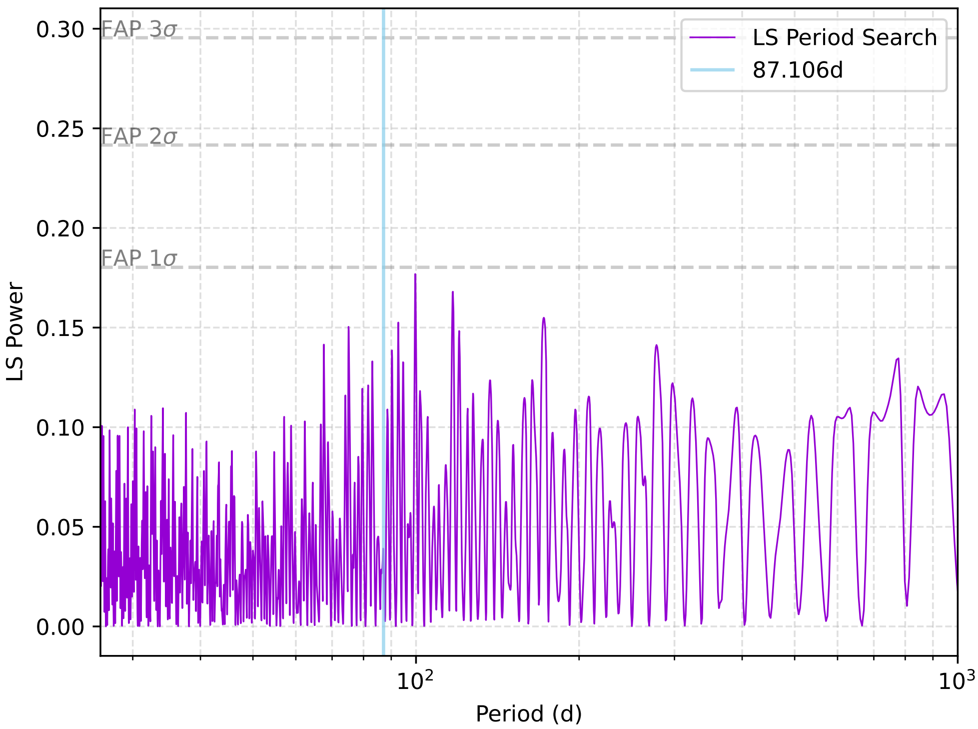

Figure 4.6: Lomb-Scargle periodogram obtained from period search on the HESS J1832-093 night-wise light curve. Grey dashed lines indicate the different FAP levels.

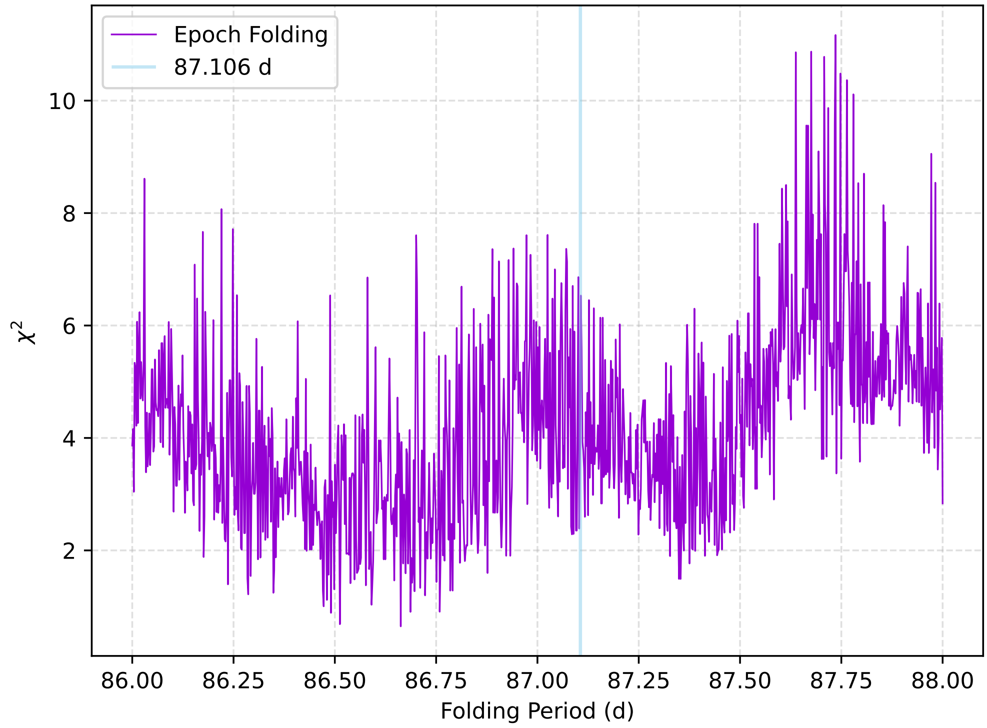

Figure 4.7: Periodogram obtained through epoch folding on the HESS J1832-093 data.

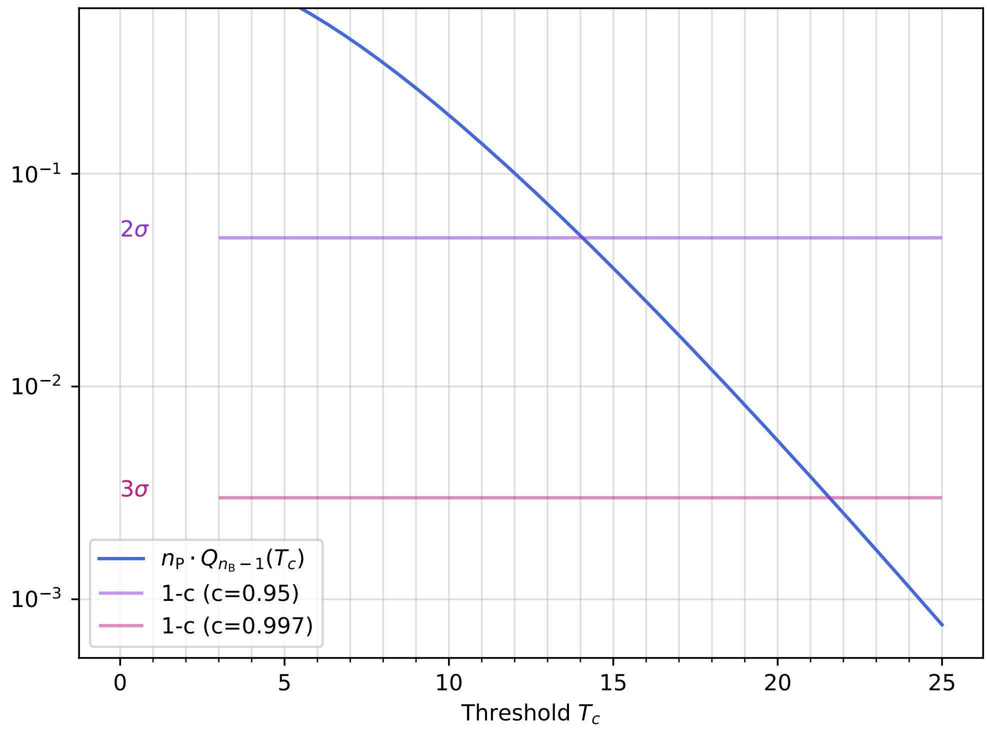

Figure 4.8: Plot used to graphically estimate the solution of eq. (3.24) at the intersections between lines, in order to obtain threshold values T_c for different confidence levels c in the epoch-folding periodogram.

4.2 4FGL J1405.1-6119

4.2.1 Data Selection

A pre-selection of runs within 2° of the source position includes 256 runs, corresponding to 99.0 h of observation time. For the analysis of 4FGL J1405.1-6119, both spectra and sky maps are retrieved. Therefore, two different data sets are extracted from the pre-selection by applying the detection criteria and the spectral criteria, respectively. This results in a detection run list, and a more restrictive spectral run list.
After selecting for detection criteria, number of telescopes and DSTs, a detection run list of 152 runs is obtained, corresponding to 70.4 h of observation time, acquired between April 2005 and June 2021. For the analogous procedure with spectral criteria, a spectral run list of 138 runs with a total of 64.1 h of observation time is obtained, spanning the same time range.
Fig. 4.9 shows the distribution of runs over time, fig. 4.10 shows the distribution of runs across the orbital phase, folded on the period reported in [16] of 13.7135 ± 0.0019 d, at $T_0 = 56498.7$ (MJD). Varying the period within the given error margin for a data set spanning 16 years leads to a maximum phase shift of $\Delta\phi \approx 0.06$, which is within one phase bin of size 0.1. An exceedingly large number of runs from 2015 and 2016 is excluded during the selection procedures. At that time, the camera of CT1 was in an experimental status, therefore the telescope is generally excluded from runs that were performed during that period. This leads to an increased number of runs being excluded with less than two participating telescopes. In addition, telescopes are excluded from runs from that time predominantly due to "hardware" missing pixels.

4.2.2 Analysis Procedure

The analysis is performed the same way as for HESS J1832-093, first using the spectral run list. Standard HAP exclusion regions are used, where two custom regions are added to improve the covering of signals originating from the source and its immediate surroundings. Details of the relevant exclusion regions are given in tab. 4.3, where the two first rows indicate the customized exclusion regions. A total excess of 198.9 with a significance of 7.7σ is found. However, due to the signal contamination from adjacent sources in the FOV, this cannot be interpreted as a detection significance for 4FGL J1405.1-6119.
The spectrum fit is performed between 0.237 and 10 TeV, best-fit values are shown in tab. 4.4 and the result of the fit is shown in fig. 4.11.
Runs are merged into ten different phase bins, the obtained spectral index of 3.3 is used for flux calculation. The reference flux is calculated between 0.1 and 100 TeV. The resulting orbital light curve is shown in 4.12. The phase-folded light curve with night-wise binning is shown in fig. 4.13.
Since the signal is contaminated by neighboring sources, the retrieved spectral index is not representative of the source emission spectrum. To assess the potential effect of the spectral index on the result, the orbital light curve is additionally calculated using an index of 2.5, which is a typical value for galactic point sources. While the

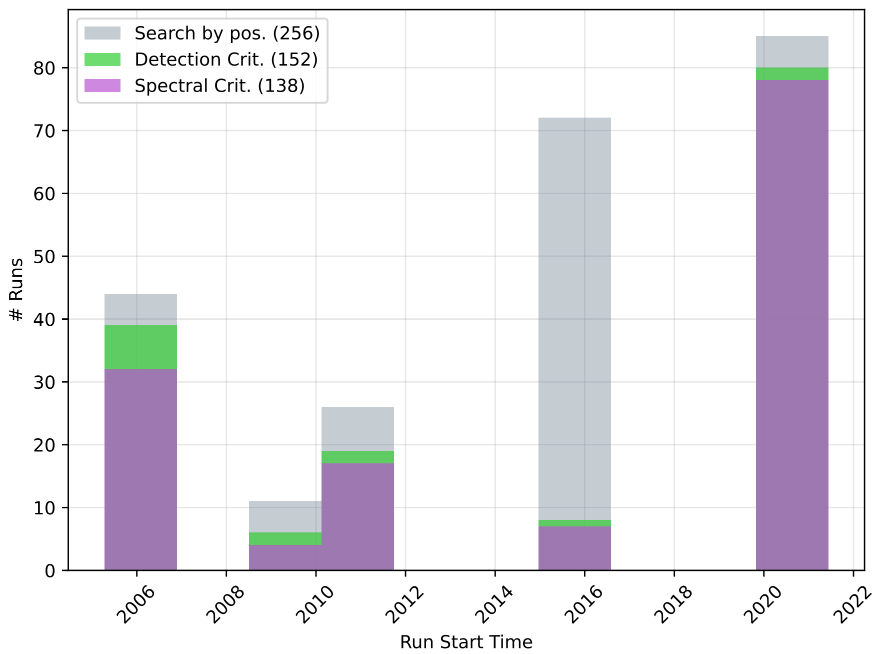

Figure 4.9: Distribution of runs over the period of data taking, showing the pre-selection found with the source position (grey) and both the detection (green) and spectral (purple) runlist, obtained after the respective selection procedures. Numbers in the legend indicate the total number of runs.

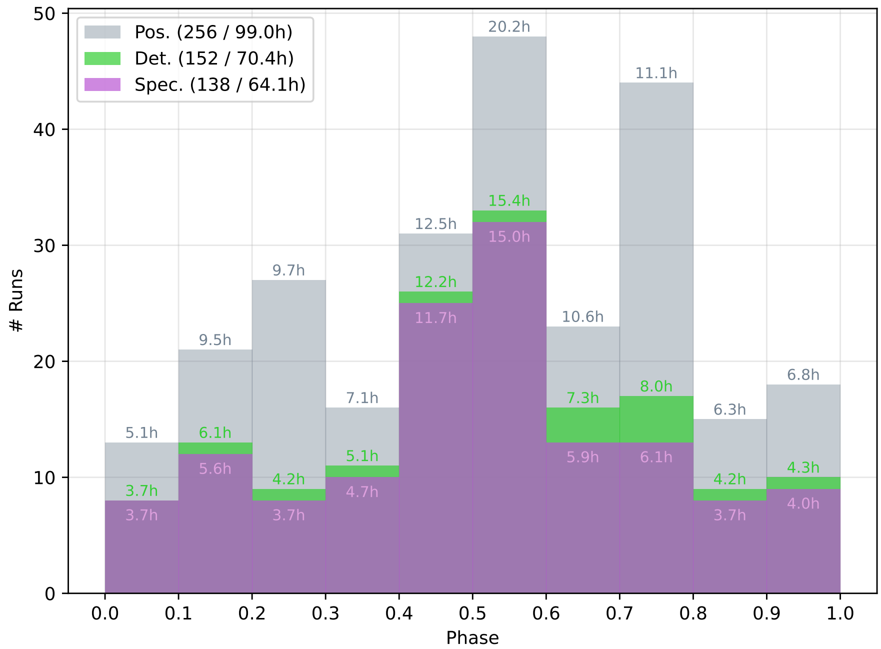

Figure 4.10: Distribution of runs over the orbital phase, folded with the 17.7135 d period. The histogram shows the pre-selection found with the source position (grey) and the spectral runlist obtained after selection procedure (purple). Numbers above the bars show the observation time of the respective bin. Numbers in the legend indicate the total number of runs and the total observation time.

absolute flux values are reduced, the use of a lower spectral index has no significant effect on the relative flux changes between the different phase bins.

4.2.3 Orbital Variability and Periodicity

A χ^2-test on the orbital light curve yields a reduced chi-square of 1.33, corresponding to $p = 0.22$. The result is not indicative of any orbital modulation.
A Lomb-Scargle period search is performed on the night-wise light curve for periods between 5 and 1000 d, the resulting periodogram is shown in fig. 4.14. No signal of periodicity surpassing a 2σ confidence level is found.

4.2.4 Phase Map Subtraction

The orbit of 4FGL J1405.1-6119 is divided into two blocks, corresponding to bright and dark phases, respectively. Based on the X-ray light curve from [16], the division is defined as

- Bright phase: $\phi \in [0.3, 0.8)$,
- Dark phase: $\phi \in [0, 0.3) \cup [0.8, 1.0)$.

The division is illustrated in fig. 4.15. Flux values are calculated for the two phase blocks. Fig. 4.16 shows the resulting orbital light curve with a binning of two, overlaid with the orbital light curve previously obtained with a binning of 10.

Maps are generated for both bright and dark phases, and the phase map subtraction procedure is performed. Fig. 4.18 shows the generated maps, intermediate results and the final subtracted significance map. A value of $S_\Delta = 2.41\sigma$ is found at the source position.
As previously explained, the method implicitly assumes that the background counts scale linearly with the background acceptance. In order to investigate the possible presence of systematic effects induced by a difference in the background signal between the two phases, the distribution of S_Δ at non-exclusion regions $N_{\Delta,\mathrm{B}}$ is fitted with a Gaussian distribution. The result is shown in fig. 4.17. The best-fit Gaussian has a center of $\mu_\mathrm{G} = 0.032 \pm 0.002$ and a sigma of $\sigma_\mathrm{G} = 1.031 \pm 0.002$. The skewness of the distribution is $\tilde{\mu}_3(N_{\Delta,\mathrm{B}}) = -0.09$. While the fit parameters are in strong accordance with a Gaussian shape, the distribution is evidently skewed towards negative values. This indicates the possible presence of a systematic effect that shifts the resulting subtracted significance towards lower values.

l [°]	b [°]	radius [°]
311.74	0.23	0.37
312.39	-0.27	0.1
311.77	1.25	0.2
311.7	0.11	0.25
312.16	-0.12	0.25
312.49	-0.57	0.25
313.24	0.15	0.4
313.4	0.2	0.55

Table 4.3: Exclusion regions used for the 4FGL J1405.1-6119 analysis. Positions are given in galactic coordinates, following the HAP convention within exclusion region files. The first two entries correspond to regions that were added manually, while the others are part of the standard HAP exclusion regions.

Parameter	Best-Fit Value
Γ	3.3 ± 0.3
E_0	$0.5907\,\mathrm{TeV}$
$\Phi_0(E_0)$	$1.5 \pm 0.2 \cdot 10^{-12}\,\mathrm{TeV}^{-1}\mathrm{cm}^{-2}\mathrm{s}^{-1}$
$\Phi(>1\,\mathrm{TeV})$	$1.1 \pm 0.4 \cdot 10^{-13}\,\mathrm{cm}^{-2}\mathrm{s}^{-1}$

Table 4.4: Best-fit values of the power law parameters from eq. (3.15) as derived from the spectrum fit, including the integrated flux above 1 TeV resulting from the best-fit model. Errors correspond to 1σ confidence intervals.

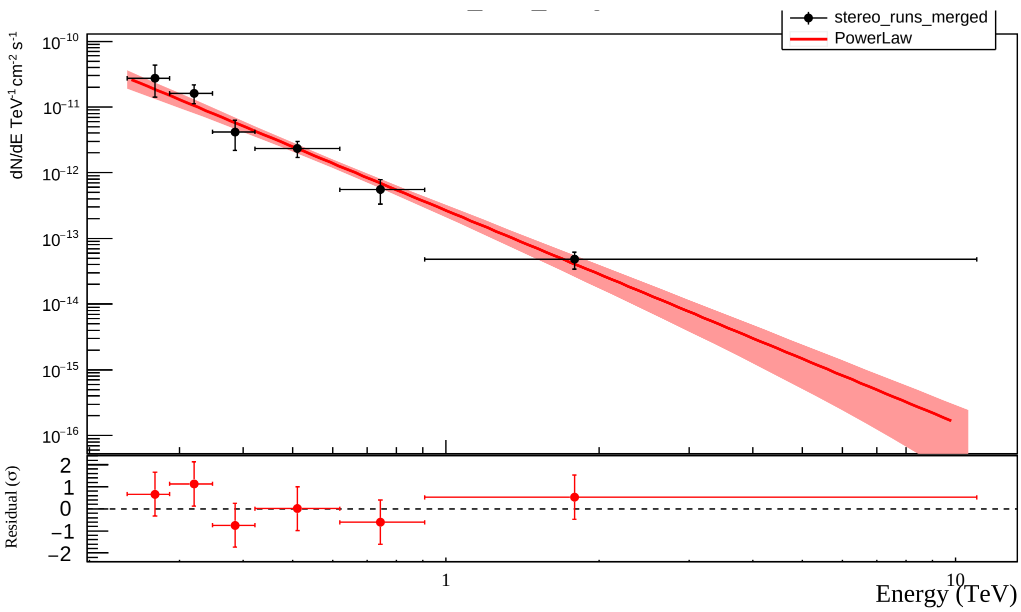

Figure 4.11: Spectrum obtained from the data (black) and best-fit power law model (red), also showing the fit residuals on the bottom.

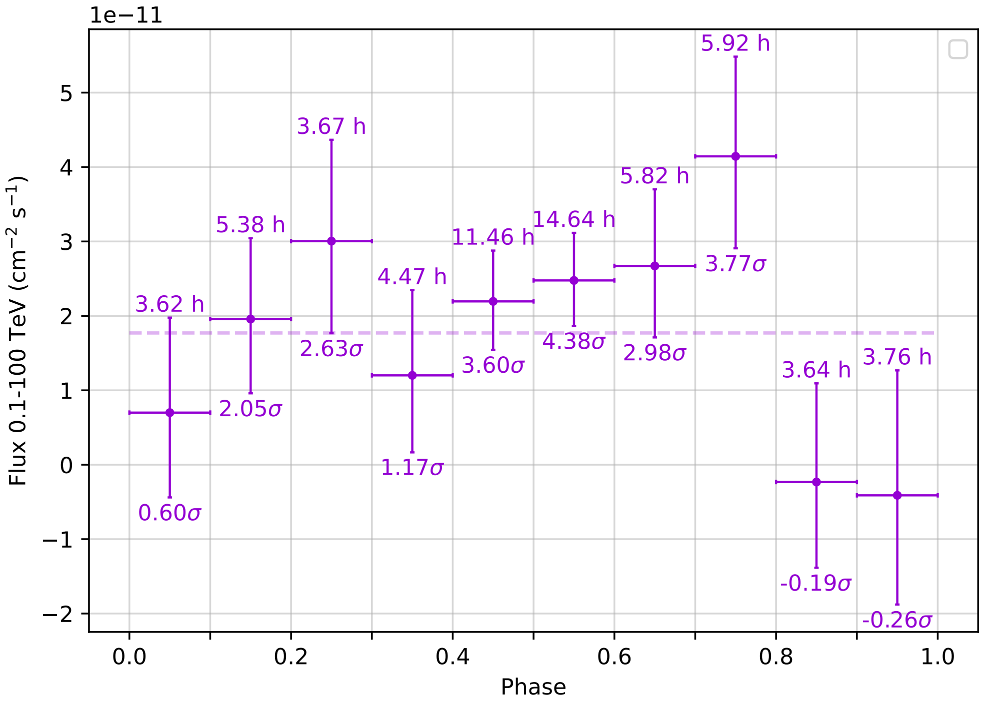

(a) Single Orbit

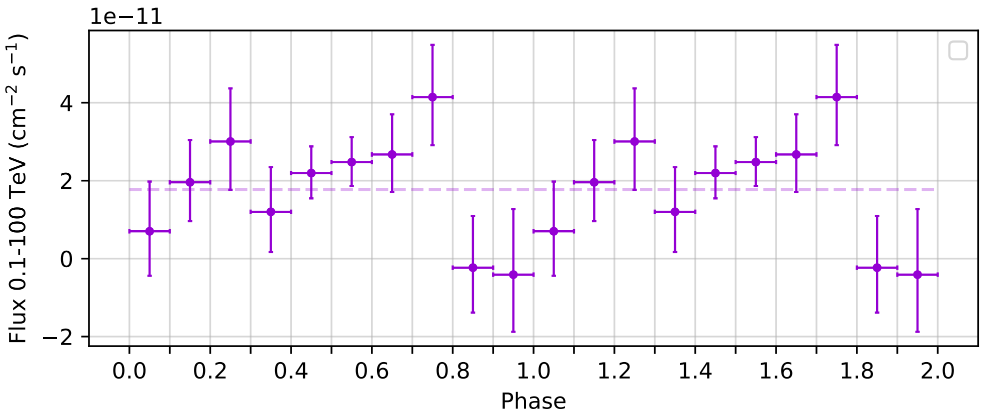

(b) Two Orbits

Figure 4.12: Phase-binned orbital light curve obtained from the 4FGL J1405.1-6119 observations, folded on the 13.7135 d period at $T_0 = 56498.7$ (MJD). The average flux level is indicated with dashed lines. In 4.12a, the numbers above and below the data points indicate the observation live time and detection significance, respectively, for each bin. In 4.12b, the same data is plotted over two periods for visualization purposes.

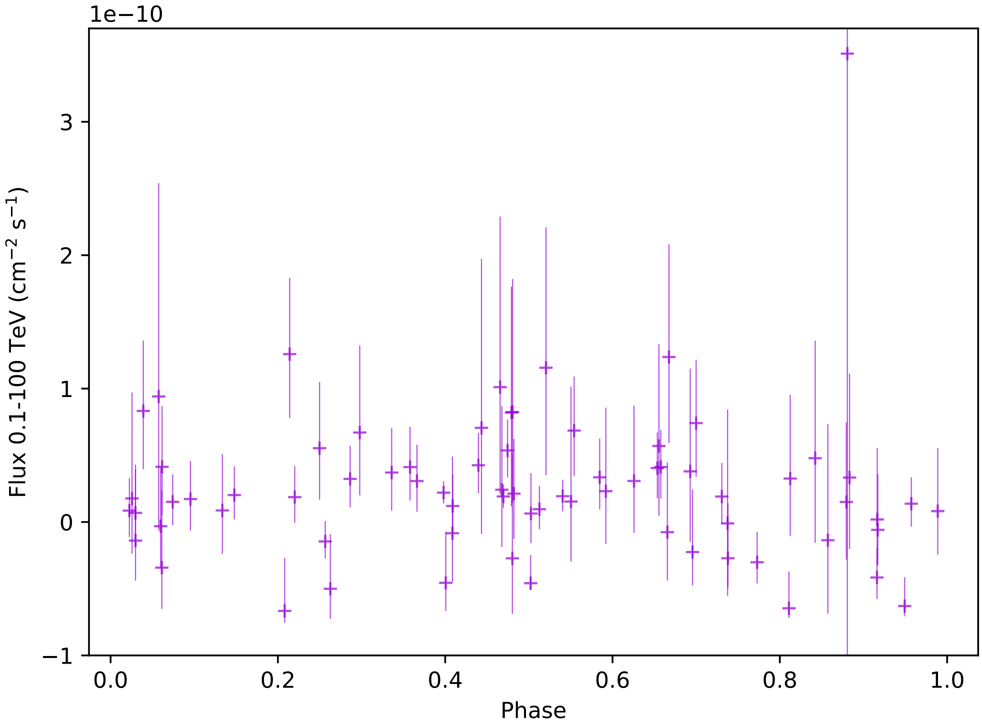

Figure 4.13: Nightly-binned orbital light curve obtained from the 4FGL J1405.1-6119 observations, folded on the 13.7135 d period at T_0 = 56498.7 (MJD).

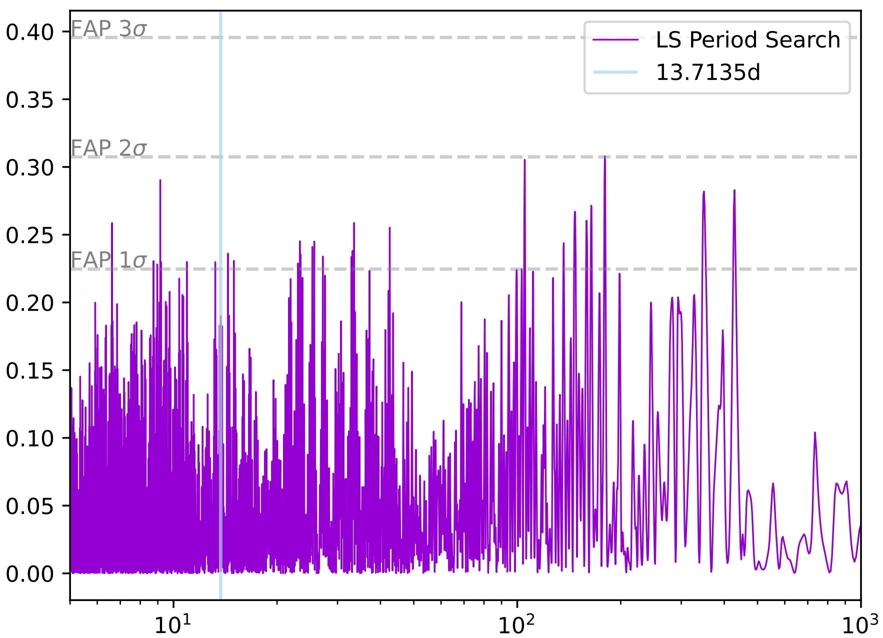

Figure 4.14: Lomb-Scargle periodogram obtained from period search on the 4FGL J1405.1-6119 data. Grey dashed lines indicate the different FAP levels.

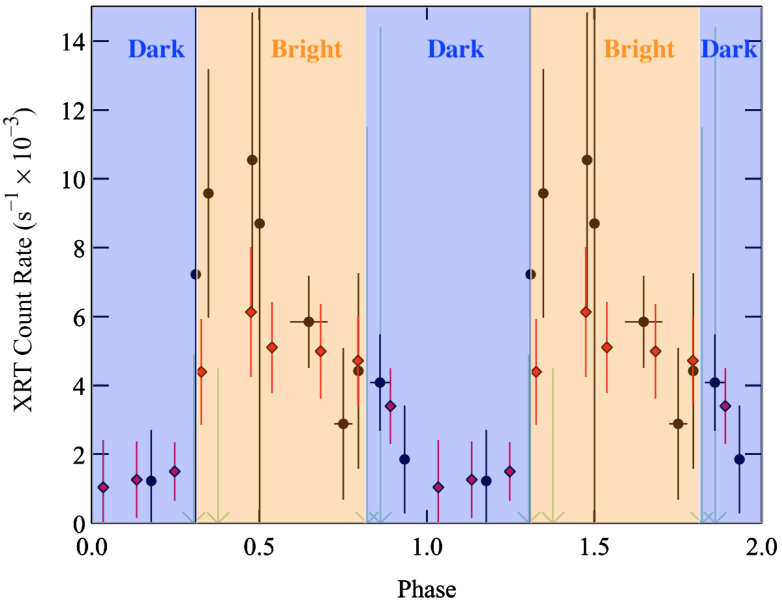

Figure 4.15: Illustration of the division of the orbital light curve into phases of increased ("bright") and reduced ("dark") X-ray flux. Adapted from [16].

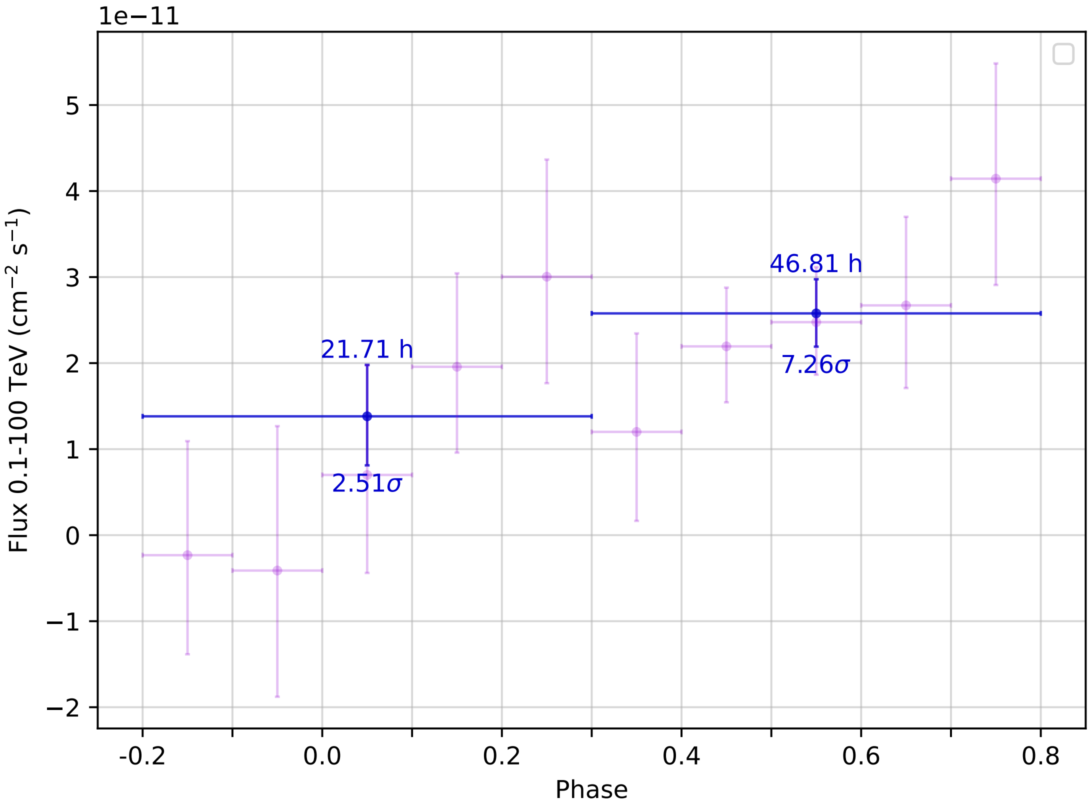

Figure 4.16: Flux values derived for the two phase blocks (blue). The numbers above and below the data points indicate the observation live time and detection significance, respectively, for each block. The orbital light curve with a binning of 10, as shown in fig. 4.12, is also plotted (purple). Note the shifted phase range between -0.2 and 0.8.

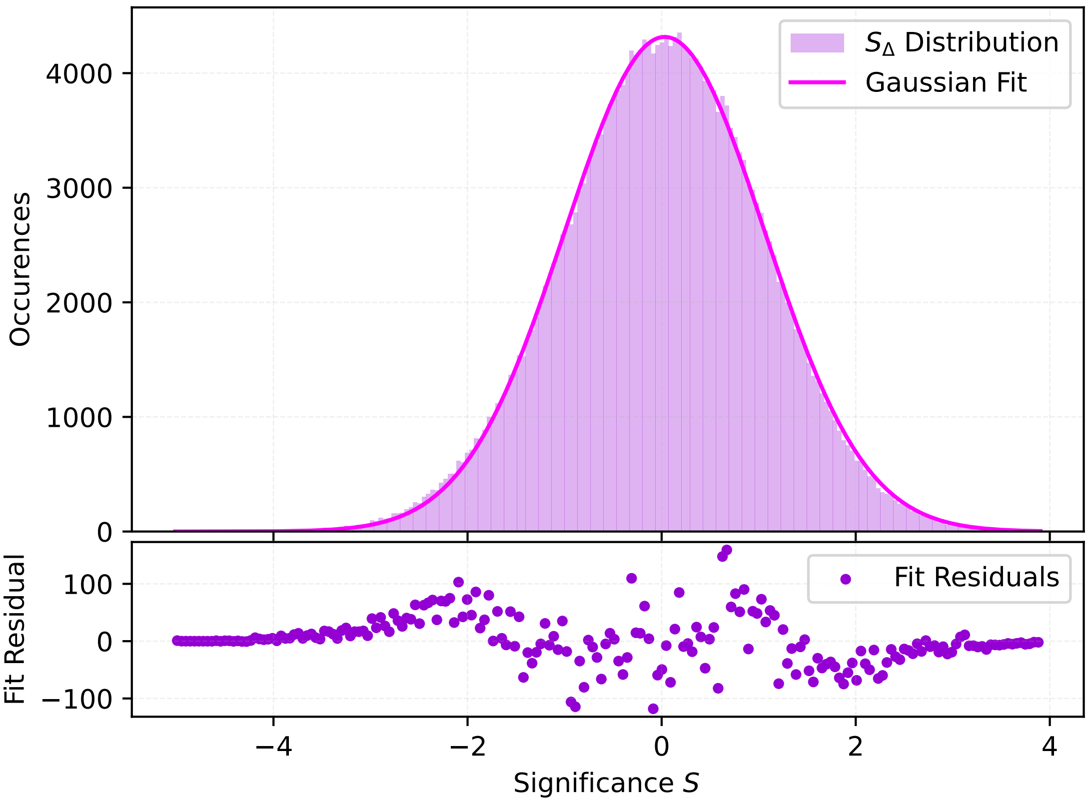

Figure 4.17: Distribution $N_{\Delta,\mathrm{B}}$ of values of S_Δ in pure background regions, fitted with a Gaussian distribution (top), also showing residuals of the fit (bottom).

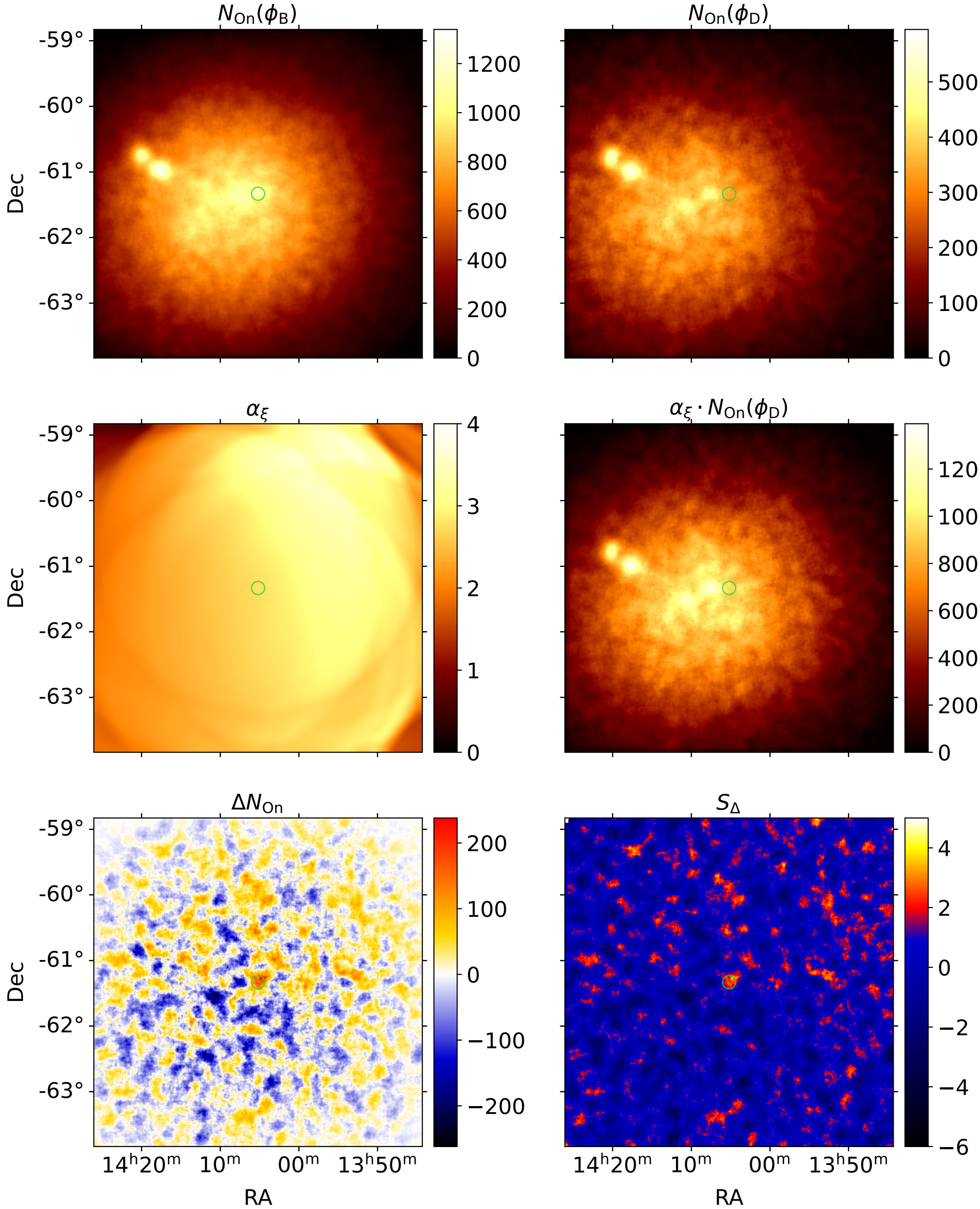

Figure 4.18: Intermediate and final results of the phase map subtraction procedure. From left to right, top to bottom: On-counts of the bright phase $N_{\mathrm{On}}(\phi_{\mathrm{B}})$, and of the dark phase $N_{\mathrm{On}}(\phi_{\mathrm{D}})$, ratio of exposures α_ξ, exposure-weighted on counts of the dark phase $\alpha_\xi \cdot N_{\mathrm{On}}(\phi_{\mathrm{D}})$, subtracted counts ΔN_{On} and subtracted significance S_Δ.

Discussion

5.1 HESS J1832-093

With the currently available set of H.E.S.S. observations, the generated orbital light curve displayed in fig. 4.4 does not show any evident sign of variability. Most data points are, within 1σ error margins, relatively close or compatible with a constant flux. A deviation from the general trend is only seen in phase bin 0.7-0.8, where the flux level is elevated. This phase bin comprises the least observation time, and consequently the corresponding data point has the largest error margin, yet the flux increase is still present within those boundaries. It is coincident with elevated flux levels of the X-ray light curve identified in [15], shown in fig. 2.9, which peaks at phase 0.6-0.7. However, considering the general trend of the TeV light curve, in particular of neighboring data points with more extensive statistics, the elevated flux seems likely to be a product of statistical fluctuations encountered in the limited data of the phase bin. Further, phase bin 0.0-0.1 is not covered by the observations, hence the flux level remains unknown. The compatibility with a constant flux is confirmed by the result of the χ^2-test with $p = 0.31$, far from the level at which the null hypothesis of a constant flux can be discarded.

Similarly, the phase-folded night-wise light curve shown in fig. 4.5 shows no clear trend on the 87.106 d period. Both the Lomb-Scargle period search and the epoch folding method yield no signal power at any significant level within the investigated period ranges.

In conclusion, no sign of orbital variability is found in the data.

5.2 4FGL J1405.1-6119

The orbital light curve obtained from the analyzed data is widely accordant with a constant flux. Between phases 0.0 and 0.7, all data points are close to, or compatible within 1σ levels with the average flux value. A shift to a higher flux is seen in phase bin 0.7-0.8. Afterwards, the flux strongly drops in phases 0.8-1.0, where both data points show similarly reduced levels. This is complemented by the flux level in phase bin 0.0-0.1 which, although compatible within 1σ with the average level, is clearly shifted towards the lower end. The current data does not indicate the presence of orbital variability, as the χ^2-test results in $p = 0.22$. Similarly, the phase-folded night-wise light curve exhibits no clear trend, and no significant periodicity is found with the Lomb-Scargle period search.

The spectral index used for the calculation of flux values is derived from counts that are contaminated by the signal of adjacent sources, hence it cannot be taken as representative of the actual source emission spectrum. This however has no significant effect on the relative flux changes within the orbital light curve, which is verified by performing the calculation with an index of 2.5, a value that is typically observed in galactic point sources.

The methods applied for testing orbital variability and periodicity are insensitive to any prior knowledge of a potential variability pattern. Motivated by the typical behavior of other GRLB systems, it is reasonable to test patterns of variability according to the behavior observed in X-rays. In fact, phases of reduced TeV flux overlap with phases of reduced X-ray flux, as the orbital light curve generated in [16] shown in fig. 2.2 has minimum levels around phases from 0.9-0.0 and 0.0-0.3. While this might be a hint towards an orbital variability in TeV that is potentially detectable, it is desirable to test the relation in a quantitative way. This gives rise to the development and application of the phase map subtraction method.

The latter results in an excess at the source position with a significance of 2.41σ. Although this is below the conventional 5σ detection threshold used for H.E.S.S. analysis, the technique is the most robust and sensitive approach at hand for using the putative correlation of orbital variability between X-ray and TeV to eliminate contamination from the signal and provide a clean detection. Considering that the detection significance scales with the square root of observation time, a 5σ detection would require roughly four times the observation time of the current data set, which comprises $\sim 70\,\mathrm{h}$. Hence, as an estimate, around $\sim 210\,\mathrm{h}$ of observations would have to be added to the data for a 5σ detection. This number however does not account for acceptance-corrections regarding the offsets between the pointing position and source position in the current data set, which would reduce the estimated amount of required hours.

The analysis of the resulting significance distribution at background regions shows that the assumption of equal background levels in both phase blocks is appropriate, since the distribution shown in fig. 4.17 is highly compatible with a standard normal distribution, with fit values deviating only on second decimal places. However, a more nuanced consideration reveals the presence of small systematic effects. For instance, it is evident that the overall distribution of S_Δ at background regions extends further into the negative range than into the positive. Moreover, the deviations of the distribution from the Gaussian fit indicate a pattern that is anti-symmetric around 0, as can be seen from both the fit and its residuals in fig. 4.17. In the positive range, the data is slightly above the fit at significances close to 0, and slightly below at higher significances. In the negative range, it is the opposite way. This observation is again confirmed by the negative skewness of the distribution. Overall, the trend indicates a minor systematic error, where the dark-phase signal is relatively overestimated, resulting in an under-estimation of the detection significance. While the effect on the result is probably minuscule, given the high consistency with the Gaussian fit, it reveals a margin for refinement of the method when used for future analysis of this or other sources with known variability that suffer from signal contamination, where the approach can generally be of potential use.

The usefulness of the method could be verified through simulations, or by applying it to other sources of known periodicity. A suitable candidate would be LS 5039, a GRLB for which the periodicity is known and a substantial amount of H.E.S.S. observational data is available. While this task is beyond the scope of this work, it constitutes an approach for possible future work.

Acknowledgements

This thesis stands at the end of a way that many helped pave for me to walk on.
Prof. Andrea Santangelo could not be stopped by online lecturing from transmitting fascinating knowledge in a passionate, entertaining and interactive way. He gave me the possibility to work in the High Energy Astrophysics Group, and also facilitated my stay in Windhoek, Namibia, a character-shaping lifetime experience of insight and growth.
Dr. Gerd Pühlhofer lead me through the scientific work, provided important and helpful comments to my thesis draft and offered numerous explanations in great detail. He also helped coordinate my shift work at the H.E.S.S. site, an experience that I will never forget.
Dr. Denys Malyshev never failed to find time and patience to help me with countless questions and doubts, sharing his extensive knowledge and offering a support that was crucial for my progress throughout the whole work.
Dr. Michael Backes welcomed me with open arms at the University of Namibia in Windhoek, where most of the work was accomplished. His consistent motivation to share useful knowledge often resulted in valuable input, and his unfailingly happy mood eased my integration into a new environment.
Great scientific advice was given by my IAAT colleagues Fabian Leuschner, Heiko Salzmann, Dr. Baiyang Bi and Charles Thorpe-Morgan, as well as Dr. Emma de Oña Wilhelmi from MPIK.
My time at UNAM was full of joy, laughs and inter-cultural exchange thanks to all my astro-postgrad friends, who made a cold office feel warm and appreciated my efforts as the technical support.
My flat mates have never failed to give me the best possible company ever and even expressed their love by stealing a Christmas tree.
Sharifa was *tha* homie in Nam and propelled the bar for a good conversation into outer space.
My sister carried me through GR, shares my interest in science and gives me huge inspiration by being one of the smartest people that I know. Also, she flew around the world to come visit me.
My parents raised a physics enthusiast with growth and persistence on his mind, never stopped giving me love, facilitated the education that is necessary for a scientific career and supported me and my plans in every possible way with great enthusiasm. Also, my dad proof-read this thesis. Also, they flew around the world to come visit me.
I thank all of you, from the bottom of my heart.

Bibliography

[1] Bradley W. Carroll and Dale A. Ostlie. *An introduction to modern astrophysics*. Pearson Addison Wesley, 2007.

[2] Deepak Raghavan et al. "A SURVEY OF STELLAR FAMILIES: MULTIPLICITY OF SOLAR-TYPE STARS". In: ApJS 190.1 (Aug. 2010), pp. 1–42. DOI: 10.1088/0067-0049/190/1/1. URL: https://doi.org/10.1088%5C%2F0067-0049%2F190%2F1%2F1.

[3] Guillaume Dubus. "Gamma-ray binaries and related systems". In: *The Astronomy and Astrophysics Review* 21.1 (Aug. 2013). DOI: 10.1007/s00159-013-0064-5. URL: https://doi.org/10.1007%5C%2Fs00159-013-0064-5.

[4] Mathieu de Naurois and Daniel Mazin. "Ground-based detectors in very-high-energy gamma-ray astronomy". In: *Comptes Rendus Physique* 16.6 (2015). Gamma-ray astronomy / Astronomie des rayons gamma, pp. 610–627. ISSN: 1631-0705. DOI: https://doi.org/10.1016/j.crhy.2015.08.011. URL: https://www.sciencedirect.com/science/article/pii/S1631070515001462.

[5] *High Energy Stereoscopic System*. URL: https://www.mpi-hd.mpg.de/hfm/HESS/pages/about/ (visited on 05/06/2022).

[6] Maria Chernyakova and Denys Malyshev. *Gamma-ray binaries*. 2020. DOI: 10.48550/ARXIV.2006.03615. URL: https://arxiv.org/abs/2006.03615.

[7] Agnibha De Sarkar et al. "Possible TeV Gamma-Ray Binary Origin of HESS J1828-099". In: ApJ 927.2, L35 (Mar. 2022), p. L35. DOI: 10.3847/2041-8213/ac5aba. arXiv: 2202.13376 [astro-ph.HE].

[8] Guillaume Dubus et al. "Sizing up the population of gamma-ray binaries". In: A&A 608, A59 (Dec. 2017), A59. DOI: 10.1051/0004-6361/201731084. arXiv: 1707.05744 [astro-ph.HE].

[9] Chernyakova, M. et al. "Overview of non-transient binaries and prospects for the Cherenkov Telescope Array". In: A&A 631 (2019), A177. DOI: 10.1051/0004-6361/201936501. URL: https://doi.org/10.1051/0004-6361/201936501.

[10] H. Yoneda et al. "Sign of Hard-X-Ray Pulsation from the γ-Ray Binary System LS 5039". In: Phys. Rev. Lett. 125.11 (Sept. 2020). DOI: 10.1103/physrevlett.125.111103. URL: https://doi.org/10.1103%2Fphysrevlett.125.111103.

[11] C.-Y. Ng et al. "X-Ray and Radio Variabilities of PSR J2032+4127 near Periastron". In: ApJ 880.2 (Aug. 2019), p. 147. DOI: 10.3847/1538-4357/ab2adb. URL: https://doi.org/10.3847%2F1538-4357%2Fab2adb.

[12] Wynn C. G. Ho et al. "Multiwavelength monitoring and X-ray brightening of Be X-ray binary PSR J2032+4127/MT91 213 on its approach to periastron". In: MNRAS 464.1 (Sept. 2016), pp. 1211–1219. ISSN: 0035-8711. DOI: 10.1093/mnras/stw2420. eprint: https://academic.oup.com/mnras/article-pdf/464/1/1211/18518503/stw2420.pdf. URL: https://doi.org/10.1093/mnras/stw2420.

[13] I. F. Mirabel et al. "A double-sided radio jet from the compact Galactic Centre annihilator 1E1740.7–2942". In: Nature 358.6383 (July 1992), pp. 215–217. DOI: 10.1038/358215a0. URL: https://doi.org/10.1038/358215a0.

[14] Guillaume Dubus. "Gamma-ray emission from binaries in context". In: *Comptes Rendus Physique* 16.6 (2015). Gamma-ray astronomy / Astronomie des rayons gamma, pp. 661–673. ISSN: 1631-0705. DOI: https://doi.org/10.1016/j.crhy.2015.08.014. URL: https://www.sciencedirect.com/science/article/pii/S1631070515001498.

[15] Martí-Devesa, G. and Reimer, O. "X-ray and orbital variability from the binary HESS J1832-093". In: A&A 637 (2020), A23. DOI: 10.1051/0004-6361/202037442. URL: https://doi.org/10.1051/0004-6361/202037442.

[16] R. H. D. Corbet et al. "Discovery of the Galactic High-mass Gamma-Ray Binary 4FGL J1405.1-6119". In: ApJ 884.1 (Oct. 2019), p. 93. DOI: 10.3847/1538-4357/ab3e32. URL: https://doi.org/10.3847/1538-4357/ab3e32.

[17] Andrzej A. Zdziarski, Andrii Neronov, and Maria Chernyakova. "A compact pulsar wind nebula model of the γ-ray-loud binary LS I +61°303". In: MNRAS 403.4 (Apr. 2010), pp. 1873–1886. ISSN: 0035-8711. DOI: 10.1111/j.1365-2966.2010.16263.x. eprint: https://academic.oup.com/mnras/article-pdf/403/4/1873/18576531/mnras0403-1873.pdf. URL: https://doi.org/10.1111/j.1365-2966.2010.16263.x.

[18] Josep M. Paredes et al. "Discovery of a High-Energy Gamma-Ray-Emitting Persistent Microquasar". In: *Science* 288.5475 (June 2000), pp. 2340–2342. DOI: 10.1126/science.288.5475.2340. URL: https://doi.org/10.1126/science.288.5475.2340.

[19] Lewis Ball et al. "Origin of the Transient, Unpulsed Radio Emission from the PSR B1259–63 Binary System". In: ApJ 514.1 (Feb. 1999), p. L39. DOI: 10.1086/311928. URL: https://dx.doi.org/10.1086/311928.

[20] M. Massi and M. Kaufman Bernadó. "RADIO SPECTRAL INDEX ANALYSIS AND CLASSES OF EJECTION IN LS I +61°303". In: ApJ 702.2 (Aug. 2009), p. 1179. DOI: 10.1088/0004-637X/702/2/1179. URL: https://dx.doi.org/10.1088/0004-637X/702/2/1179.

[21] S. Abdollahi et al. "*Fermi* Large Area Telescope Fourth Source Catalog". In: ApJS 247.1 (Mar. 2020), p. 33. DOI: 10.3847/1538-4365/ab6bcb. URL: https://doi.org/10.3847%2F1538-4365%2Fab6bcb.

[22] P. M. Saz Parkinson et al. "Classification and Ranking of Fermi LAT Gamma-ray Sources from the 3FGL Catalog using Machine Learning Techniques". In: ApJ 820.1, 8 (Mar. 2016), p. 8. DOI: 10.3847/0004-637X/820/1/8. arXiv: 1602.00385 [astro-ph.HE].

[23] R. Landi et al. “Investigating the X-ray counterparts to unidentified sources in the 1000-orbit INTEGRAL/IBIS catalogue”. In: MNRAS 470.1 (Sept. 2017), pp. 1107–1120. DOI: 10.1093/mnras/stx908. arXiv: 1704.03872 [astro-ph.HE].

[24] J. D. Scargle. “Studies in astronomical time series analysis. II. Statistical aspects of spectral analysis of unevenly spaced data.” In: ApJ 263 (Dec. 1982), pp. 835–853. DOI: 10.1086/160554.

[25] Michael Mayer. “Studies of the Pulsar Wind Nebula Population observed with H.E.S.S.” Diplomarbeit. 2010. URL: https://ecap.nat.fau.de/wp-content/uploads/2017/05/2010_Mayer_Diplom.pdf.

[26] Naomi Tsuji et al. “Cross-match between the Latest Swift-BAT and Fermi-LAT Catalogs”. In: *The Astrophysical Journal* 916.1 (July 2021), p. 28. DOI: 10.3847/1538-4357/ac0341. URL: https://doi.org/10.3847/1538-4357/ac0341.

[27] HESS Collaboration et al. “Discovery of the VHE gamma-ray source HESS J1832-093 in the vicinity of SNR G22.7-0.2”. In: MNRAS 446.2 (Nov. 2014), pp. 1163–1169. ISSN: 0035-8711. DOI: 10.1093/mnras/stu2148. eprint: https://academic.oup.com/mnras/article-pdf/446/2/1163/9379117/stu2148.pdf. URL: https://doi.org/10.1093/mnras/stu2148.

[28] David J. Helfand et al. “MAGPIS: A Multi-Array Galactic Plane Imaging Survey”. In: AJ 131.5 (May 2006), pp. 2525–2537. DOI: 10.1086/503253. URL: https://doi.org/10.1086/503253.

[29] Kaya Mori et al. “*NuSTAR* Hard X-Ray Observation of the Gamma-Ray Binary Candidate HESS J1832-093”. In: ApJ 848.2 (Oct. 2017), p. 80. DOI: 10.3847/1538-4357/aa8d15. URL: https://doi.org/10.3847/1538-4357/aa8d15.

[30] N. R. Lomb. “Least-squares frequency analysis of unequally spaced data”. In: *Astrophysics and Space Science* 39.2 (Feb. 1976), pp. 447–462. DOI: 10.1007/bf00648343. URL: https://doi.org/10.1007/bf00648343.

[31] R. V. Baluev. “Assessing the statistical significance of periodogram peaks”. In: MNRAS 385.3 (Apr. 2008), pp. 1279–1285. DOI: 10.1111/j.1365-2966.2008.12689.x. arXiv: 0711.0330 [astro-ph].

[32] D. A. Leahy. “Searches for pulsed emission - Improved determination of period and amplitude from epoch folding for sinusoidal signals”. In: A&A 180.1-2 (June 1987), pp. 275–277.

[33] Christian Föhr. *H.E.S.S.-II Image Gallery*. URL: https://www.mpi-hd.mpg.de/hfm/HESS/pages/home/Webgalleries/HESS2_telescope/index.html.

[34] Victor F. Hess. “Über Beobachtungen der durchdringenden Strahlung bei sieben Freiballonfahrten”. In: *Phys. Z.* 13 (1912).

[35] P. A. Cherenkov. “Visible luminescence of pure liquids under the influence of γ-radiation”. In: *Dokl. Akad. Nauk SSSR* 2.8 (1934), pp. 451–454. DOI: 10.3367/UFNr.0093.196710n.0385.

[36] I. M. Frank and I. E. Tamm. “Coherent visible radiation of fast electrons passing through matter”. In: *Compt. Rend. Acad. Sci. URSS* 14.3 (1937), pp. 109–114. DOI: 10.3367/UFNr.0093.196710o.0388.

[37] PMS Blackett. "Gassiot Committee Report". In: Phys. Soc. Lond. 1948.

[38] W. GALBRAITH and J. V. JELLEY. "Light Pulses from the Night Sky associated with Cosmic Rays". In: Nature 171.4347 (Feb. 1953), pp. 349–350. DOI: 10.1038/171349a0. URL: https://doi.org/10.1038/171349a0.

[39] T. C. Weekes et al. "Observation of TeV Gamma Rays from the Crab Nebula Using the Atmospheric Cerenkov Imaging Technique". In: ApJ 342 (July 1989), p. 379. DOI: 10.1086/167599.

[40] S. P. Swordy. "The Energy Spectra and Anisotropies of Cosmic Rays". In: Space Sci. Rev. 99 (Oct. 2001), pp. 85–94. DOI: 10.1023/A:1013828611730.

[41] Alicia López Oramas. "Multi-year Campaign of the Gamma-Ray Binary LS I +61◦ 303 and Search for VHE Emission from Gamma-Ray Binary Candidates with the MAGIC Telescopes". PhD thesis. Universitat Autònoma de Barcelona, 2014.

[42] Malcolm S. Longair. *High Energy Astrophysics*. 3rd ed. Cambridge University Press, 2011. DOI: 10.1017/CBO9780511778346.

[43] K. Bernlöhr. *Pictures and movies from simulated air showers*. URL: https://www.mpi-hd.mpg.de/hfm/~bernlohr/HESS/MC_images/.

[44] F. Aharonian et al. "Observations of the Crab nebula with HESS". In: A&A 457.3 (Oct. 2006), pp. 899–915. DOI: 10.1051/0004-6361:20065351. arXiv: astro-ph/0607333 [astro-ph].

[45] Iryna Lypova et al. "A Major Upgrade of the H.E.S.S. Cherenkov Cameras". In: *EPJ Web of Conferences* 136 (2017). Ed. by A. Morselli, A. Capone, and G. Rodriguez Fernandez, p. 03002. DOI: 10.1051/epjconf/201713603002. URL: https://doi.org/10.1051/epjconf/201713603002.

[46] John M. Davies and Eugene S. Cotton. "Design of the quartermaster solar furnace". In: *Solar Energy* 1.2 (1957), pp. 16–22. ISSN: 0038-092X. DOI: https://doi.org/10.1016/0038-092X(57)90116-0. URL: https://www.sciencedirect.com/science/article/pii/0038092X57901160.

[47] K. Bernlöhr et al. "The optical system of the H.E.S.S. imaging atmospheric Cherenkov telescopes. Part I: layout and components of the system". In: *Astroparticle Physics* 20.2 (Nov. 2003), pp. 111–128. DOI: 10.1016/S0927-6505(03)00171-3. arXiv: astro-ph/0308246 [astro-ph].

[48] R. Cornils et al. "The optical system of the H.E.S.S. imaging atmospheric Cherenkov telescopes. Part II: mirror alignment and point spread function". In: *Astroparticle Physics* 20.2 (Nov. 2003), pp. 129–143. DOI: 10.1016/S0927-6505(03)00172-5. arXiv: astro-ph/0308247 [astro-ph].

[49] S. Funk et al. "The trigger system of the H.E.S.S. telescope array". In: *Astroparticle Physics* 22.3-4 (Nov. 2004), pp. 285–296. DOI: 10.1016/j.astropartphys.2004.08.001. arXiv: astro-ph/0408375 [astro-ph].

[50] Mathieu de Naurois. "The Making of Catalogues of Very-High-Energy γ-ray Sources". In: *Universe* 7.11 (Nov. 2021), p. 421. DOI: 10.3390/universe7110421. URL: https://doi.org/10.3390/universe7110421.

[51] J. Hahn et al. "Heidelberg Data Quality Selection (H.E.S.S. internal note)". 2013.

[52] J. Hahn et al. “Impact of aerosols and adverse atmospheric conditions on the data quality for spectral analysis of the H.E.S.S. telescopes”. In: *Astroparticle Physics* 54 (Feb. 2014), pp. 25–32. DOI: 10.1016/j.astropartphys.2013.10.003. arXiv: 1310.1639 [astro-ph.IM].

[53] A. M. Hillas. “Cerenkov Light Images of EAS Produced by Primary Gamma Rays and by Nuclei”. In: *19th International Cosmic Ray Conference (ICRC19), Volume 3*. Vol. 3. International Cosmic Ray Conference. Aug. 1985, p. 445.

[54] Mathieu de Naurois. “Very High Energy astronomy from H.E.S.S. to CTA. Opening of a new astronomical window on the non-thermal Universe”. Habilitation à diriger des recherches. Université Pierre et Marie Curie - Paris VI, Mar. 2012. URL: https://tel.archives-ouvertes.fr/tel-00687872.

[55] Stefan Funk. “A new population of very high-energy gamma-ray sources detected with H.E.S.S. in the inner part of the Milky Way”. Dissertation. 2005. DOI: 10.11588/HEIDOK.00005542. URL: http://archiv.ub.uni-heidelberg.de/volltextserver/id/eprint/5542.

[56] S. Ohm, C. van Eldik, and K. Egberts. “γ/hadron separation in very-high-energy γ-ray astronomy using a multivariate analysis method”. In: *Astroparticle Physics* 31.5 (June 2009), pp. 383–391. DOI: 10.1016/j.astropartphys.2009.04.001. URL: https://doi.org/10.1016/j.astropartphys.2009.04.001.

[57] R. D. Parsons and J. A. Hinton. “A Monte Carlo template based analysis for air-Cherenkov arrays”. In: *Astroparticle Physics* 56 (Apr. 2014), pp. 26–34. DOI: 10.1016/j.astropartphys.2014.03.002. arXiv: 1403.2993 [astro-ph.IM].

[58] T. -P. Li and Y. -Q. Ma. “Analysis methods for results in gamma-ray astronomy.” In: ApJ 272 (Sept. 1983), pp. 317–324. DOI: 10.1086/161295.

[59] S. S. Wilks. “The Large-Sample Distribution of the Likelihood Ratio for Testing Composite Hypotheses”. In: *The Annals of Mathematical Statistics* 9.1 (Mar. 1938), pp. 60–62. DOI: 10.1214/aoms/1177732360. URL: https://doi.org/10.1214/aoms/1177732360.

[60] S. Gillessen and H. L. Harney. “Significance in gamma-ray astronomy - the Li & Ma problem in Bayesian statistics”. In: A&A 430 (Jan. 2005), pp. 355–362. DOI: 10.1051/0004-6361:20035839. arXiv: astro-ph/0411660 [astro-ph].

[61] Wolfgang A. Rolke, Angel M. López, and Jan Conrad. “Limits and confidence intervals in the presence of nuisance parameters”. In: *Nuclear Instruments and Methods in Physics Research A* 551.2-3 (Oct. 2005), pp. 493–503. DOI: 10.1016/j.nima.2005.05.068. arXiv: physics/0403059 [physics.data-an].

[62] *Astropy Documentation on Lomb-Scargle Periodograms*. URL: https://docs.scipy.org/doc/scipy/reference/generated/scipy.stats.chi2.html (visited on 09/01/2023).

[63] Jacob T. VanderPlas. “Understanding the Lomb–Scargle Periodogram”. In: *The Astrophysical Journal Supplement Series* 236.1 (May 2018), p. 16. DOI: 10.3847/1538-4365/aab766. URL: https://doi.org/10.3847/1538-4365/aab766.

[64] *Astropy Documentation on Lomb-Scargle Periodograms*. URL: https://docs.astropy.org/en/stable/timeseries/lombscargle.html (visited on 06/12/2022).